symmetry

MDPI

Review

Characterisation and Manipulation of Polarisation Response in Plasmonic and Magneto-Plasmonic Nanostructures and Metamaterials

Pritam Khan, Grace Brennan, James Lillis, Syed A. M. Tofail, Ning Liu and Christophe Silien *

Department of Physics and Bernal Institute, University of Limerick, V94 T9PX Limerick, Ireland; Pritam.Khan@ul.ie (P.K.); grace.brennan@ul.ie (G.B.); james.lillis@ul.ie (J.L.); tofail.syed@ul.ie (S.A.M.T.); ning.liu@ul.ie (N.L.)

* Correspondence: christophe.silien@ul.ie

Received: 9 July 2020; Accepted: 12 August 2020; Published: 17 August 2020

Abstract: Optical properties of metal nanostructures, governed by the so-called localised surface plasmon resonance (LSPR) effects, have invoked intensive investigations in recent times owing to their fundamental nature and potential applications. LSPR scattering from metal nanostructures is expected to show the symmetry of the oscillation mode and the particle shape. Therefore, information on the polarisation properties of the LSPR scattering is crucial for identifying different oscillation modes within one particle and to distinguish differently shaped particles within one sample. On the contrary, the polarisation state of light itself can be arbitrarily manipulated by the inverse designed sample, known as metamaterials. Apart from polarisation state, external stimulus, e.g., magnetic field also controls the LSPR scattering from plasmonic nanostructures, giving rise to a new field of magneto-plasmonics. In this review, we pay special attention to polarisation and its effect in three contrasting aspects. First, tailoring between LSPR scattering and symmetry of plasmonic nanostructures, secondly, manipulating polarisation state through metamaterials and lastly, polarisation modulation in magneto-plasmonics. Finally, we will review recent progress in applications of plasmonic and magneto-plasmonic nanostructures and metamaterials in various fields.

Keywords: plasmonics; LSPR scattering; polarisation manipulation; metamaterials; Faraday effect (rotation); magneto-optic Kerr effect (MOKE); magnetoplasmonics

1. Introduction

Of late, thanks to their unique chemical, electrical and optical properties, nanomaterials have been the subject of extensive research in the frame of nanoscience and nanotechnology from the point of view of both fundamental science and practical applications. Among the family of nanomaterials, metallic nanostructures are of particular interest because of their remarkable optical properties that leads to a plethora of novel phenomena, mediated by elementary excitations, known as plasmons [1,2]. Localised surface plasmon resonance (LSPR) takes place from the collective oscillations of conduction electrons near metallic nanoparticles following light excitation [3]. LSPR in metallic nanoparticles allows to manipulate light at the nanoscale that gives rise to exotic phenomena, e.g., optical near-field enhancement at resonant wavelength, hot-electron generation [4,5], etc. Likewise, such effects find tremendous potential applications in photocarrier generators [6], optical holography [7], plasmonic routers [8], biosensors [9,10], surface-enhanced Raman scattering (SERS) [11], etc. LSPR of the plasmonic nanostructures can be readily tuned by the geometry, i.e., shape and size of the plasmonic nanostructures which in turn can be correlated with the polarisation state of the incident light [1,12].

It is well known that polarisation is a key attribute of light that describes the oscillation direction of the electromagnetic wave, that plays an important role in the light–matter interactions [13,14]. In particular, the resonant light scattering from plasmonic nanostructures (Figure 1) is expected to show the symmetry of the plasmon mode and the particle shape [15]. Therefore, detailed knowledge of the scattered light polarisation from plasmonic nanostructures is very important to understand the fundamental physics and practical applications of such nanostructures. At the same time, it also helps to differentiate several oscillation modes within one particle as well as distinguish particles of different shape within one nanostructure. For example, smallest unit of nanostructures like silver/gold nanosphere (diameter less than 50 nm) or nanoparticle dimer has high symmetry with only one dipole plasmon [16,17].

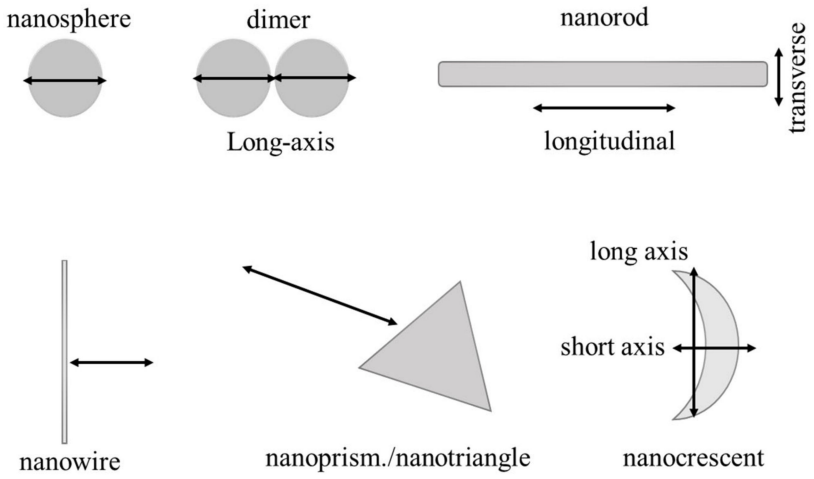

Figure 1. Plasmonic nanostructures of various shape. The arrow indicates the axis of symmetry of the nanostructures for the excitation of LSPR.

Moving on to nanoparticle trimer with broken symmetry in their geometry, they exhibit a polarisation response that is altogether different from the dipolar response of a dimer [17,18]. Similarly, in nanorods, instead of one dipole, two dipolar peaks, transverse and longitudinal [19] appear. Further complicated nanostructures like triangular Ag nanoparticles [20,21] or nanocrescents [22] possess in- and out-of-plane dipole, quadrupole and even higher multipoles. Several techniques, including dark-field (DF) extinction [17,23], SERS scattering [24,25], infrared absorption [22,26] have been used to extract the optical response of plasmonic nanostructures to get information on the polarisation state. In the first part of the review, we aim to tailor between LSPR scattering and symmetry of plasmonic nanostructures by going through polarisation sensitive optical measurements in such nanostructures. On the contrary, in another end of the spectrum, artificial plasmonic nanostructures are inversed designed to control the polarisation state of the light wave [27,28]. This new set of artificial materials are classified as metamaterials, that are composed of periodically arranged subwavelength dielectric elements or structured metallic components [29,30]. The metamaterials can arbitrarily manipulate the polarisation state of the electromagnetic waves with multiple degrees of freedom, that has found tremendous potential application in nanophotonics [31,32]. We will discuss the designing of such metamaterial strictures and their excellent application prospective in the second part of the review. In the last section, we will discuss magneto-optics and magnetoplasmonics with particular emphasis on the role of polarisation in a number of experiments including the Faraday effect, inverse Faraday effect, magneto-optical Kerr effect, magnetic second-harmonic generation and magnetic circular dichroism. Finally, we will explore a number of relevant applications.

2. Tailoring between LSPR Scattering and Symmetry of Plasmonic Nanostructures

In this section, we will discuss the polarisation dependent LSPR response of various plasmonic nanostructures of different shape and size. It is well known that axis of symmetry of plasmonic nanostructures plays an important role and by exciting along the favourable symmetry axis LSPR response can be enhanced significantly. Below we will analyse several plasmonic nanostructures and their LSPR response by polarisation sensitive measurements.

2.1. Single Nanosphere and Dimer

The smallest unit of plasmonic nanostructure is a single nanoparticle or nanosphere. The scattering spectra of a single Ag/Au nanosphere has one major peak, originated from the interaction of electromagnetic waves with the free electrons of the nanospheres. For single nanoparticles, the LSPR does not exhibit any marked polarisation dependence [33]. It can be seen from Figure 2a that LSPR of two isolated Au nanoparticles occurs at 573 nm and it is indistinguishable for two orthogonal light polarisations. However, if these two nanoparticles are brought closer, they get dimerised because of plasmonic coupling and a strong polarisation anisotropy takes place. For polarisation perpendicular to the long axis of the dimer, LSPR peak at 573 nm overlaps with that of a single particle [34], however, for polarisation parallel to the long axis of the dimer, we observed a strongly red-shifted spectrum with LSPR at 588 nm which is ascribed to the "long axis" mode of dimer. The position of the LSPR of a dimer corresponding to both parallel and perpendicular polarisation depends strongly on the interparticle distance (d) as well as their relative interaction [34]. In Figure 2b when d changes from 10 (1) to 25 nm (3), LSPR position of Ag dimer for parallel polarisation redshifts approximately by 100 nm. In contrast, for perpendicular polarisation LSPR exhibits very weak blueshift. It is important to note that, for very large d ~ 250 nm, LSPR of the dimer (5) is comparable to that of an individual particle (6). This observation indicates that when the separation is large between the pair of particles, it becomes complicated to resolve the effects of particle interactions.

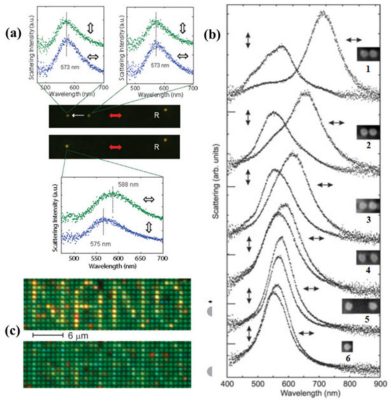

Figure 2. (**a**) Alignment of a dimer composed of two ~80 nm gold nanoparticles. The upper graphs are spectra for the immobilised particle (left) and the optically trapped particle (right) before dimerisation. The lower spectra correspond to the case when the two particles have been brought into near-field coupling range. All the figures were reprinted (adapted) with permission from [33], Copyright 2010, American Chemical Society. (**b**) DF spectra and SEM micrographs from isolated particle pairs with varying separations in parallel and perpendicular polarisation, as indicated by arrows. The separations (gaps) between the particles are d ~ (1) 10, (2) 15, (3) 25, (4) 50, and (5) 250 nm. Spectrum 6 from a single particle is included for comparison. The vertical bars indicate the baselines for the different spectra. (**c**) DF images form an array of "identical" silver disks with a diameter of 80 nm and a height of 25 nm. The text "NANO" is written with pairs of such particles with an interparticle distance of approximately 110 nm. In the top image, the array is illuminated with light polarised parallel to the particle pair axis. In the bottom image, the polarisation is perpendicular to the pair axis. All the figures were reprinted (adapted) with permission from [34], Copyright 2005, American Chemical Society.

The effect of parallel and perpendicular polarisations on the dimer composed of Ag particles array can be readily seen from the DF images shown in Figure 2c. For the top panel, under parallel polarisation, the text "NANO" written with dimers appears red compared to green single particles. In contrast, for perpendicular polarisation the text appears blue in the green single particle background. Such observation is in line with the results shown in Figure 2b.

Next, we discuss the detailed polarisation response of single Ag nanosphere dimer (Figure 3a). The dimer is oriented at 40° with respect to the normal. In this regard, Figure 3b,c demonstrates the polar plot of Raman scattering intensity profile and depolarisation ratio (ρ) of the dimer, respectively against the polarisation angle at two dominant Raman bands of the dimer. Both the Raman scattering intensity and depolarisation ratio varies between ±1, at parallel and perpendicular to the dimer axis, respectively [18]. Therefore, clearly indicating that scattering from the dimer is linearly polarised in line with the results from Tian et al. [17]. Figure 3c also reveals that the depolarisation ratio of a dimer is wavelength independent.

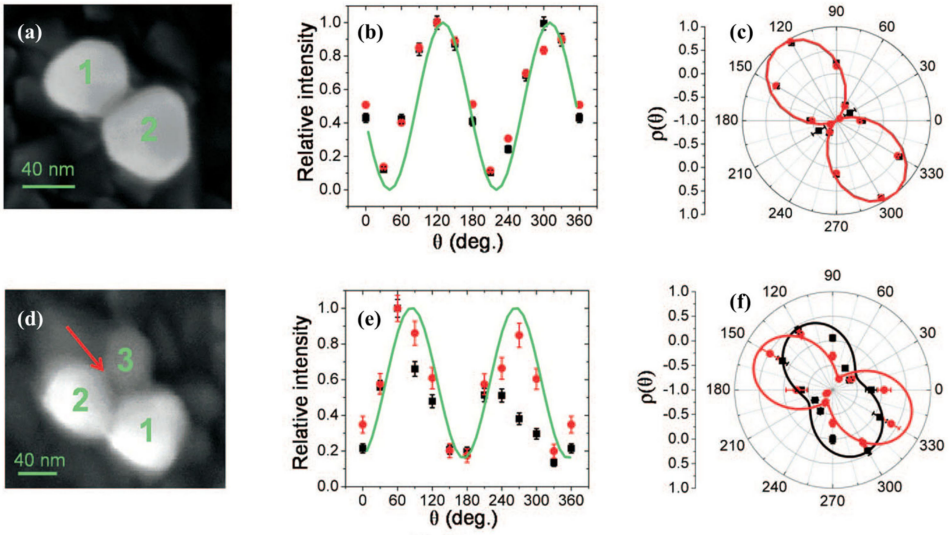

Figure 3. Polarisation response of a nanoparticle dimer and trimer. SEM image of the (**a**) dimer and (**d**) trimer of nanoparticles. The red arrow in (**d**) indicates the position of the molecule that leads to the best agreement between experiment and calculation. Normalised RS intensity at 555 (black squares) and 583 nm (red circles) as a function of the angle of rotation of the incident polarisation for (**b**) dimer and (**e**) trimer. Depolarisation ratio (ρ) measured at 555 (black squares) and 583 nm (red circles) for (**c**) dimer and (**f**) trimer. All the figures were reprinted (adapted) with permission from [18], Copyright 2008, National Academy of Sciences, USA.

2.2. Nanosphere Trimer

When an additional third particle (1) is added at the junction of a dimer formed by particles 2 and 3, it breaks the axial symmetry (Figure 3d) to form a trimer and the polarisation response of a symmetry-broken trimer is altogether different from that of a dimer. Figure 3e represents the Raman scattering profile of the trimer at the same wavelengths of that of the dimer, with varying incident polarisation angle. The maximum signal is obtained at 75° which does not match with the alignment of any of the pairs. The polar plot of the depolarisation ratio for a trimer shown in Figure 3f exhibits strong wavelength dependence, i.e., for different wavelengths it is rotated at different angles from the Raman intensity profile [18]. Unlike dimer, the scattered intensity in trimer never reaches ±1, signifying elliptically polarised light scattering from a trimer, which could arise from the presence of broken symmetry, after a third particle is added to a symmetric dimer to form a trimer. Apart from the results above, there are several other studies which also represent similar polarisation dependent optical response of plasmonic dimer [17,23,35] and trimer nanostructures [36,37].

2.3. Nanorod

Nanorods are the perfect example of "antenna-like" plasmonic structures, therefore the polarisation pattern of the scattered light holds paramount importance for practical applications [15]. Especially, gold nanorods have shown extremely strong light scattering due to the combination of lightning rod effect [38] and the suppression of interband damping [39]. In this regard, Figure 4a reveals the comparison between the single-particle scattering spectra of a nanosphere and a nanorod which shows that LSPR of the sphere at 2.19 eV and for the long-axis mode of the rod at 1.82 eV [39]. By extracting the linewidth (Γ) of the LSPR of nanosphere and nanorod, it is evident that Γ for nanorod is significantly lower than that of nanosphere which leads to lower plasmon damping for nanorods owing to their small volume.

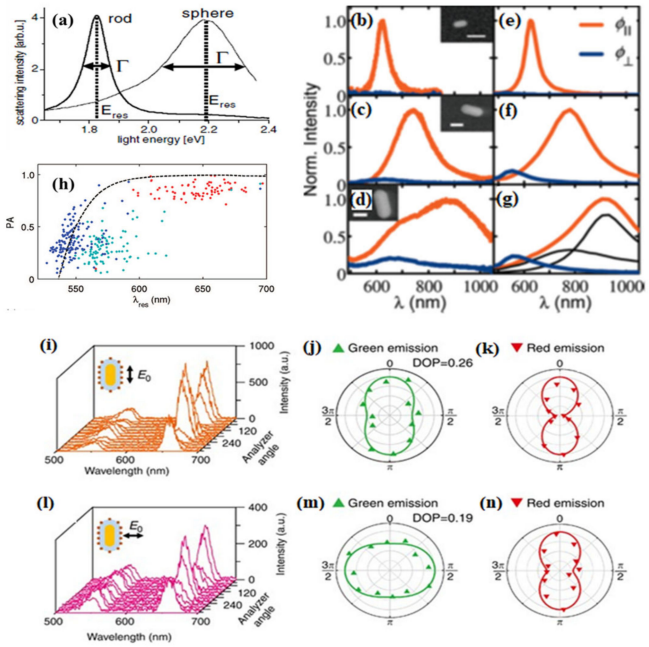

Figure 4. (**a**) Light-scattering spectra from a gold nanorod and gold nanosphere measured under identical conditions (light polarised along the long rod axis). All the figures were reprinted (adapted) with permission from [39], Copyright 2002, American Physical Society. Scattering spectra of single AuNRs with (**b**) d = 32 nm, (**c**) d = 81 nm, and (**d**) d = 100 nm, all having AR of ~2.2 ± 0.1, and the corresponding DDA calculations (**e**–**g**), respectively. All the figures were reprinted (adapted) with permission from [40], Copyright 2010, American Chemical Society. The spectra were recorded for scattered light polarised parallel (red) and perpendicular (blue) to the orientation of the main rod axis. A fit to a sum of two Lorentzian curves is included as black lines in (**g**). In all images, the scale bar represents 100 nm. (**h**) The polarisation at the longitudinal plasmon resonance wavelength λ_{res} is shown as a function of the resonance wavelength for three different gold particle samples (blue dots, nominally spherical gold particles with 60 nm diameter; 87 nm diameter, teal dots; and red dots, gold nanorods). The dashed black line is a theoretical prediction from simulations of gold rods of different aspect ratios and sizes embedded in water. All the figures were reprinted (adapted) with permission from [15], Copyright 2008, American Chemical Society. (**i**) UC emission spectra obtained as the analyser angle varied from 0 to 2 π under excitation polarisation parallel to the long axis of the hybrid nanostructure. From these spectra, the polar plots were extracted for the green (**j**) and red (**k**) emissions. (**l**) UC emission spectra under perpendicular excitation and corresponding polar plots for green (**m**) and red (**n**) emissions. The lines in the polar plots are cosine-squared fits of the experimental data. All the figures were reprinted (adapted) with permission from [41], Copyright 2017, Springer Nature.

It is well known that nanorods exhibit two LSPR modes, one that exhibits a strong polarisation response along the long axis (length), known as longitudinal LSPR and the other one with very weak polarisation response along the short axis (width) of nanorods, referred as transverse LSPR [40].

Longitudinal LSPR is of particular interest because it is tunable across the whole visible and near-infrared region by precisely tailoring the length (l), width (d), and/or aspect ratio (AR) of the nanorod as demonstrated in [40]. Figure 4 depicts the scattering spectra of AuNR for different d and l with fixed AR of 2.2 (±0.1). For the AuNR with (d, l) = 32 × 69 nm, a narrow longitudinal dipole LSPR is observed at 620 nm with no transverse component. When the size of AuNR increases to (d, l) = 84 × 174 nm and (d, l) = 100 × 227 nm, a clear redshift is observed in longitudinal LSPR to 740 and 900 nm, respectively as shown Figure 4c,d. Apart from that, a weak transverse LSPR peak appears in Figure 4c,d at 600 and 660 nm, respectively, because of the larger width of the AuNR [42,43]. Till now, the AuNRs discussed have a low AR of 2.2. Increasing the AR of a slim AuNR to 3.1 (24 × 74 nm) can lead to the similar redshift of the longitudinal LSPR. Experimental scattering spectra of these AuNR shows good agreement with the DDA calculations as depicted in Figure 4e–g. The longitudinal LSPR is highly anisotropic, i.e., it only favourably gets excited for polarisation along the long axis of the rod, and remains unexcited otherwise. Likewise, the scattered light from AuNR exhibits a dipolar response, in line with a cosine-squared function [44].

The strong polarisation dependent optical response in plasmonic nanosphere and nanorods in turn can be exploited to reveal the nanoparticle symmetry. In this context, wavelength-dependent polarisation anisotropy (PA(λ)) serves as an efficient parameter to distinguish nanoparticles with different symmetry [15]. In general, $PA(\lambda) = (I_{major} - I_{minor})/(I_{major} + I_{minor})$, where I_{major} and I_{minor} are defined as the scattering intensity of light polarised parallel to the major and minor axes, respectively [45]. For this purpose, PA is extracted at the resonance wavelength λ_{res}. Figure 4h shows that for an AuNR of (d, l) = 28 × 57 nm shows a high degree of $PA(\lambda_{res}) \sim 0.84$ [39], whereas for spherical AuNP of diameters 60 and 87 nm had an average $PA(\lambda_{res}) \sim 0.35$. It is important to note that AuNP and AuNR exhibit contrasting PA(λ) spectra. For AuNR, it is strongly wavelength dependent, i.e., the long-axis plasmon mode is only excited at the resonance wavelength, whereas for AuNP, PA(λ) is independent of excitation wavelength. It is also found that LSPR linewidth scales inversely with $PA(\lambda_{res})$, i.e., linewidth is lower for particles with high $PA(\lambda_{res})$. Likewise, we can conclude from Figure 4a AuNR with lower linewidth has high $PA(\lambda_{res})$ compared to AuNP at resonance wavelength [15].

AuNRs are an important plasmonic nanostructure which can strongly enhance as well as influence the polarisation state of fluorescence from organic fluorophores or upconversion nanocrystals (UCNC) [41]. It has been shown that, similar to bare AuNR, in hybrid nanostructures of AuNR-fluorophore (oxazine 725), the fluorescent emission is also polarised along the long axis of the NR and exhibits a dipolar pattern. However, the polarisation response of the emission pattern is bit compilated for hybrid plasmonic UCNCs. By measuring the emission spectra of UCNC hybrid nanostructures at polarisation angles from 0° to 360°, by keeping the excitation laser either parallel (Figure 4i) or perpendicular (Figure 4l) to the long axis of the hybrid nanostructure, two dominant emission bands are observed cantered at 540 (green) and 660 nm (red). In this regard, Figure 4j,k,m,n shows the polar plot of red and green emission, respectively. Clearly, red emission is independent of the excitation polarisation, i.e., for both parallel and perpendicular polarisation, red emission follows the scattering pattern of AuNR. In stark contrast, green emission follows the excitation polarisation and oriented along and perpendicular to the long axis of AuNR for parallel and perpendicular excitation polarisation, respectively. The observed results are explained on the basis of Förster resonance energy transfer (FRET) between the emission dipole of the UCNC and the plasmonic dipole of the AuNR [41].

Similar polarisation sensitive measurements on the LSPR of plasmonic Au nanorods and their arrays can be found in the following articles [46–49].

2.4. Nanowire

One-dimensional nanowires (NW) with length of tens of microns stand apart thanks to their easy microscopic directionality [50,51] compared to other counterparts like dimer or NR, where because of diffraction limit it is difficult to estimate the direction of the dimer axis or the long axis of the nanorod. The LSPR response of a NW can be easily tuned by varying the polarisation angle between incident polarisation and NW axis orientation. The excitation of LSPR in NW leads to well-known phenomenon of surface-enhanced Raman scattering (SERS) [25,52,53] that has been explored extensively for chemical and biological sensing. Mohanty et al. [54] demonstrated experimentally as well as from finite difference time domain (FDTD) simulation that SERS signal in the AgNW system reached maximum when the incident laser is perpendicular to NW axis. Similar results are also obtained by Li et al. [55] which shows that when the SERS spectra of R6G is measured at one spot on a NW at different polarisation angles it exhibits maximum at $\theta = 90$, i.e., for vertical polarisation as shown in the polar plot of Figure 5a. The results remain consistent when measured at different spots of the sample. They also demonstrated the dimerisation of 4-nitrobenzenethiol (4NBT) to p,p'-dimercaptoazobenzene (DMAB), arising from LSPR and monitored via SERS. It is shown in Figure 5b that when the polarisation angle θ changes from 0 to 90, new peaks, e.g., ν_4, ν_5, ν_6 gradually increase, indicating the catalytical transformation of 4NBT to DMAB. The above results are further substantiated with DF measurements (Figure 5c) which shows that LSPR scattering increases with increase in polarisation angle and becomes maximum for vertical polarisation, i.e., $\theta = 90$. In another study, Wei and co-workers [25] have shown that SERS of AgNW can be further enhanced by the presence of another metallic nanoparticle (AuNP) adjacent to the wire. The magnitude of this coupling is shown to be independent of the NP shape following the theoretical prediction. However, a strong polarisation dependence is expected owing to strong local and polarisation sensitive electric field enhancements at the NP-NW junctions [56] as shown by the SERS spectra in Figure 5d for different probe positions (Figure 5e) using Malachite green isothiocyanate (MGITC). SERS is inherently a plasmonic property, and therefore remains absent from Si substrate without Ag nanostructures, although the probe molecule MGITC is strongly resonant at 633 nm excitation. When SERS is probed on the trunk of the AgNW, a weak SERS signal is observed. Surprisingly, a remarkable enhancement is observed in the SERS signal when an AuNP is placed near the NW, thanks to the coupling between the AuNP-AgNW plasmons. A polarisation dependent study of the SERS signal in AuNP-AgNW system reveals that when the laser is polarised perpendicularly to the NW, the SERS intensity increases and remains weak for parallel polarisation [56]. The polarisation pattern of the composite system shown in Figure 5f exhibits a dipolar pattern similar to the observation by Mohanty [54] and Li [55].

Apart from SERS, one-photon photoluminescence (PL) is also found to be enhanced significantly by the plasmon coupling between Ag nanowire on top of an Au film in the presence of a ~6 nm dielectric spacer (gap plasmon mode) that supports a localised resonance. In their work, Hu and colleagues [57] further demonstrated that the PL associated with the gap plasmon mode depends strongly on the polarisation angle between the incident laser polarisation and the nanowire orientation, thus exhibits a dipolar emission profile. In this regard, Figure 5g depicts the DF scattering spectra peaking at 655 nm, which is attributed to the gap plasmon mode. Clearly, for perpendicular polarisation (red curve) the peak is much stronger than parallel polarisation (black curve). Such observation confirms that gap plasmon mode is associated with the transverse charge oscillations across nanowire-film junction. PL spectra in Figure 5h follow similar trend like DF scattering, i.e., maximum for perpendicular polarisation ($\theta = 90°$), which almost disappears under parallel polarisation ($\theta = 0°$). Like excitation polarisation, analyser or detection polarisation also plays a significant role in PL or SERS signal. It is found that when the analyser polarisation (Figure 5i) is parallel with excitation polarisation, the detected signal becomes strongest and diminishes when they are perpendicular to each other. In short, LSPR in nanowires can be favourably excited when the incident laser is directed perpendicular to the nanowire axis thanks to the spatial confinement of the electrons at the nanowire and the neighbouring medium interface. Such polarisation dependence is in strong contrary to the case of spherical nanoparticle,

where plasmon excitation is polarisation independent due to spherical geometry [58]. Apart from the above-mentioned results, there are many other studies [59–62] which also discuss the polarisation response LSPR response of plasmonic NWs.

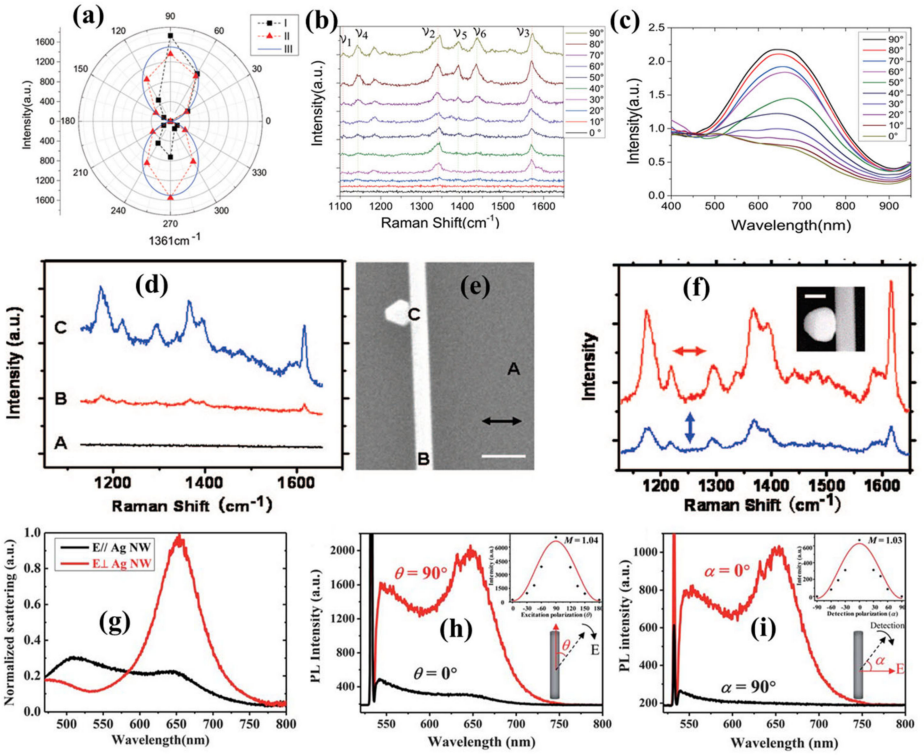

Figure 5. (**a**) Polar plot of SERS intensity at different polarisation angles (I), at different spots (II) and (III) $Sin^2\theta$ function for comparison. (**b**) SERS spectrum of 4NBT on the NW at different polarisation angles θ. (**c**) Experimentally measured DF scattering spectra with single NWs at different polarisation angles. All the figures were reprinted (adapted) with permission from [54], Copyright 2018, Royal Society of Chemistry. (**d**) Raman spectra of MGITC from different positions of the sample as shown in (**e**). The scale bar is 400 nm. The arrow in the SEM image shows the incident polarisation. (**f**) SERS spectra of MGITC at two different polarisations for the wire-particle shown in the inset. The scale bar in the inset is 200 nm. All the figures were reprinted (adapted) with permission from [25], Copyright 2008, American Chemical Society. (**g**) The scattering spectra were obtained under horizontal (red) and perpendicular (black) conditions. The strong and sharp resonant peak at 653 nm is due to the gap plasmon resonance, which is barely present under parallel illumination. (**h**) and (**i**) represent the excitation and detection polarisation dependences of PL intensity under 532 nm lasers, respectively. The absolute peak intensities as a function of excitation and collection polarisation are shown in the insets in (**h**) and (**i**), respectively, exhibiting a good dipole behaviour in photon absorption and emission All the figures were reprinted (adapted) with permission from [57], Copyright 2013, Royal Society of Chemistry.

2.5. Nanohole and Nanoellipse

Among the family of plasmonic nanostructures of different symmetry, elliptical geometry has particular importance because of its inherent anisotropy [63,64]. Therefore, the LSPR of elliptical plasmonic nanostructures is expected to be highly polarisation dependent. In this regard, Figure 6a shows the reflectance spectra of Au ellipsoidal cylinders with axes 80 and 110 nm, inside an array with a lattice constant of 200 nm under unpolarised and linearly polarised light parallel to two different axes [65]. The inset depicts the SEM image of the nanoparticle array. The broad LSPR observed for unpolarised excitation can be easily resolved by polarised illumination parallel to two axes, found to be located near 630 and 730 nm. Experimental observations are further verified with DDA simulations

in the sample with the same dimension, however, with a larger lattice constant of 300 nm. The DDA simulations confirm the presence of two distinct resonance peaks even with unpolarised excitation when there is no coupling between neighbouring particles due to a larger lattice constant. Nevertheless, selective polarisation parallel to axes can lead to the excitation of the individual LSPR as evident from Figure 6b. Of late, Xia and co-workers [66] exploited the inherent asymmetry of elliptical graphene disks (Figure 6c) and showed that two orthogonal plasmonic modes along minor and major axes can be excited together or separately by choosing the incident light polarisation. The polarisation response is shown in Figure 6d,e for minor and major axis excitation, respectively, that reveals that resonant high frequency modes are favourably excited for minor axis polarisation. Apart from that, with an increase in AR, LSPR frequency for the eigenmode along the minor axis shows a blueshift, while it remains almost unchanged for the eigenmode along the major axis. Such observation indicates that the LSPR frequency of the mode along the minor axis is more sensitive to its length. To understand the role of incident light polarisation, first, the results are shown for a round graphene disk in Figure 6f,i. Expectedly, polarisation independent isotropic response is observed due to spherical symmetry of the round disk. On the other hand, Figure 6g,h shows polarisation dependent scattering spectra of two different sized ellipses by varying the polarisation direction from the minor axis (0°) to the major axis (90°). The relative strength of minor and major axes modes is shown by the polar plots for two ellipses in Figure 6j,k. They found that for both the ellipses, scattered intensity along the major axis (blue curve) is larger than that along the minor axis (red curve), thereby suggesting that light–matter interaction takes place predominantly along the major axis. Notably, the frequency difference between major and minor axes plasmon modes increases with increase in size difference between them, therefore provides more degrees of freedom for light manipulation. A similar kind of polarisation dependent response in plasmonic elliptical nanoholes can also be found elsewhere [67–69].

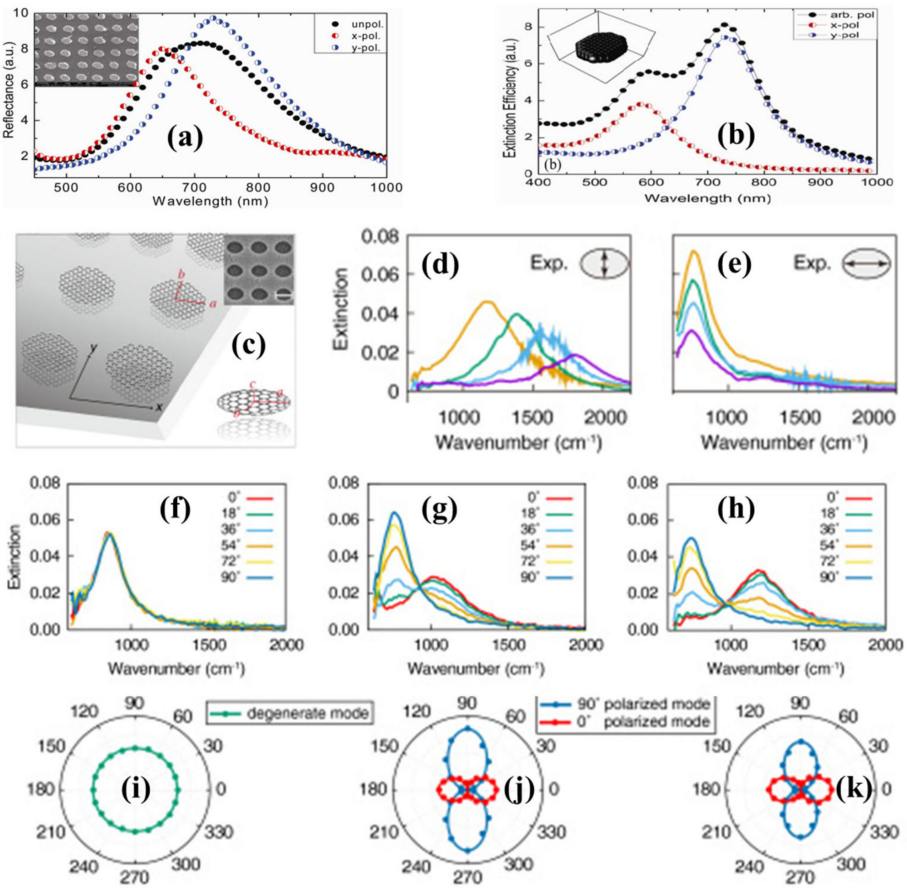

Figure 6. (**a**) The reflectance spectra of an array of ellipsoidal Au nanoparticles with axes of 80 and

110 nm, with a lattice constant of 200 nm over ITO coated glass under unpolarised illumination and linear polarisations parallel to short (x-pol) and large (y-pol) axes. The inset gives SEM images of the corresponding ellipsoid nanoparticle array. (**b**) DDA simulation results for the extinction efficiency of a single Au nanoparticle with 80 and 110 nm axes standing on ITO/Air interface. All the figures were reprinted (adapted) with permission from [65], Copyright 2010, The Optical Society. (**c**) The schematic diagram and the SEM image of periodic graphene ellipse arrays on BaF_2. The length of semi-major and semi-minor axes are a and b, respectively. Scale bar of the SEM image: 140 nm. Experimental extinction spectra at normal incidence with the polarisation along (**d**) minor and (**e**) major axes, respectively. From yellow line to purple line, the sizes of ellipse are a = 77:5 nm, b = 30 nm (orange); a = 72:5 nm, b = 25 nm (green); a = 67:5 nm, b = 20 nm (blue); a = 62:5 nm, b = 15 nm (purple), respectively. Polarisation-dependent extinction spectra of three different ellipticity structures. The extinction spectra of normal incident light with polarisations varied from 0° to 90° for (**f**) round graphene disk with 45 nm radius. (**g**) Ellipse with a = 70 nm, b = 38 nm; (**h**) ellipse with a = 70 nm, b = 32 nm. (**i**–**k**) are polar plots showing the extinction intensities for all polarisation direction of the two resonant plasmonic modes corresponding to (**f**–**h**), respectively. All the figures were reprinted (adapted) with permission from [66], Copyright 2019, The Optical Society.

2.6. Nanoprism and Nanotriangle

Triangular nanoprisms are a special type of plasmonic nanostructure where the combination of LSPR excitation and lightning rod effects leads to strong field enhancement [70,71]. Triangular Au and Ag nanoprisms hold advantages over flat and round surfaced nanostructures thanks to the presence of the sharp tips and edges, known as "hot spots" which favours strong enhancement in their LSPR [20,72] and allows high sensitivity to bulk and local dielectric changes. Several theoretical calculations by DDA simulation have shown the excitation of multipolar (l = 1, 2 and 3) LSPR modes in nanotriangles [20,73–75]. In their work, Félidj et al. [21] used far-field extinction spectroscopy to study in-plane multipolar LSPR modes on regular arrays of Au triangular particles (Figure 7a). Figure 7b depicts the extinction spectra corresponding to the arrays of different lateral size. For the array A with smallest lateral size, the LSPR response consists of a single peak at 590 nm, which is redshifted to 665 nm with increasing intensity for array B. With an increase in lateral size to arrays C and D, the first peak further redshifts with an additional weak peak appearing on the blue side of the spectrum. The strong peak in the longer wavelength regime is assigned to dipolar resonance (l = 1) while the weaker peak in the shorter wavelength regime is ascribed to quadrupolar mode (l = 2). It is shown that the theoretically calculated extinction cross-sections match well with the experimental results within ± 10 nm. For further large triangle of edge length a = 360 nm and grating constant of 840 nm (array E), l = 1 and l = 2 peak further redshifted to 974 and 672 nm while an additional new mode of l = 3 appears at 615 nm. In a rather unconventional work, Gao at co-workers [74] theoretically demonstrated that when the tips and edges, i.e., hotspots of lateral triangular nanoprisms are exposed to the environment directly, their LSPR characteristics are predominantly controlled by the polarisation over propagation.

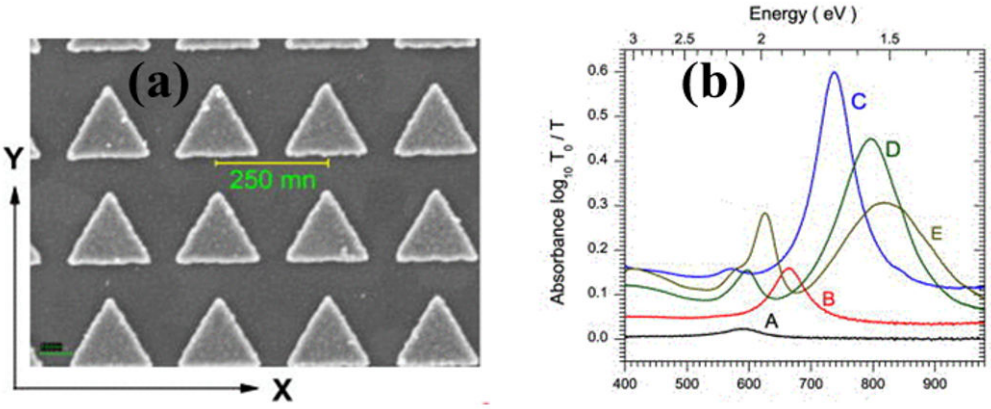

Figure 7. (**a**) Scanning electron microscopy image of the array A, constituted of gold nanotriangles on ITO. (**b**) Experimental extinction spectra of gold nanotriangles. The spectra correspond to triangle arrays with five different lateral sides. (A) 50 nm, (B) 100 nm, (C) 150 nm, (D) 200 nm, and (E) 260 nm. All the figures were reprinted (adapted) with permission from [21], Copyright 2008, American Institute of Physics.

2.7. Nanocrescent

Nanocrescents (NC) are a very special type of nanostructures which are fabricated using nanosphere template lithography (NTL) [76,77]. Bukasov and Shumaker-Parry [22] demonstrated that Polystyrene spheres (PS) of varying diameters can be exploited as templates to fabricate NCs with well-defined shape and size using NTL, as shown in Figure 8a–e. The NCs have sharp corners that can induce strong electromagnetic field enhancement. The LSPR of NCs is easily tunable by structural parameters like thickness, tip sharpness, tip gap angle, orientation [22,78]. Apart from that, due to the asymmetry of the crescent structure, LSPR is believed to be highly polarisation dependent. Figure 8f shows the extinction spectra consists of several peaks of the NCs produced from PS templates of different diameters [22]. For all the NCs the weakest peaks appeared in the visible range around 600 ± 50 nm range which is ascribed to the out-of-plane LSPR mode that is less sensitive to the NC orientation as well as to the incident polarisation. The dominating longitudinal LSPR peaks for all NCs appear in the longer wavelength side, e.g., at 2640 and 2470 nm for 410 and 356 nm diameter templates when the incident light is polarised along the long axis of the NC. On the other hand, transverse LSPR peak dominates for polarisation along the short axis of NC, e.g., 1450 nm peak for the templates of diameter 356 nm. Notably, both the longitudinal and transverse LSPR peaks of the NCs redshift with an increase in the template diameter as depicted in Figure 8g. The longitudinal LSPR peaks are found to be very sensitive to the incident polarisation as it reduced by 300–500% with unfavourable polarisation, while the transverse peaks are less sensitive which changes only by 10–30% against the variation of incident polarisation. In this regard, Cooper et al. [79] studied the polarisation sensitive LSPR response of open-structure NCs (Figure 8h). As shown in Figure 8i, LSPR extinction spectra of open-tip AuNCs upon unpolarised light excitation, consists of four distinct peaks, each of which is associated with particular mode.

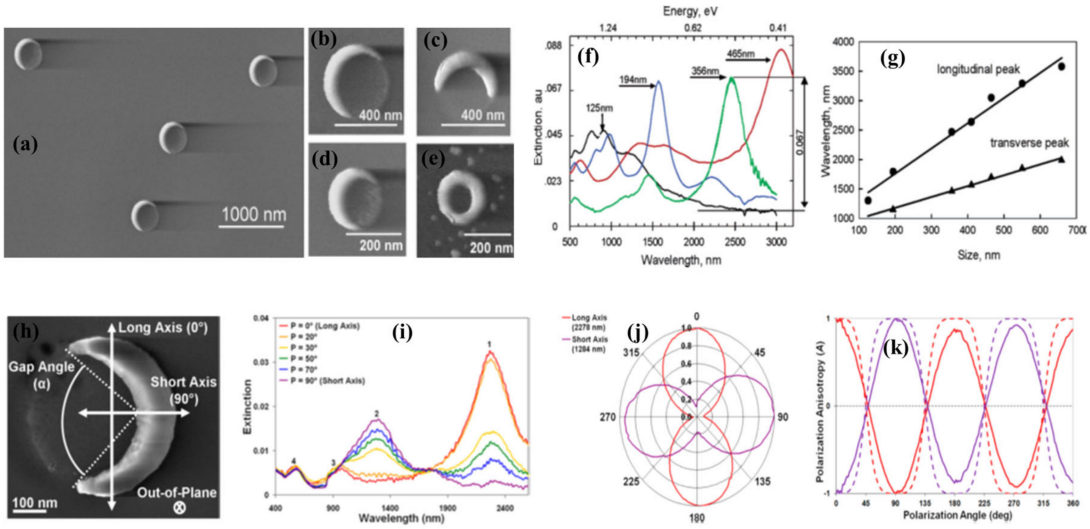

Figure 8. SEM images of nanocrescents template with PS beads with diameters of (**a**–**c**) 356 nm, (**d**) 194 nm beads, and (**e**) nanorings template with 125 nm diameter PS beads. (**f**) Ensemble extinction spectra with the PS bead template diameter shown near the longitudinal peaks. (**g**) The linear dependence of nanocrescent LSPR peaks on the diameter of the PS template used to fabricate the nanocrescents. All the figures were reprinted (adapted) with permission from [22], Copyright 2007, American Chemical Society. (**h**) Illustration of the direction of electric field polarisation with respect to nanocrescent axes for distinct resonance modes. (**i**) Extinction spectra of 356 nm diameter template AuNC. The varying polarisation angles (P) demonstrate selective excitation, co-excitation or non-excitation of resonances at specific angles. Peak labels correspond to unique resonance modes described in text: 1, long axis dipole; 2, short axis dipole; 3, long axis quadrupole; 4, out-of-plane dipole. (**j**) Polar plot of normalised extinction values for the LA-D (red) and SA-D (purple) resonance modes, demonstrating the anisotropy of 356 nm diameter AuNCs. (**k**) Experimental (solid) and calculated (dashed) polarisation anisotropy values (A) for LA-D (red) and SA-D (purple) resonances of the same AuNC sample. All the figures were reprinted (adapted) with permission from [79], Copyright 2013, American Chemical Society.

The peaks shown in Figure 8f under different polarisation can be assigned to particular resonance mode. The position of these peaks can be tuned by changing the angle between the incident light polarisation and the nanostructure orientation. By setting the incident light polarisation along the long and short axes of the nanocrescents, various resonance modes can be excited selectively and likewise can be assigned to long axis dipole (LA-D), short axis dipole (SA-D), long axis quadrupole (LA-Q), and out-of-plane dipole (OOPD) modes, as shown in Figure 8i. Both LA-D and LA-Q resonance modes are selectively excited when the incident light polarisation is along the long axis of the nanocrescent (0°). Notably, LA-D resonance mode shows strong electric field enhancement and appears between the near- to mid-infrared regime. On the other hand, the LA-Q mode is much weaker compared to LA-D and likewise produces a weaker peak with lower field enhancement. On the other hand, when light is polarised along the short axis (SA) of the nanocrescent (90°), i.e., orthogonal to LA, SA-D mode is excited, which is although strong, however less dominant than LA-D, thus not coupled with incident light most efficiently. The last one, i.e., out-of-plane weak dipole (OOP-D) mode can be excited irrespective of the incident polarisation, in a direction perpendicular to the plane of the nanocrescent around the visible wavelength range. Notably, while LA-D and SA-D modes redshift with increasing template diameter, OOP-D mode remains invariant against the variation of template diameter, similar to observations by Bukasov et al. [22]. The polarisation dependence of the nanocrescent LSPR can be visualised from the 360° polar plot as shown in Figure 8j. For LA-D mode maximum intensity is obtained for 0° and 180°, whereas SA-D shows maxima for 90° and 270°, thus indicates that these two modes are orthogonal to each other. Likewise, PA discussed before can be calculated for long axis

as $PA_{LA} = (I_{LA}-I_{SA})/(I_{LA}+I_{SA})$ [80]. Here I_{LA} and I_{SA} are defined as the normalised intensities of the LA-D and SA-D resonance modes, respectively, for any given angle. From Figure 8k it is apparent that both calculated and measured normalised extinction for LA-D mode at 2278 nm and SA-D mode at 1284 nm become 1 at 0° and 90° for PA_{LA} and PA_{SA}, respectively. In addition, Goerlitzer et al. [81] and Zhang et al. [82] also demonstrated that LSPR of NCs depends strongly on the polarisation of the excitation light.

2.8. Hybrid Plasmonic Nanostructures

The quest for an enhanced electromagnetic field with superior signal-to-noise ratio from the optical signal leads to the idea of engineered plasmonic nanostructures [83]. Two-dimensional (2D) materials, thanks to their reduced symmetry provides ample controllability over physical properties, thus become an ideal candidate in the field of optics, optoelectronics and nanophotonics [84–86]. The integration of a 2D material with a plasmonic nanomaterial leads to a new generation of hybrid nanostructures which can efficiently manipulate the light through LSPR, that leads to exotic spectroscopy enhancement phenomenon, including SERS, PL, enhanced transmission, etc. [87–89]. Among the family of 2D materials/plasmonic hybrid nanostructures, black phosphorus (BP) [90,91] and GaSe metal chalcogenides [92] need special mention thanks to their tunable optical, electrical and electronic properties. In a recent theoretical framework, Deng and co-workers [26] demonstrated that excitation of surface plasmon polaritons (SPP) at the metal/BP array interface leads to broadband enhanced transmission which is found to be strongly polarisation dependent because of the inherent anisotropy of BP structure, coming from x-(armchair) and y-(zigzag) directions. A schematic diagram of gold patch arrays with a BP sheet hybrid structure is shown in Figure 9a. Clearly in both x-(armchair) and y-(zigzag) directions, transmission enhanced significantly (Figure 9b) through gold slit arrays after the BP incorporation, when LSPR at gold/BP interface couples with the SSP modes of BP. Interestingly, enhancement of transmissions is strongly wavelength dependent and also occurs differently for different polarisations, which leads to anisotropic polarisation response.

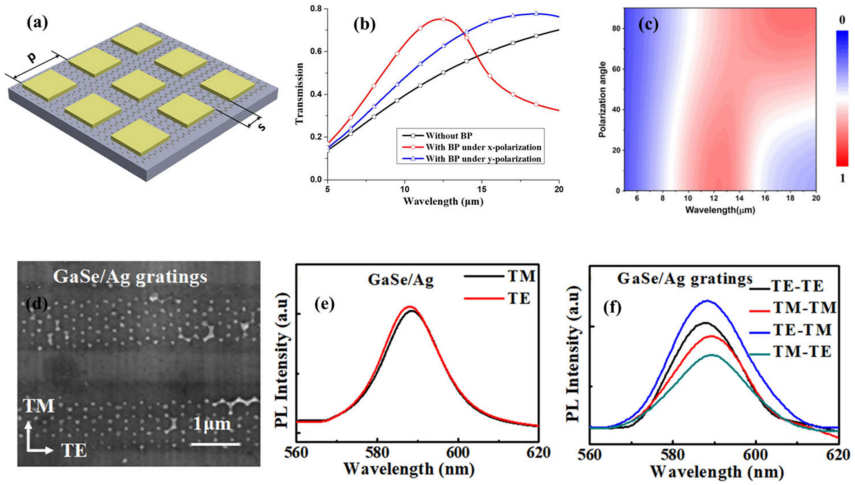

Figure 9. (**a**) Schematic of continuous BP sheet at the bottom of the gold patch arrays and (**b**) transmission of the structure with and without the BP sheet. (**c**) Transmission spectra of the gold patch arrays structures with BP under different polarisation angles. All the figures were reprinted (adapted) with permission from [26], Copyright 2019, The Optical Society. (**d**) SEM image of the Ag nanoprism gratings on GaSe layers. (**e**) Measured PL spectra with TM and TE polarisations for the normal GaSe/Ag hybrid structure. (**f**) Measured PL spectra for the GaSe/Ag grating structure, along two detection polarisation directions, TM and TE, with TM and TE excitation polarisations, respectively. The "TE−TE" ("TM−TM", "TE−TM", and "TM−TE") indicates the spectrum pumped with the TE (TM, TE, and TM) polarised incidence and detected along the TE (TM, TM, and TE) polarisation direction. All the figures were reprinted (adapted) with permission from [93], Copyright 2019, American Chemical Society.

To obtain a clear picture, Figure 9c shows the polarisation dependent transmission spectra at different wavelengths. It can be seen that for varying polarisation angle from 0° to 90°, at shorter wavelengths transmission slightly decreases, while transmission gets higher at longer wavelengths [26]. Such observation can be understood from wavelength dependence of x- and y-polarisation transmission. Below 15 µm, for both the x- and y-polarisation, the transmission with BP is almost indistinguishable. However, for above 15 µm, as the excitation of the propagating SPPs is not possible in the x-direction, transmission is reduced significantly. Nevertheless, transmission remains high in the y-direction (Figure 9b). Hence, a strong polarisation-dependent wave transmission is observed in the proposed hybrid nanostructures. In another similar work, Wan et al. [93] fabricated hybrid plasmonic nanostructures by designing a periodic array of Ag metallic nanostructures on typical 2D GaSe layers. Experimental results indicate that both SERS and PL signal enhanced significantly in the hybrid nanostructures compared to pristine one and the effect is found to be strongest for thinnest GaSe layer. Based on the plasmonic-enhanced optical response, they tried to manipulate the optical properties on the GaSe/Ag hybrid nanostructure. To realise the optical anisotropy, it is desirable to have broken structural symmetry in the x-y plane, which allows selective excitation of transverse and longitudinal surface plasmons by varying incident polarisation. For practical application, Ag nanoprisms with patterned gratings were imprinted on the GaSe layer, along the x axis with a periodicity of 1176 nm, which can be clearly seen from the SEM image in Figure 9d. To experimentally observe the optical anisotropy, PL spectra are recorded at TE ($\perp$ to x-axis)) and TM ($\parallel$ to x axis) polarisation as shown in Figure 9e,f. We learnt from Figure 9e that PL spectra in normal GaSe/Ag hybrid structure is polarisation-independent because of the presence of low anisotropy in geometric configuration. In stark contrast, a strong polarisation dependent PL spectrum is obtained for the GaSe/Ag grating structure. For example, under TM excitation polarisation, the PL at TM- and TE-polarised detections show a 9.3% polarisation which remains 8.2% for TE polarised excitation. Both the excitation and detection of PL signal show strong polarisation dependence which indicates anisotropic polarisation response. Precisely, for both TE and TM excitations, PL signals are detected to be higher along the TM polarisation [93]. On the other hand, when detected in two different polarisation directions, band edge emissions are more favourably excited for TE polarised excitation compared to TM polarisation. In short, polarisation sensitive, selective excitation and emission in GaSe/Ag grating structure confirms the role of Ag nanoprism gratings in inducing anisotropic plasmonic pumping in GaSe luminescence, which holds tremendous potential application in fabricating anisotropic 2D nanodevices.

2.9. Selected Applications

Manipulation of the polarisation state of light at the nanoscale by plasmonic nanostructures of various shape and size discussed above has led to notable applications in photonics, optoelectronic devices, plasmonic circuits and optical sensing techniques [94–98]. Of late, key functional elements of optoelectronic devices and nanophotonic circuitry have been realised utilising plasmonic structures, providing proof of principle devices at scales, which is otherwise not achievable with conventional photonics [95,99,100]. Plasmonics also continues to demonstrate progressing utility in biological and chemical fields, with plasmonic sensing methods providing single-molecule sensitivity at nanoscale dimensions [101–103]. The unique structural orientation and favourable polarisation direction of individual nanostructures have given rise to many diverse applications. For example, LSPRs in nanoparticles have been utilised to locally enhance Raman scattering, with dimer, trimer and quadrumer nanoparticle arrangements demonstrating confined Raman enhancement hot-spots, with marked polarisation dependence [104–106]. Nanorods, due to their polarisation dependent longitudinal LSPR modes, have been employed as orientation sensors, also allowing for precise alignment and rotation using polarised laser tweezer techniques [33,107]. Recently, one-dimensional nanowires have found wide-ranging applications, most notably in the development of novel plasmonic circuitry as plasmonic waveguides, routers, multiplexers and logic gates, etc. [60,100,108,109].

Photonic devices have been proposed as the foundation for the next generation of semiconductor-based computing thanks to their remarkable speed, bandwidth and energy efficiency as compared to their electronic counterparts. Plasmonic analogues of optical components can be replicated at nanoscale dimensions, and many of the functional elements required for plasmon-based integrated circuits have been developed recently, including Plasmonic waveguides, multiplexers, de-multiplexers, emitters, detectors, gain media and Boolean logic gates, etc. [60,100,108,109]. Among the variety of plasmonic nanostructures, Ag nanowires (NWs) are of particular interest because of the low loss propagation of surface plasmons (SPs) along the wire in the visible to near-infrared spectral range [110,111]. The coupling of far-field light to propagating SPs can be achieved when light is incident on metal NW terminals, allowing for subwavelength confinement as the SP travels along the NW before being emitted as a photon at the distal end. This in/out coupling process requires a scattering mechanism to take place and, as such, is found to occur only at areas of symmetry breaking within the wire, such as wire ends or sharp discontinuities [112]. Coupling of light to the AgNW in Figure 10a(i) by focused laser illumination is illustrated in Figure 10a(ii), launching a propagating SP that is re-emitted as scattered light from the NW terminal. These propagating SP distributions can be successfully imaged by coating the NWs with fluorescent quantum dots (QDs), which are excited by energy transfer from the propagating SPs [8]. Unique near-field distribution patterns are observed as a result of the superposition of different SP modes within the NW. It can be seen that these distributions change as the polarisation of the incident light is varied, with Figure 10a(iii,iv) demonstrating the patterns obtained for orthogonal polarisations using QD imaging.

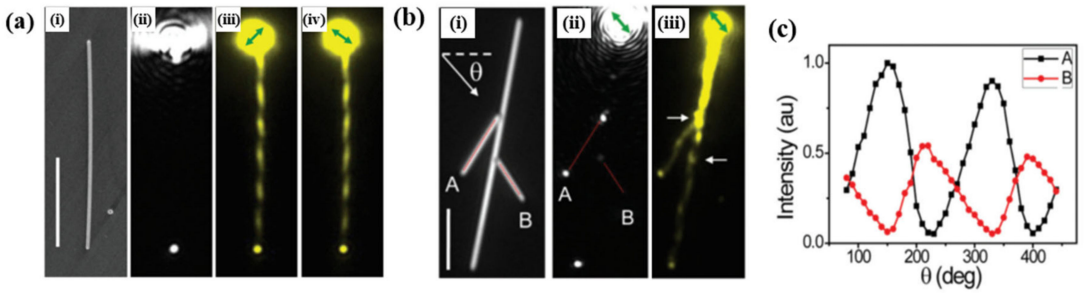

Figure 10. (**a**) (i) SEM image of an AgNW, scale bar is 5 μm. (ii) Scattering image during focused laser illumination of the NW terminal. (iii,iv) Quantum dot fluorescence imaging of the NW's propagating SP field distribution for different incident polarisations indicated by the green arrows. (**b**) (i) White light image, (ii) scattering image, and (iii) QD fluorescence image of a branched NW structure during polarised illumination. θ indicates the angle of polarisation of the incident light. (**c**) Output intensity of branch terminals A and B as the incident polarisation angle θ is varied. Selective routing into either branch can be achieved by tuning of the incident polarisation. All the figures were reprinted (adapted) with permission from [8], Copyright 2015, Royal Society of Chemistry.

Coupling of light to NWs at regions other than terminals or discontinuities is observed only as a result of near-field interactions and cannot occur through far-field illumination [61]. However, these near-field interactions were shown to facilitate the transfer of propagating SPs from one NW to an adjacent NW due to near-field coupling, allowing SPs to propagate through branched NW networks [60]. The successful coupling of propagating SPs from one NW to another depends on the near-field intensity at the junction between the two, with the SP either being routed into the adjacent wire or continuing in the original wire. The near-field patterns observed in these NWs are found to be strongly dependent on the polarisation of incident light. For example, the simple branched NW network shown in Figure 10b(i,ii) allows selective routing of propagating SPs into either branch A or B by tuning the incident polarisation. The near-field coupling to branch A from the main wire occurs due to the large near-field intensity at the junction between the two (marked by the upper white arrow in Figure 10b(iii)), while the weak near-field intensity at the junction with branch B (lower white arrow)

does not lead to successful coupling. Figure 10c shows the output intensity from both A and B as the polarisation is rotated. A polarisation angle of $\theta \approx 150^\circ$ exhibits a maximum scattering intensity from A and a minimum from B, while an angle of $\theta \approx 230^\circ$ exhibits a maximum from B and minimum from A, demonstrating the polarisation selective routing behaviour. The routing process is also found to be dependent on the incident wavelength, leading to light at different frequencies being routed into different branches within the network, allowing for de-multiplexing of multi-wavelength signals [60].

In another pioneer work, Wei and co-workers demonstrated that, in simple AgNW networks, interference of plasmons between primary and secondary/branched NWs modulates the near-field distribution to control the output optical signal, which can be exploited to realise the complete family of Boolean logic gates [108,113]. NW networks with two input terminals (I1 and I2) were used to combine propagating SPs within the main wire, where both the phase difference and polarisation angle led to interference that dictated the output (O) of the NW network as shown in Figure 11a. Polarisation control allows coupling between wires to be maximised while tuning the relative phase difference between the propagating SPs allows their interaction to lead to constructive or destructive interference. Specific input phase and polarisations demonstrate a maximum to minimum intensity ratio larger than 10, allowing for simple binary classification of 'ON' and 'OFF' states, and the performance of basic logical functions (Figure 11a). For example, when inputs I1 and I2, separately or together, leads to maximum output at O, an "OR" gate is realised. On the other hand, when the output signal is obtained only for individual inputs and disappears (OFF) when two SPs propagate together owing to destructive interference between them, the NW network behaves as XOR gate. Further complicated NW networks with two inputs, I1 and I2, and two output terminals, O1 and O2, (Figure 11b) are also exploited to realise the additional logic gates. It can be seen from Figure 11b that for simultaneous inputs from I1 and I2, the outputs O1 and O2 are complementary to each other. An "AND" gate can be realised by considering O2 as the gate output, setting the output intensity threshold for the 'ON' state to 450 au, and tuning the relative phase delay so that simultaneous inputs at I1 and I2 lead to a maximum output at O2. In this case, inputs at I1 and I2 individually lead to a sub-threshold output at O2 (~100 and ~350 au, respectively) yielding a 'low' output, but simultaneous inputs at I1 and I2 leads to an output at O2 that exceeds the threshold (~800 au) yielding a 'high' output. Similar four-terminal NW networks are also proposed to demonstrate other logical functionalities like 'NOT', 'NAND' and binary 'Adder' operations as illustrated in Figure 11c.

Wei et al. further demonstrated the ability of AgNW networks to cascade basic logic functions to create more complex logic functions [109]. In their work, a four-terminal branched AgNW network was exploited to realise a universal logical 'NOR' gate by cascading 'OR' and 'NOT' gates as illustrated in Figure 11d. Operation of both the 'OR' and 'NOT' gates can be tuned by varying the intensity, polarisation and phase of I1 and I2. The 'NOR' gate is illustrated by considering terminals I1 and I2 as inputs where C serves as control terminal which inverts the signal, resulting in the binary 'high/low' states. The first section of the network consists of a primary and branched NW, with inputs I1 and I2 that operate as an 'OR' gate (as before), with inputs from I1 and I2 separately or together leading to a 'high' output from the gate. The second section takes the output from the first and, using a control input C from the second NW branch, uses destructive interference to realise a logical 'NOT' gate, inverting the output of the 'OR' gate. The realisation of the 'NOR' gate can be understood clearly by looking into the scattering images of the NW network with different combination of the inputs I1, I2, and C as shown in Figure 11f–k. For example, following inputs from I1 and I2 separately or together, the output is 'high' (as depicted by the yellow circle), indicating the 'OR' functionality (Figure 11f–h). Alternatively, when I1 and I2 are 'low' and C is enabled, the network output is 'high', thus depicting the 'NOT' operation (i). Finally, the 'NOR' gate is demonstrated when the 'NOT' gate acts upon the 'OR' gate, i.e., when the output is inverted to 'low' with both or either I1 and I2 being 'high', due to the control input C (j,k).

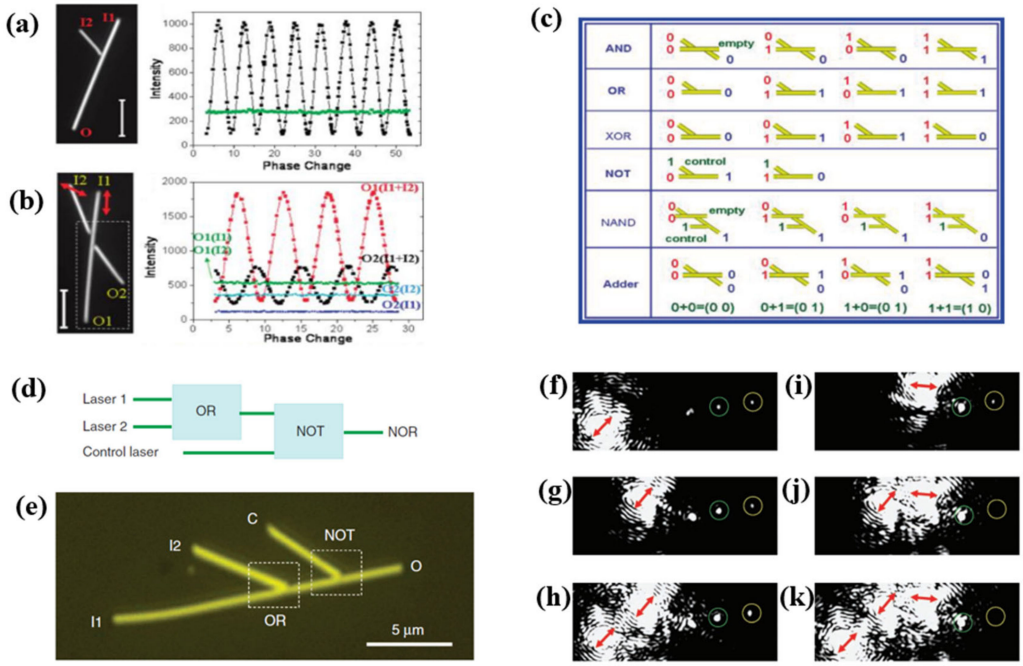

Figure 11. (**a**) Optical image of a simple branched NW network with two inputs (I1 and I2), and one output (O). The graph shows the output scattering intensity at O as a function optical phase delay when input is either I1 or I2 (green), and for simultaneous inputs I1 and I2 (black). Phase change does not impact output intensity for single inputs, however, for dual inputs, relative phase delay between I1 and I2 leads to interference that modulates the intensity at output O. (**b**) Optical image of a two-input (I1, I2) two output (O1, O2) NW network. The graph shows the variation in output intensity as a function of phase delay for both outputs with various input combinations. As before, no change in output intensity is observed as the phase of single inputs are varied (green, blue, dark blue). When propagating SPs are launched in both inputs simultaneously, the relative phase between I1 and I2 dictates the output intensity at O1 (red) and O2 (black). (**c**) Proposed schematics for various other interferometric logic operations in simple NW networks. All the figures were reprinted (adapted) with permission from [108], Copyright 2011, American Chemical Society. (**d**) Schematic of an optical cascaded logic gate in a four terminal AgNW network. (**e**) Optical image of the network. Propagating SPs can be launched at inputs I1 and I2 to perform the OR operation using phase-dependent interference before the output interferes with the control C to perform the interferometric NOT operation. (**f**–**k**) Scattering images illustrating the operation of the OR and NOT gates (with the green and yellow circles locating the outputs of the OR and NOT gates, respectively, while the red arrows indicate polarisation orientation). Launching propagating SPs at inputs I1 or I2 individually (**f**,**g**) or simultaneously (**h**) leads to a high output intensity from the OR gate. A low input to the NOT gate leads to a high output (**i**), while a high input leads to a low output (**j**,**k**). All the figures were reprinted (adapted) with permission from [109], Copyright 2011, Springer Nature.

'NOR' and 'NAND' gates are universal logic gates and form the foundation of Boolean logic networks central to electronic circuitry. Complex phase and polarisation dependent NW networks constitute a realistic route for plasmonic circuitry to overcome fundamental size limitations of optical computing devices, allowing for analogous plasmonic integrated circuits to be scaled down to sizes comparable with standard electronic ICs. Phase and polarisation dependent logic operations are a promising foundation for future on-chip integrated optical computing.

Manipulation of nanoscale objects by intense laser field through optical trapping and guided transport in plasmonic nanostructures has found tremendous applications in the field of hydrodynamics, microfluidics and lab-on-a-chip studies [114–117]. Strong electromagnetic field gradients and resulting optical gradient forces in localised LSPR of plasmonic nanostructures allows for trapping and

manipulation of nearby nano-objects. Several plasmonic nanostructures of different shapes have been proposed for trapping and guided transport of single nanoparticles [114–117]. However, we are particularly interested in the work by Yang et al. who demonstrated for the first time the guided transport of TiO_2 nanoparticles (NP) in AgNW in aqueous solution at single-particle levels with dedicated applications in microfluidics [118]. Using focused laser illumination of NW terminals, they successfully demonstrated the trapping of TiO_2 nanoparticles on NW surfaces in fluids. It was found that plasmonic trapping also leads to the transport of the nanoparticles along the wire toward the incident terminal. It is important to note that the nanoparticle trajectory is explicitly determined by the combination of the nanostructure shape and direction of incident laser polarisation. For example, in a V-shaped NW dimer, polarisation parallel to the left branch of the NW induces the movement of the NP along the left branch only (Figure 12a), whereas polarisation parallel to the right branch guides the NP along the right branch only (Figure 12b). Far-field optical manipulation methods like laser tweezers have become widely used for particle trapping and transport, however, plasmonic nanostructures provide a route towards precise control at nanoscale dimensions, with a unique versatility provided by various nanostructure shapes.

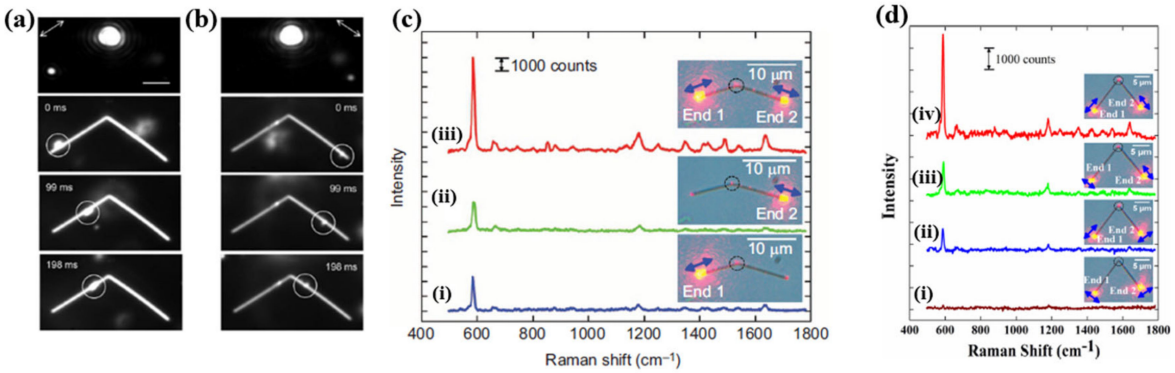

Figure 12. Images of trapping and guided transport of a TiO_2 nanoparticle along a v-shaped NW dimer structure (scale bar is 1 μm). Images in (**a**) illustrate the transport of a nanoparticle along the left branch for an incident polarisation orientation parallel to the left branch (marked by the white arrow). Images in (**b**) demonstrate transport along the right branch for orientation parallel to the right branch. Transport can be tuned to either the left or right branch by varying the incident polarisation. All the figures were reprinted (adapted) with permission from [118], Copyright 2016, Royal Society of Chemistry. Similar NW dimer structures were used to perform polarisation tuneable Remote SERS. (**c**) Comparison of the Remote SERS signal generated in NW dimer structures when propagating SPs are generated in (i) the left branch only (8 mW), (ii) the right branch only (8 mW) and (iii) both branches simultaneously (4 mW per branch). Incident polarisations are marked by the blue arrows. (**d**) Tuning of SERS signal intensity by varying the incident polarisation orientations. (iv) Polarisations parallel to their respective branches generated the greatest signal enhancement, whereas enhancement was reduced when polarisation in one branch was perpendicular (iii,ii), with the enhancement effect disappearing when both polarisations were perpendicular to their respective branches (i). All the figures were reprinted (adapted) with permission from [119], Copyright 2013, American Institute of Physics.

Plasmonic nanostructures have also led to notable advancements in various biosensing techniques [98]. Most notably, Surface Enhanced Raman Spectroscopy (SERS) has demonstrated the practical abilities of plasmon based sensing methodologies and has been shown to provide up to a 10^{10}–10^{11} enhancement over conventional Raman Spectroscopy [120–122]. Plasmonic nanostructures have been utilised as SERS probes for nanoscale Raman measurements, as LSPRs provide enhanced electromagnetic field strengths in nanoscale hot-spots regions. SERS has also been employed in NW structures, utilising propagating surface plasmons to transport incident light and perform Raman spectroscopy at distances several microns from the laser illumination. Remote SERS, while weaker than conventional SERS methods, provides notable advantages as the nanoscale volume probed avoids

background noise due to the incident illumination while also isolating heat from the incident light source reducing photodamage experienced by samples at high illumination intensities [123]. Following the work by Dasgupta and co-workers, two AgNWs are coupled serially to form a NW-dimer, where remote SERS is achieved by performing dual-path illumination at both distal ends of the NW-dimer [119]. They observed that the SERS signal was enhanced significantly when propagating SPs were excited simultaneously in both NWs (dual-path) compared to single-path excitation, at identical excitation powers. This observation can be understood clearly from Figure 12c, where single path excitation was performed in each branch with an incident power of 8 mW (i,ii), before dual-path excitation was performed by exciting both branches simultaneously with 4 mW laser power (iii). Dual-path excitation led to a 70% enhancement in the SERS signal when compared to single-path excitation with the same total excitation power.

This dual path SERS enhancement was found to be strongly dependent on the incident polarisation of both excitation beams. For polarisation perpendicular to the NWs (Figure 12d(i)), no SERS signal is obtained. Rotating the polarisation parallel to either of the NW branches led to a noticeable signal enhancement (ii, iii), however, a maximum SERS enhancement was observed only when both incident polarisations were parallel to their respective NW branches (iv). Tuning of the incident polarisations alters the near-field intensity at the junction hot-spot, allowing for control and modulation of the SERS intensity generated at the junction between wires.

Polarisation sensitive optical response of plasmonic nanostructures have also been proposed for use in novel SERS-based security labels [124,125]. These labels are constructed from arrays of short Ag coated plasmonic NWs orientated orthogonally in specific pattern designs, with embedded molecular probes that allow information to be read out through pixel-by-pixel SERS analysis of the target molecules. The polarisation dependence of these nanostructure arrays allows separate images to be simultaneously encoded and later revealed through polarised SERS imaging. The pixel-by-pixel SERS response for an individual NW coated in 4-MBT target molecules for horizontal and vertical polarisations is shown in Figure 13a,b, with the SERS intensity being collected from the 1079 cm^{-1} band. 2D SERS imaging shows a strong Raman enhancement around the edges and tips of the NW for horizontally polarised light, while for vertically polarised light enhancement is only seen at the NW tips. Figure 13c–f represents a few examples of custom made plasmonic nanostructures that demonstrate the capacity for covert security labels based on polarisation sensitive SERS imaging. Simple arrays in (c) show how horizontally polarised light (ii) leads to illumination of vertically aligned NWs, while vertically polarised light (iii) leads to illumination of horizontal NWs. Orthogonally polarised SERS imaging allow specific designs to be separately resolved by selective excitation of horizontal or vertical NWs (d,e). Based on this idea the images in Figure 13f demonstrate a more sophisticated encryption of molecular information from complex plasmonic structures composed of horizontal and vertical NWs. In short, SERS based plasmonic structures demonstrate the capacity to be utilised as advanced anti-counterfeiting labels for next-generation securities that are difficult to replicate yet easily verified.

Other than the NW structures described above, basic nanoparticle dimer, as well as trimer and quadrumer structures have shown to create polarisation dependent local hot-spots in the region between nanoparticles due to plasmonic coupling within sufficiently close interparticle separation [102,104–106]. Nanodisk Au dimers, for example, have been used to design nanoscale plasmonic cavities in which SERS measurements of graphene suspended on cavity exhibits an enhancement of 10^3 within the cavity [126] for certain polarisations. The sample configuration is depicted in Figure 13g. It is also shown that the SERS signal depends strongly on the incident polarisation of 638 nm excitation (Figure 13h,i). For polarisations parallel to the nanodisk dimer axis, 2D Raman peak (2670 cm^{-1}) exhibits strong enhancement and reaches a maximum (Figure 13h). However, when the polarisation is rotated by 90° the nanodisks get decoupled and as the localisation is lifted, Raman signal (Figure 13i) drops by a factor of 20.

Anisotropic polarisation responses of plasmonic nanostructures have also found applications as novel orientation sensors DF microscopy at single-particle level [107]. For example, LSPR scattering of Au nanorods shown in Figure 14a is strongly polarised along the long axis of the nanorod, which makes them an ideal candidate for orientation sensors. At the same time, AuNRs demonstrate compelling advantages over conventional fluorescent methods, based on fluorophore dyes in terms of the photostability of the scattering intensity.

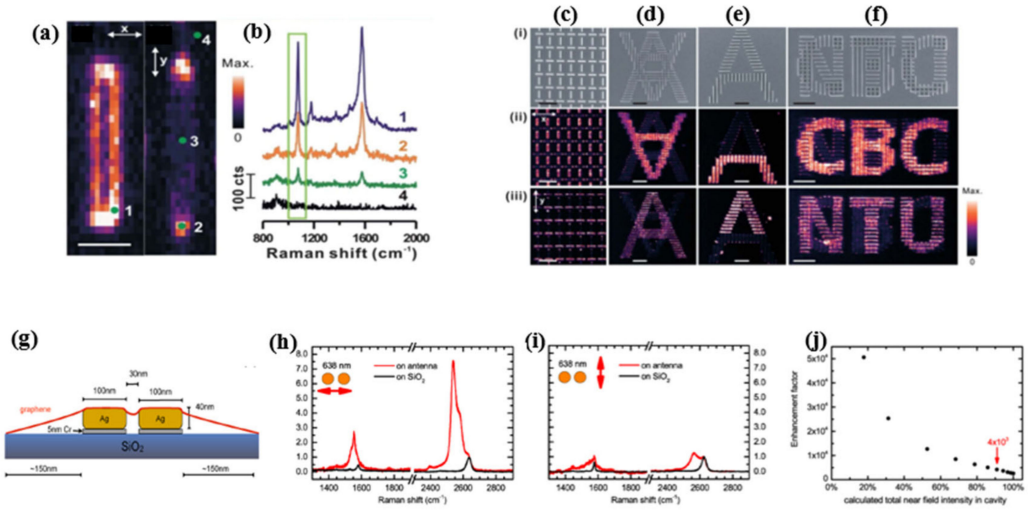

Figure 13. (**a**) SERS imaging of a single Ag NW under horizontal and vertical polarised light (scale bar is 1 µm). The NW is coated in 4-MBT target molecules, and the pixel intensities in the image are collected from the 1079 cm^{-1} band of the SERS spectra. (**b**) The SERS spectra obtained at points 1, 2, 3 and 4 in (**a**), demonstrating much stronger enhancement for light polarised perpendicularly to the NW. (**c**–**f**) Encrypted designs formed from horizontal and vertical AgNWs (scale bar is 1 µm). (i) SEM images, (ii) horizontally polarised and (iii) vertically polarised SERS images. All the figures were reprinted (adapted) with permission from [124], Copyright 2014, Royal Society of Chemistry. (**g**) Diagram of the polarisation dependent nanodisk dimer structure with the Raman hot-spot located in the nanogap between disks. (**h**,**i**) SERS spectra obtained from the hot-spot region for polarisation parallel and perpendicular to the longitudinal dimer mode at an incident wavelength of 638 nm. Maximum enhancement is obtained when the longitudinal LSPR of the dimer structure is excited with parallel polarisation, with this enhancement reducing when polarisation is orientated perpendicular to the long dimer axis and the nanodisks de-couple. (**j**) The enhancement factor is calculated by estimating the calculated integrated near-field intensity within the cavity and comparing it to the laser spot size. Here, the nanogap region is estimated to account for 90% of the enhancement, leading to a local enhancement factor of 4×10^3 for polarisations parallel to the longitudinal dimer mode. All the figures were reprinted (adapted) with permission from [126], Copyright 2013, American Chemical Society.

For plasmonic AuNRs, scattering intensity remains constant over the period of measurement (Figure 14b), whereas fluorescent dyes and quantum dots suffer from photobleaching, thereby reducing the emitted intensity over time and limiting timescales over which images can be recorded. For Au nanorods, the scattering intensity (I_{sca}) recorded for a certain polarisation orientation is proportional to the square of the cosine of the angle θ between the rod's longitudinal axis and the incident polarisation. The NR orientation can, therefore, be back-calculated from the recorded intensity, where $\theta = \arccos\left(\sqrt{I_{sca}}\right)$, and monitored as the NR rotates (Figure 14b).

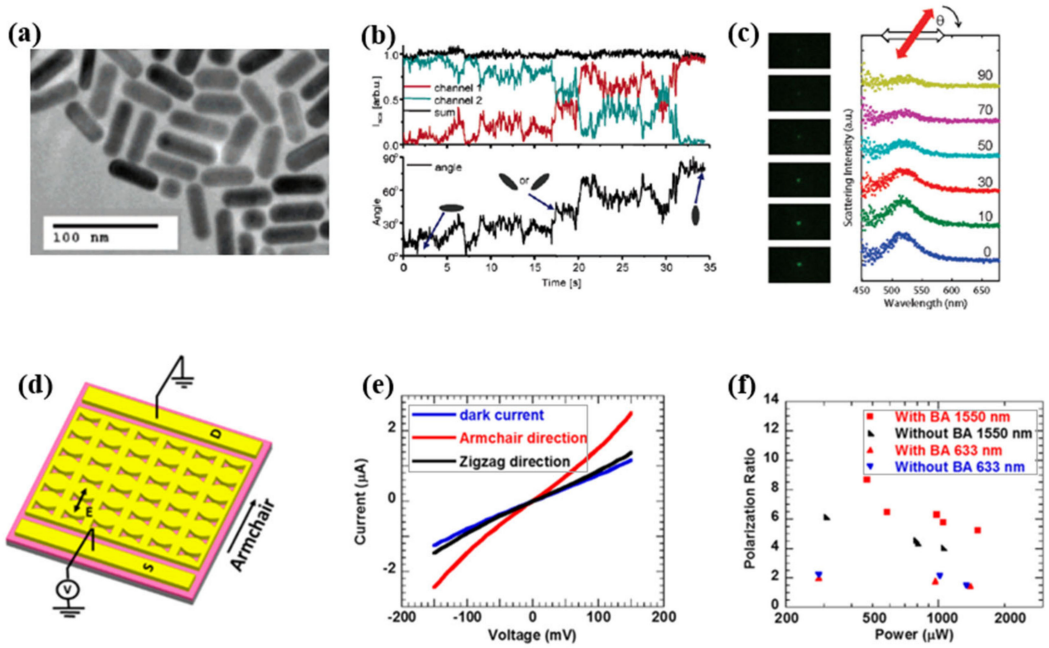

Figure 14. (**a**) SEM image of the Au nanorod orientation sensors (**b**) Scattered light intensity time traces recorded for orthogonal polarisations (channels 1 and 2) observed during DF imaging of a single rotating Au nanorod. Maximum signals are recorded in a channel when the nanorod orientation is parallel to the channel's polarisation axis. The sum of both channels illustrates a constant scatter intensity as the nanorod rotates. From these intensities, the orientation angle can be calculated. All the figures were reprinted (adapted) with permission from [107], Copyright 2005, American Chemical Society. (**c**) DF images and corresponding scattering intensities of an AgNR rotated using a polarised laser tweezers. A maximum intensity is recorded when the angle θ between the nanorod and the illumination polarisation is 0° (blue line), decreasing as θ increases, and reaching a minimum when θ is 90° (yellow line). As such, NR rotation and alignment using focused tweezers can be investigated and verified. All the figures were reprinted (adapted) with permission from [33], Copyright 2010, American Chemical Society. (**d**) Diagram of the polarisation-sensitive BP hybrid plasmonic photodetector. (**e**) Photodetector current vs. applied voltage for no illumination (blue), illumination polarised in the armchair illumination (red) and polarised in the zigzag direction (black) at 580 μW (1550 nm wavelength). (**f**) Polarisation ratios (photocurrent for armchair to zigzag directions) for various illumination powers at 150 mV bias. At 1550 nm illumination, devices with the bowtie apertures (BA) show an increased polarisation ratio compared to those without. This effect is wavelength dependent as 633 nm illumination shows similar ratios with and without the plasmonic apertures. All the figures were reprinted (adapted) with permission from [127], Copyright 2018, American Chemical Society.

Optical alignment and rotation of nanostructures has also been demonstrated using polarised light, as structures with one dominant LSPR mode, such as the long-axis longitudinal mode in nanorods, tend to align parallel to the incident laser polarisation [33]. Tong et al. utilised this phenomenon to rotate and align Ag nanorods using polarised laser tweezers. Rotation of the incident laser polarisation induces similar rotation of the AuNR to maintain alignment, which was verified using polarised white light DF imaging (Figure 14c). Maximum scattering is observed when the NR is orientated parallel to the white light polarisation, whereas for perpendicular polarisations, it reaches a minimum. Precise control and rotation of nanostructures allow nanoscale manipulation which may aid in the construction of nano-architectures, the driving of nano-pumps in fluidic devices, or even the testing of particle adhesion through rotational forces.

Polarisation sensitive LSPR response of hybrid plasmonic nanostructures discussed earlier have also found tremendous potential applications. For example, enhanced light absorption in 2D materials leads to enhanced performance of 2D devices [128]. Likewise, very recently Venuthurumilli et al.

demonstrated that hybrid plasmonic nanostructures made from Black Phosphorous (BP) that can be exploited for polarisation dependent photodetector devices to enhance polarisation sensitivity at NIR wavelengths [127]. Their design consists of bowtie nanoapertures in gold film deposited on 2D BP materials (Figure 14d) to enhance the photocurrent ratio of orthogonal polarisations in BP photodetectors. BP has gained interest for use in photodetectors owing to its thickness-dependent direct bandgap, while its intrinsic anisotropic properties, i.e., linear dichroism arising from its higher absorption along armchair axis compared to its zigzag axis, have been exploited for polarisation-sensitive detection [129]. The bowtie apertures utilised in the hybrid devices (Figure 14e) also exhibit polarisation dependence, allowing transmission of light polarised along the aperture's short-axis while suppressing light polarised along the aperture's long-axis [130]. By orientating the aperture's long-axis parallel to the BP's zigzag axis they further suppress the absorption in the zigzag direction, thus leading to an enhanced polarisation ratio (armchair to zigzag) for the photodetector. Measured currents through the photodetector are notably enhanced when the detector is illuminated with 1550 nm light polarised in the armchair direction, with little enhancement along the zigzag direction (Figure 14e). The polarisation ratio (defined as the ratio of photocurrent in the armchair direction to that in the zigzag direction) was then investigated for various illumination powers (Figure 14f) with and without bowtie apertures (BA). In general, the polarisation ratio is seen to decrease as the illumination power increases (possibly owing to saturation of the photocurrent in the armchair direction) for both structures with and without BA. Comparing structures with and without BA, the polarisation ratio in the device exhibits an increase from 4 without BA to 5.8 with BA at 1.05 mW illumination. At a lower power of 470 mW, the ratio reaches an even higher value of 8.7 for BA structures. For applications with lower power requirements such as IR polarimetry imaging, hybrid nanostructures provide avenues for enhanced sensitivity and selectivity for novel optical devices.

Plasmonic nanostructures provide unprecedented access to light manipulation at nanoscale dimensions while demonstrating the flexibility and control required for advancing photonic technologies. Continued research has motivated advances in optoelectronics, integrated photonics, telecommunications, biological sensing and nanoparticle manipulation, both furthering fundamental research and presenting proof of principle devices. Nanoparticles and nanostructures serve as optical antennas, exhibiting strong local field enhancements while plasmonic nanowires serve as novel waveguides and plasmon routers allowing for sub-wavelength manipulation and transport of light. The polarisation dependent responses of many nanostructures have brought about novel techniques to control and tune plasmon propagations and interactions, while also providing access to sensitive information through optical probing. The continued development and optimisation of plasmonic devices promises further advances in efficiency and sensitivity while continuing to integrate Plasmonics into conventional applications. Plasmonics promises to be at the centre of many notable future advances in optics, providing a realistic route toward the next generation of optical technologies.

3. Manipulating Polarisation State via Metamaterials

Polarisation state is an important characteristic of electromagnetic waves (EMW) which serves as a cornerstone in many optical phenomena. Therefore, the ability to control the polarisation state of EMW has attracted tremendous potential applications in the field of optical polarisation and wavefront manipulation [131,132], optical communication [133], THz photonics [134,135] and spin-hall effect of light [136,137], etc. Conventionally, bulky waveplates made of birefringent crystalline solids [138] or liquid crystals [139] are exploited to manipulate the polarisation state of the EMW. However, due to their large size, operational bandwidth, their application gets limited in optical system miniaturisation and integration. Therefore, it remains an important challenge to manipulate the polarisation state of the EMW at nanoscale for applications in nanophotonics.

Recently, after the emergence of metamaterials, we can unprecedently control the EMWs over a broad wavelength range from microwave to optical frequencies with multiple degrees of freedom e.g., polarisation, phase, and amplitude, which was beyond the scope of natural materials [140–142]. Similar

to metamaterials, their two-dimensional counterpart, single-layered nanostructured metasurfaces also provide adequate functionalities of polarisation manipulation in an ultrathin, planar platform [143–145]. In comparison to the volumetric metamaterial, fabrication of metasurfaces requires less complexity and also, they offer reduced loss. To date, although different anisotropic building blocks including crossed nanodipoles [146,147], nanorods [148], L- or S-shaped nanostructures [149–151] and elliptical nanoholes [67] have been employed to fabricate metasurfaces-based waveplates to manipulate the polarisation state of the EMWs, they suffer from the optical anisotropy of the individual building blocks which ends up with limited bandwidth and low efficiency. Chiral metamaterials require special mention because they can arbitrarily manipulate polarisation state of EMWs at nanoscale by combining additional mirror symmetry breaking and by taking advantage of the fact that chirality in EM resonance is handedness sensitive [152,153]. In the second part of the review, we will discuss the designing of metamaterials to control or switch the polarisation states of light, for example by rotating linearly polarised light, ellipticity and chirality, etc.

In a recently published book chapter in 2017, Chen et al. [30] have demonstrated some of the important aspects of polarisation manipulation which we will discuss briefly in the following section. Jiang and co-workers [154] demonstrated anisotropic metasurface of nanorod resonators for high-efficiency, angle-insensitive polarisation rotation over a broadband wavelength regime. They design the metasurface structures by optimising by tailoring the interference of light at the subwavelength scale and the metasurface-based half-wave plate (HWP) and quarter-wave plate (QWP) work over large bandwidth from 640 to 1290 nm near-visible to IR regime, which converts linear polarisation to its cross polarisation and circular to linear polarisation, respectively. The book chapter also includes the observation of Kruk et al. [29], who designed and demonstrated transparent all-dielectric metadevices for highly efficient polarisation manipulation based on HWP and QWPs that can operate across several telecom bands. Their system has an advantage to interact with electromagnetic waves at extremely confined spots without any heat dissipation. Their work paves the idea of reflection-less HWP, QWP and q-plates with high transmittivity that can operate across multiple telecom bands with ~99% polarisation conversion efficiency. Similarly, Wu and colleagues [155] experimentally demonstrate Fano resonances with quality factors as high as Q > 100 in silicon-based planar chiral infrared metasurfaces. They further demonstrated that by designing silicon-based metasurfaces planar (2D) chiral metamaterial high (50%) linear-to-circular polarisation conversion efficiency can be achieved experimentally.

3.1. Multifunctional QWP

Chiral metamaterials designed so far have been exploited for a specific functionality to do with rotating LP, ellipticity of handedness of circularity. In a very recent work, Liu and co-workers [145] inverse designed chiral material with multifunctional polarisation manipulation including Meta-quarter-wave plate (Type 1), bifunctional chiral metamaterial (Type 2) and abnormal meta-quarter-wave plate (Type 3), all of which we will discuss in this section. The results are validated through theoretical calculation, numerical simulation and experimental measurements. They inverse designed the cascaded chiral metamaterials for different polarisation controls, starting from the scattering matrix $\boldsymbol{S}$, defining the scattering properties of metamaterials. For an incident wave along j-polarisation, the reflection and transmission coefficients along i-polarisation are denoted as r_{ij} and t_{ij}. The forward (T_f) and backward (T_b) propagating transmission matrices are expressed as:

$$T_f = \frac{1}{\sqrt{2}} \begin{pmatrix} 1 & e^{j\theta} \\ -i & e^{j(\theta+\frac{\pi}{2})} \end{pmatrix} \tag{1}$$

$$T_b = \frac{1}{\sqrt{2}} \begin{pmatrix} 1 & -i \\ e^{j\theta} & e^{j(\theta+\frac{\pi}{2})} \end{pmatrix} \tag{2}$$

Here θ is arbitrary real number and by choosing several typical values of θ, the metamaterials will be exploited for abundant functionalities of polarisation control. To quantitatively evaluate the performance of the metamaterials as an m-QWP, first the Stokes parameters are introduced as [156]:

$$S_0 = |t_x|^2 + \left|t_y\right|^2,\ S_1 = |t_x|^2 - \left|t_y\right|^2,\ S_2 = 2|t_x|\left|t_y\right|cos\Delta\varphi \text{ and } S_3 = 2|t_x|\left|t_y\right|sin\Delta\varphi \quad (3)$$

Here $|t_x|$ and $\left|t_y\right|$ are the amplitude of transmitted electric fields along x and y directions and $\Delta\varphi = \angle t_y - \angle t_x$ is transmission phase difference. The ellipticity angle χ is defined as:

$$\chi = \frac{1}{2}\arcsin(S_3/S_0) \quad (4)$$

When χ is ±45°, the transmitted waves are perfect RCP and LCP, whereas χ = 0° represents a LP wave. In the following section, we will discuss three extreme cases of polarisation control:

Type 1. Meta-quarter-wave plate ($\theta = -\pi/2$)

When the variable $\theta = -\pi/2$, the forward and backward propagating matrices are expressed as:

$$T_f = T_b = \frac{1}{\sqrt{2}}\begin{pmatrix} 1 & -i \\ -i & 1 \end{pmatrix} \quad (5)$$

Type 2. Bifunctional chiral metamaterial ($\theta = 0$)

For this functionality, a four-layer chiral metamaterial (FLCM) is inverse designed by combining two TLMs which are oriented from each other at a twist angle of 45° and separated by an identical dielectric broad. For $\theta = 0$, the forward and backward propagating matrices are expressed as:

$$T_f = \frac{1}{\sqrt{2}}\begin{pmatrix} 1 & 1 \\ -i & i \end{pmatrix} \quad (6)$$

$$T_b = \frac{1}{\sqrt{2}}\begin{pmatrix} 1 & -i \\ 1 & i \end{pmatrix} \quad (7)$$

Equation (6) reveals that for forward propagating LP waves, m-QWP is realised for linear-to-circular polarisation conversion. On the other hand, following Equation (7) the structure works as a 45° polarisation rotator for backward propagating LP waves. It is quite evident from Figure 15b that for the forward propagating LP waves in x- and y-directions, both co-($\left|\vec{t_{xx}}\right|$, $\vec{t_{yy}}$) and cross-polarised transmission ($\left|\vec{t_{yx}}\right|$, $\left|\vec{t_{xy}}\right|$) exhibit high transmission of 0.7, which makes the total transmission $\left|\vec{T_x}\right|$ and $\left|\vec{T_y}\right|$ close to 1.

Likewise, a traditional m-QWP is realised that converts x- or y-polarised waves into LCP or RCP waves, for both forward and backward propagation direction. The m-QWP can be designed from a two-layer metamaterial (TLM), by keeping two metallic split ring resonators (SRRs) on each side of an F4B board. The schematic diagram of such optimised unit cell structure is shown in Figure 15a(i). Simulated results show that for normal incident LP waves, the co-polarised transmissions are greater than 0.8 (Figure 15a(ii)) with zero cross-polarisation transmission coefficients because of the mirror-symmetry of the TLM structure with respect to x-z plane. Figure 15a(iii) shows that the phase difference $\angle t_y - \angle t_x$ is ~90° ± 10°. Figure 15a(iv) illustrates that the simulated ellipticity angle χ > 40° is within the broadband frequency range of 10.5–12.5 GHz. This clearly demonstrate a nearly perfect high transmission RCP wave output, for an incident LP wave at 45° with respect to the x and y axes.

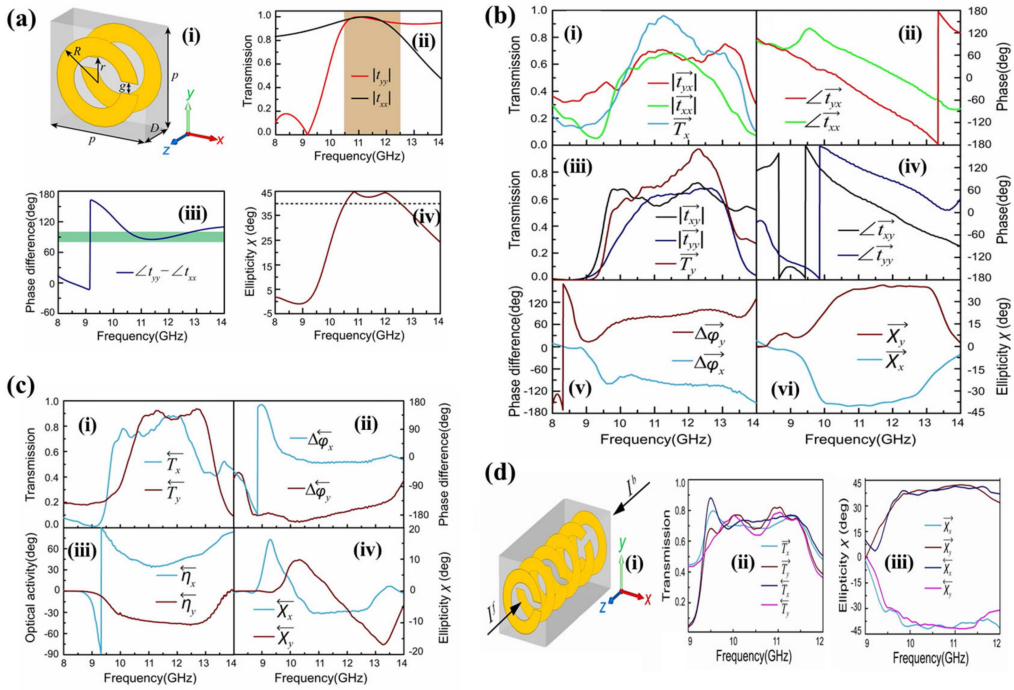

Figure 15. (**a**) (i) TLM as an m-QWP. The Schematic and geometric dimensions of the unit cell: p = 7.0 mm, D = 3.5 mm, r = 1.75 mm, R = 3.0 mm, and g = 0.75 mm. (ii) Simulated transmission spectra and (iii) phase difference for x- and y-polarised incident waves. (iv) Calculated ellipticity angle χ. (**b**) Experimental results of the FLCM for the forward propagating x- and y-polarised waves. ((i) and (iii)) Transmission spectra, ((ii) and (iv)) transmission phases, (v) transmission phase differences, and (vi) ellipticity angles χ of the transmitted waves. (**c**) Experimental results of the FLCM for the backward propagating x- and y-polarised waves. (i) Transmission spectra, (ii) transmission phase differences, (iii) polarisation azimuth rotation angles η, and (iv) ellipticity angles χ of the transmitted waves. (**d**) Multilayer chiral metamaterial as an abnormal m-QWP. (i) Schematic of the unit cell. Experimental results of (ii) transmission spectra and (iii) ellipticity angles. All the figures were reprinted (adapted) with permission from [27], Copyright 2019, Springer Nature.

For x and y polarised LP waves, ellipticity angle χ was found to be −40° and 40°, respectively, therefore indicting nearly perfect LCP and RCP output wave. The phase difference of −90° ± 10° and +90° ± 10° for x and y polarised waves support the observation further. Experimental results match well with the simulation.

For backward propagating LP waves, following reciprocity theorem, when the propagation direction is reversed, although the transmission coefficients of co-polarisation remain unchanged, it gets interchanged for cross-polarisation. The experimental results in Figure 15c show that the transmission phase difference $\Delta\overleftarrow{\varphi}_x$ and $\Delta\overleftarrow{\varphi}_y$ are calculated to be 0° and −180°, polarisation azimuth rotation angle η is +45° and −45° and the ellipticity angle is ~−6.3° and 8.3°, and for x and y polarised waves, respectively, which indicates a nearly linear polarisation.

Type 3. Abnormal meta-quarter-wave plate ($\theta = \pi/2$)

When the variable $\theta = \pi/2$, the forward and backward propagating matrices are expressed as

$$T_f = \frac{1}{\sqrt{2}}\begin{pmatrix} 1 & i \\ -i & -1 \end{pmatrix} \tag{8}$$

$$T_b = \frac{1}{\sqrt{2}}\begin{pmatrix} 1 & -i \\ i & 1 \end{pmatrix} \tag{9}$$

Clearly, such structures can convert the forward x-polarised or y-polarised wave into LCP or RCP wave, respectively; while it realises an inverse function, i.e., converts the backward x-polarised or y-polarised wave into RCP or LCP wave, respectively.

To realise this functionality, three m-QWPs are cascaded together as shown in Figure 15d(i). Two of them form an m-HWP, that together with the back m-QWP, oriented at 45° from the x-axis, gives rise to mirror symmetry breaking in the propagation direction. In line with the predicted theory, experimental results shown in Figure 4 match with each other for the forward and backward propagating LP waves. As can be seen from the Figure 15d(ii–iii) that for forward propagating x and y polarised wave ellipticities are −40° and 40°, respectively, thus output waves are LPC and RCP, respectively, with very strong transmission efficiency over a broadband. In contrast, backward propagating x and y polarised wave ellipticities are 40° and −40°, respectively, i.e., polarisation conversation is reversed to RCP and LCP, respectively. The proposed chiral metamaterials in this study show potential advantages of high transmission, broad bandwidth, and multi-functionality, and may find potential applications in polarisation-controlled devices.

3.2. Linear to Cross Polarisation Conversion

The multifunctional structure proposed by Liu et al. [145] missed an important component of 90° polarisation rotation of LP waves. In this regard, Yuqian Ye and Sailing He [157] proposed a bilayer chiral metamaterial (CMM) to realise 90° polarisation rotation with a resonant polarisation conversion efficiency over 90%. Figure 16a shows the schematic diagram of one-unit cell of the present bilayered CMM, while the whole sample is composed of 20 × 20 unit cells as depicted by Figure 16b. In their experiment, the incident wave is polarised in x-direction and normally impinged on the sample. The experimental and simulation results are shown in Figure 16c. The co-polarised transmission (dotted blue line) defined by $|t_{xx}| = \left|E_x^{out}\right| / \left|E_x^{in}\right|$ is below −5 dB in the given frequency range which suppressed below −20 dB around 12 GHz (Figure 16c). On the other hand, the cross polarised transmission (dotted red line), defined as $\left|t_{yx}\right| = \left|E_y^{out}\right| / \left|E_x^{in}\right|$ exhibits a resonant peak around 11.4 GHz with maximum amplitude of -2 dB. This clearly indicates polarisation conversion efficiency of over 90% is achieved through the strong rotatory strength in this bilayered CMM. The simulated results shown by solid blue and red lines agree well with the experimental observation. To understand the polarisation rotation in detail, polarisation state of the transmitted signal is studied at six different frequencies as shown in Figure 16e. The polarisation spectrum is shown in Figure 16d.

At low frequency of 10 GHz the transmission is relatively low and the polarisation is slightly off the x-axis with an azimuth of 20°. As the frequency increases, transmission polarisation rotates counterclockwise towards the y-axis followed by increased transmission. At 11.86 GHz maximum transmission is obtained with a polarisation azimuth angle of 86°. With further increase in frequency transmission starts reducing. It is important to note that within the frequency range 11.66–12.10 GHz, output polarisation is aligned in the y-axis. Eventually, at higher frequency the polarisation reverses back toward the x-axis (Figure 16e) in line with the Gaussian profile of the polarisation azimuth spectra of Figure 16d. Such observation confirms the 90° polarisation rotation by the bilayered CMM. In this context, it is also important to mention that in addition to the chiral metamaterial described above, anisotropic metamaterials also can be used for highly efficient conversions from a linear polarisation to its cross polarisation as proposed by Chin et al. [158] and Cui et al. [159]. Following the work by Chin, as shown in Figure 16f that around 10 GHz frequency range, the field intensity of the cross polarisation is close to 0 dB (p1 to p2) and that of the original polarisation (p1 to p1) is less than −20 dB. Such observation clearly depicts cross polarisation conversions with high efficiency.

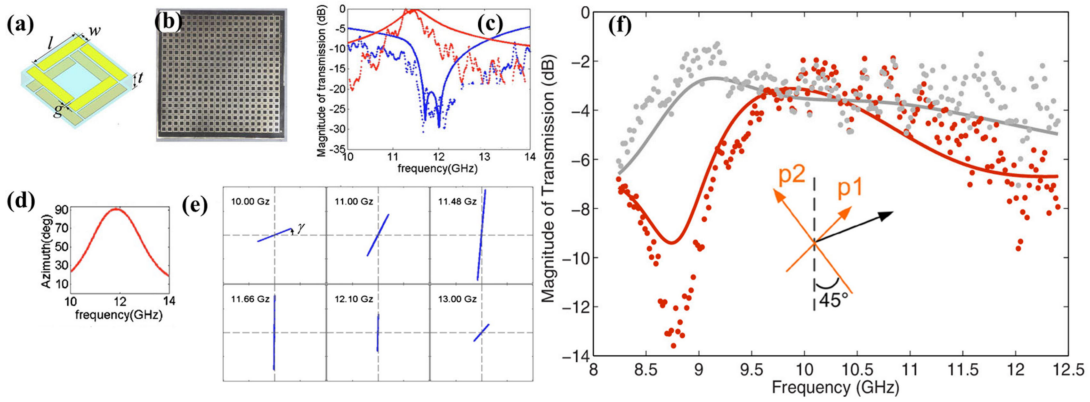

Figure 16. (**a**) Unit cell of the present bilayered CMM for transmission calculation. (**b**) The top view of the fabricated microwave-scale sample. (**c**) Co-polarised and cross-polarised transmission of electric field through the present bilayered CMM by both simulation (solid lines) and experimental measurement (dotted lines). (**d**) Polarisation azimuth of the transmitted wave as the frequency varies. (**e**) Polarisation states at six different frequencies. All the figures were reprinted (adapted) with permission from [157], Copyright 2010, American Institute of Physics. (**f**) The simulated (solid lines) and measured (dots) transmission of electric fields from p1 to p1 (yellow) and from p1 to p2 (blue). The inset shows the orientation for p1 and p2. All the figures were reprinted (adapted) with permission from [158], Copyright 2008, American Institute of Physics.

3.3. Linear to Left and Right Circular Polarisation Conversion

Most of the modern photonics devices are based on the terahertz (THz) technique with numerous significant applications, e.g., homeland security [160], communications and sensing [161], switching [162], etc. Therefore, it is desirable to design polarisation-controlling metamaterial in the THz regime to manipulate the polarisation state of THz wave and can be used as polarisers [163], a polarisation rotator [164] and waveplates [165], etc. Most of those structures suffer from low transmission, limited bandwidth, high cost, size constraint, etc. These shortcomings are overcome by Cong et al. [166] who designed broadband and highly efficient m-QWP fabricated on a free-standing flexible dielectric polymide layer that is sandwiched between the metamaterial layers (metallic grating) as shown in Figure 17a. The first metallic grating is oriented at −45° with respect to the x-axis, while the second one is along the x-axis.

In addition, the structure is further capped with two additional polymide layers on the top and bottom of the first and second metallic grating, respectively. For all experiments and simulation, the incident THz wave is linearly polarised along the x-axis. The experimental scheme is based on broadband THz time domain experiment. Similar to the work by Liu et al. [27] polarisation states are numerically determined by Stokes parameter [156]. The ellipticity χ is redefined as $\chi = S_3/S_0$, where χ = 1 and −1 represent LCP and RCP, respectively. It can be seen from Figure 17b that within 1–1.4 THz regime, orthogonal components of transmission, i.e., both co- and cross-polarised transmission, $\left|\vec{t_{xx}}\right|$ and $\left|\vec{t_{yx}}\right|$, respectively, have similar amplitude. In the same regime, the phase retardance data in Figure 17c exhibit around 90° (±5°) change, the signature of the functionality of QWP. The results are further substantiated with the ellipticity of $\chi \sim 0.99$ (Figure 17d) between 1 and 1.4 THz, thus depicting nearly perfect broadband LCP. To realise RCP, the first metasurface is oriented to 45°, to make the new m-QWP which is exactly the mirror-symmetry of the pristine QWP. The new QWP is named as negative m-QWP that can introduce −180°/180° phase retardance between the orthogonal components. It can be seen from Figure 17e that like the original m-QWP, orthogonal transmission components for negative m-QWP also reveal a similar transmission value. However, phase retardance is found to be -90° (Figure 17f) and ellipticity gives the value $\chi \sim -0.99$ (Figure 17g) over the broadband, the signature of RCP. The structure has an added advantage on the tunability of the operational THz

bandwidth which can easily be adjusted by changing the dimensions of the two metal strips. Apart from that, the structure is found to be very robust against crude handling which makes it ideal for practical device applications. It is important to note that broadband THz linear to circular polarisation conversation also has been theoretically demonstrated by Jiang and co-workers using monolayer black phosphorus (phosphorene) metamaterial [167].

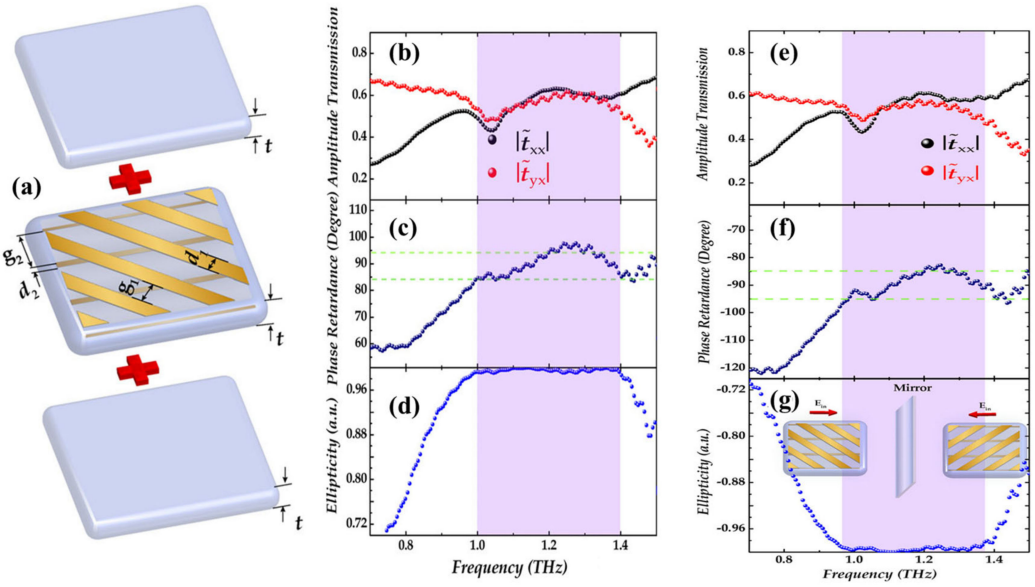

Figure 17. (**a**) Schematic diagram of the sandwiched metamaterial structure with labelled dimensions. (**b**) Amplitude transmissions (**c**) phase retardance between orthogonal components and corresponding (**d**) ellipticities change. (**e**) Amplitude transmissions (**f**) phase retardance between orthogonal components and corresponding (**g**) ellipticities change for the mirror symmetry sample shown in the inset of (**g**). All the figures were reprinted (adapted) with permission from [166], Copyright 2014, Wiley-VCH.

3.4. Circular Polarisation Conversion Using Helical Metamaterials

Thus, we are left with the one last important polarisation functionality of the metamaterial, i.e., the circular polarisation switching, in other words, conversion of the handedness of the circular polarisation, i.e., LCP to RCP or vice-versa. Helical metamaterials have been used extensively for this functionality because they exhibit inherent circular dichroism over an unmatched bandwidth above one octave. Depending on the handedness of the circular beam, a helix can either transmit or reflect the incident wave. When the handedness of the helix matches with that of the incoming circular beam, it gets reflected unperturbed whereas for opposite handedness no coupling takes place and light gets transmitted. Different helix structures have been proposed as circular polarisers with high extinction ratio and enhanced bandwidth in the mid-IR region. However, research on the asymmetric circular polarisation conversion has been started of late with generally very narrow operation bandwidths. There are very few experimental designs for circular polarisation conversions over broadband, however, conversion efficiency is well below 50% throughout the operational band, thus making the application limited. For example, Pan and co-workers [168] demonstrated circular polarisation conversion with 20% overall transmission (Figure 18a) using G-shaped chiral metamaterial whereas, Pfeiffer et al. [169] showed conversion from RCP to LCP with a low extinction ratio of 20:1 (Figure 18b). To overcome these shortcomings, Johannes Kaschke [28] proposed a novel helical metamaterial based on unit cells with a single helix. The uniqueness of the structure lies in the fact that the helix changes its handedness halfway through the helix axis. The device can perform high circular polarisation conversion (up to 80%) from RCP to LCP over a bandwidth of more than one octave.

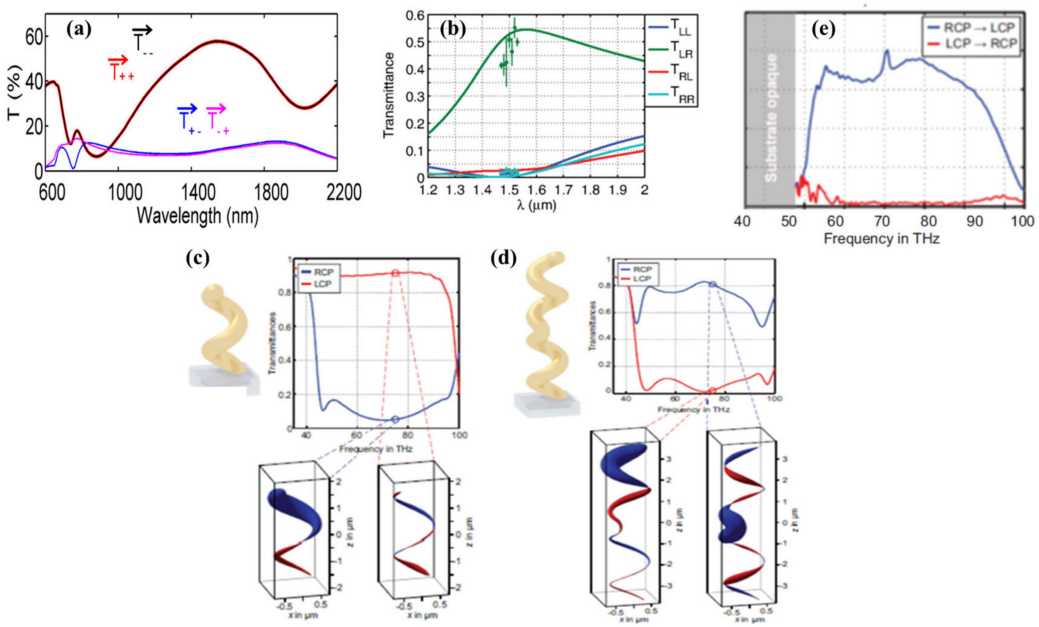

Figure 18. (**a**) Transmission spectra for circular polarisation conversion in G-shaped chiral metamaterial. All the figures were reprinted (adapted) with permission from [168], Copyright 2014, American Institute of Physics. (**b**) Measured (circles) and simulated (solid lines) Jones matrix of the bianisotropic metasurface. All the figures were reprinted (adapted) with permission from [169], Copyright 2014, American Physical Society. The top panels in (**c**,**d**) depict the numerically calculated transmittance spectra for both incident circular polarisations not differentiating between emerging polarisations. In the bottom panels, the calculated normalised current densities are shown for one frequency within the operation band (f = 75 THz). (**e**) Experimental data showing polarisation conversions. All the figures were reprinted (adapted) with permission from [28], Copyright 2015, WILEY-VCH.

To start with, for a single right-handed helix (Figure 18c) an incoming RCP light matches with the helix handedness, couples strongly to it and is reflected with the same handedness. On the contrary, for an incoming LCP light, handedness mismatch leads to no coupling between LCP light and the helix structure, thus gets transmitted as shown in Figure 18c. Following the same logic, for a left-handed helix, the transmitted light will be dominantly RCP. To substantiate this idea, they numerically calculated the current density at f = 75 THz along the helix wire (bottom panel of Figure 18c). For incident RCP, strong coupling leads to large currents at the top end of the helix with little to no transmission, whereas for incident LCP, weak coupling between light and helix structure results in comparably smaller current along the entire helix. Next, they performed the same measurement on the helix structure of both handedness's as shown in Figure 18d. For incoming LCP, the right-handed lower part of the overall structure does not play a role, it transmits to the upper left-handed part. At the top end of the left-handed helix, LCP light undergoes strong coupling and most of the light is therefore reflected. Thus, transmission remains less for incoming LCP. However, for an incoming RCP strong coupling takes place with the bottom right-handed helix, which generates large current that transfers from bottom right- to the top left-handed section of the helix. As a result, the left-handed helix, gets excited and behaves like a helical antenna. Consequently, owing to time-reversal symmetry, the left-handed antenna in the far-field emits LCP, consistent with its handedness. Therefore, the double helix structure converts an incoming RCP to LCP with high efficiency of 75% over a broadband from 50 to 100 THz (Figure 18e). However, for LCP to RCP, the conversion rate remains very low (<10%), over the same frequency regime. Apart from that, Sonsilphong and Wongkasem [170] also demonstrated numerically circular polarisation switching in helical metamaterial.

3.5. Selected Applications of Metamaterials

As discussed in the previous section, metamaterials can arbitrarily manipulate the polarisation state of electromagnetic waves which paves the way to design novel devices for real life applications. Much of the interest in metamaterial devices has stemmed from their potential to overcome fundamental size and bandwidth limitations in conventional optical materials by specific tuning of metamaterial properties, allowing for not only selective manipulation, but also completely novel optical phenomena unseen in natural materials. Engineered metamaterials have advanced research in superlenses, cloaking, holography, while also demonstrating compelling advantages over conventional optical devices [171–173]. The arbitrary wavefront manipulation provided by subwavelength nanostructures affords researchers unparalleled design opportunities for artificial materials, leading to vast and varied approaches to metamaterial devices. Metasurfaces, in particular, have prompted research into the field of flat optics, whereby ultra-thin metadevices provide functionalities previously available only through bulky waveplates and lenses [174]. Functional flat optics would allow for continued miniaturisation of optical systems and devices as well as integration into emerging nanophotonic technologies.

The design flexibility provided by novel metadevices has also allowed researchers to combine multiple optical functionalities into one device, allowing for novel multitasking which would previously require multiple discrete components [175–177]. Very recently, Wang et al. experimentally demonstrated simultaneous beam shaping and focusing using metasurface devices based on silicon nanobricks (Figure 19a) [178]. Careful engineering of the device allowed them to fabricate an optical vortex metalens (OVM) that can produce and focus a vortex beam from incident circularly polarised plane wave. This focusing behaviour is found to vary with the handedness of the polarised light, however, by merging two polarity-inverse OVMs a new device can be created to focus both LCP and RCP light to the same position (Figure 19b–e). Similarly, merging OVMs with different focal points leads to the creation of a new bifocal OVM, allowing the vortex beam to be focused at (Figure 19f) 2 μm and (Figure 19g) 5 μm. Other metadevices allow multiple functions to be performed for light at different wavelengths. Cheng et al. created a multifunctional metasurface based on arrays of plasmonic nanorods (Figure 19h) that demonstrate nearly perfect absorption, linear cross-polarisation and linear-to-circular polarisation conversion for different wavelengths of incident linearly polarised light [179]. For wavelengths ~770nm the device demonstrates absorption (Figure 19i), while at longer wavelengths, the device operates as a polarisation converter, exhibiting linear cross-polarisation at $\lambda = 1227$ nm (Figure 19j) and linear-to-circular polarisation conversion at $\lambda = 1380$ nm (Figure 19k).

Engineered metasurface optics also enable the construction of dynamically tunable and active devices not possible with conventional materials. Many metadevices have been demonstrated to dynamically change their optical properties in response to external stimuli. Thermal, electromagnetic, electromechanical and optical influences have all been shown to dynamically alter metasurface functionalities, allowing for metadevices to be precisely tuned to illicit desired effects, without prefabrication of the device [180]. Microelectromechanical systems (MEMS) fabricated in CMOS compatible materials have been employed as reconfigurable metasurfaces, using the deflection of microcantilever arrays to alter polarisation response.

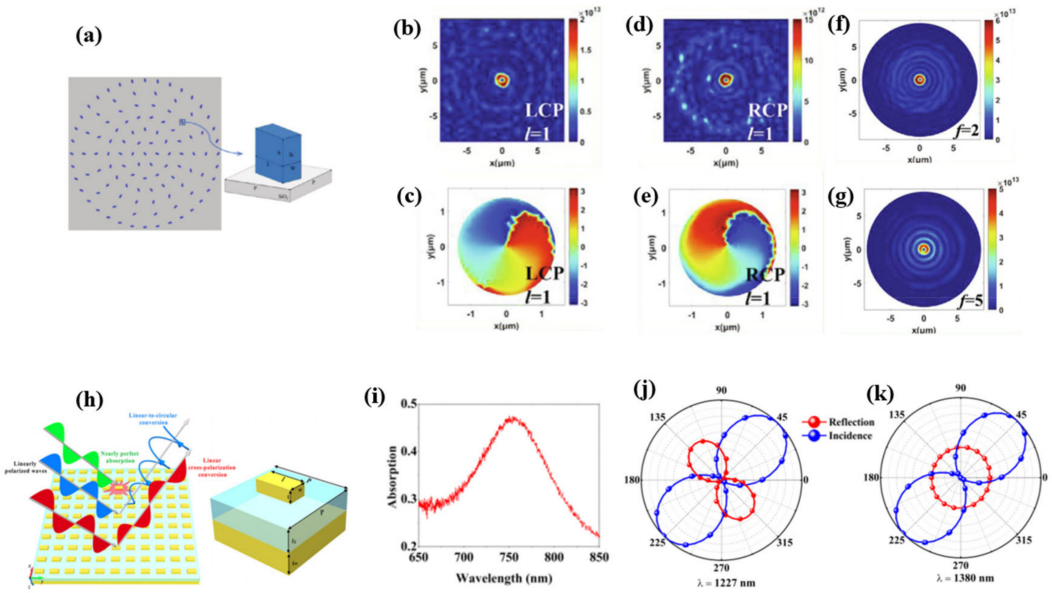

Figure 19. A multifunctional metasurface fabricated from silicon nanobricks functioning as an optical vortex metalens (OVM) allowing for simultaneous beam shaping and focusing ($\lambda = 1500$ nm). (**a**) Schematic of the metasurface and constituent nanobricks. Intensity (**b**,**d**) and phase (**c**,**e**) distributions for left and right circularly polarised light demonstrating the ability to shape and focus light of opposite handedness. Intensity distributions for the bifocal OVM, demonstrating focusing at (**f**) f = 2 μm and (**g**) f = 5 μm. All the figures were reprinted (adapted) with permission from [178], Copyright 2020, Elsevier. (**h**) A multifunctional metasurface consisting of nanorod arrays demonstrating nearly perfect absorption, cross-polarisation and linear-to-circular polarisation conversion for different wavelengths of incident light. (**i**) Measured absorption showing maximum absorption at ~ 770nm. Measured intensity at different polarisations for incident and reflected light illustrating (**j**) cross polarisation and (**k**) linear-to-circular polarisation conversion at $\lambda = 1227$ nm and 1380 nm, respectively. All the figures were reprinted (adapted) with permission from [179], Copyright 2017, American Institute of Physics.

Work by Ma et al. demonstrated structurally reconfigurable metasurfaces based on MEMS resonator arrays to create polarisation sensitive terahertz filters (Figure 20a). Deflection of the curved microcantilevers by an applied electric field allows for dynamic tuning of the device's resonant frequency, leading to tuning of transmitted light for *e*-polarisation while *o*-polarised light remains unaltered. A similar device operating on a thermoelectric principle was demonstrated by Ho et al. [181]. In their device current through the microactuator arrays leads to Joule heating that deflects the microcantilevers, altering the polarisation response at terahertz frequencies (Figure 20b). Further polarisation manipulation and control using MEMS metadevices was demonstrated by Zhao et al. as they realised tunable circular-to-linear polarisation conversion through voltage based microcantilever actuation (Figure 20c) [182]. Novel metadevices have recently been created using other materials and techniques. Nouman and others utilised the insulator to metal transition in vanadium dioxide to create a tunable metasurface device operating at terahertz frequencies. The metasurface is created from wire grating array on VO_2 thin film patches (Figure 20d). Varying the current through the device triggers the insulator to metal transition, altering the resonant frequency of the device for incident polarisations perpendicular to the wire grating and modulating the phase of transmitted light. Parallel polarisations, however, do not experience a current dependent phase shift, allowing phase to be independently varied for orthogonal polarisations. As such, specific tuning of the device enables circular-to-linear polarisation conversion at THz frequencies. A novel liquid metal-based metasurface device was demonstrated by Wu et al. to allow for reconfigurable polarisation response within a microfluidic platform [183]. The device consisted of individually addressable L-shaped microfluidic resonators filled with liquid Galinstan (Figure 20e). The length of both arms in the L-shaped resonators can be varied

by tuning the pressure at both outlets, leading to changes in the polarisation response of orthogonal polarisations. Accordingly, tuning of their device allowed for linear-to-linear, linear-to-circular and linear-to-elliptical polarisation conversions. The versatility provided by engineered metamaterials gives metadevices a unique advantage over conventional optics. Ultrathin metasurfaces continue to demonstrate their utility for wavefront shaping and manipulation, demonstrating functional flat optics in proof of principle devices. Merging, stacking and cascading of separate 2D devices has led to multifunctional metasurface devices, allowing for simultaneous control of multiple optical parameters or specified functions for specified wavelengths. Individually addressable and tunable elements in metadevice arrays lead to tuning of the metadevice, allowing for active metasurfaces to be controlled and reconfigured in a variety of ways. Future devices based on engineered metamaterials will afford users unparalleled versatility in numerous applications through tunable, multifunctional and ultrathin optical wavefront manipulation.

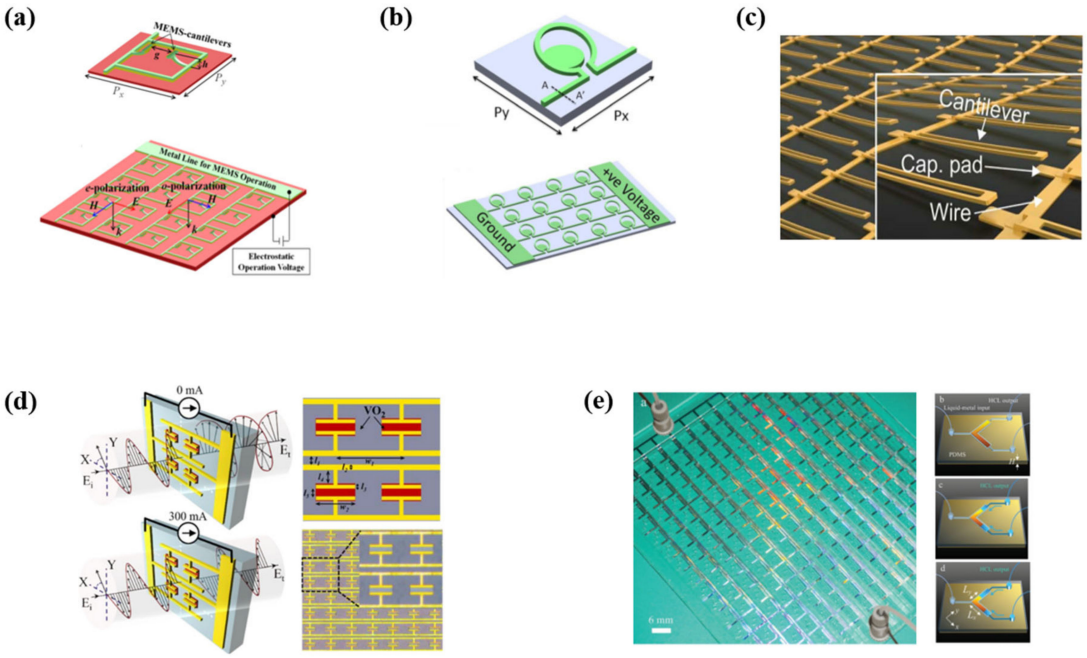

Figure 20. (**a**–**c**) Tuneable MEMS metasurfaces created using CMOS compatible materials operating at terahertz frequencies. Polarisation filter devices achieved through electromechanical (**a**) and electrothermal (**b**) actuation of microcantilever arrays. All the figures were reprinted (adapted) with permission from [181,184], Copyright 2014 and Copyright 2013, American Institute of Physics, respectively. (**c**) Reconfigurable linear-to-circular polarisation conversion whereby voltage based actuation of the microcantilevers allows tuning of the metasurface polarisation response. All the figures were reprinted (adapted) with permission from [182], Copyright 2018, The Optical Society. (**d**) Switchable, voltage-operated quarter wave plate metadevices operating via the insulator to metal transition in Vanadium Dioxide. All the figures were reprinted (adapted) with permission from [185], Copyright 2018, The Optical Society. (**e**) Tuneable polarisation converter metadevice based on a liquid-metal microfluidic platform whereby polarisation response is varied by tuning the length of L-shaped resonator metasurface-elements. All the figures were reprinted (adapted) with permission from [183], Copyright 2017, WILEY-VCH.

4. Polarisation Measurements of Magnetic-Plasmonic Nanostructures

In this third and final section, we will discuss the role of polarisation in magnetic-plasmonic nanostructures. Beginning with a general introduction to magneto-optics and magnetoplasmonics, we will then discuss the role of plasmonics in the Faraday effect, inverse Faraday effect and magneto-optical Kerr effect. Next, we will briefly discuss magnetic plasmon resonances. Then magnetic second-harmonic

generation and magnetic circular dichroism will be reviewed. Finally, several magnetoplasmonics-based applications will be explored.

The study of magneto-optical (MO) effects dates back to 1845 when Michael Faraday discovered that the plane of polarisation of light is rotated when passing through an optically transparent dielectric material under an external magnetic field (Faraday rotation). This effect, later called the Faraday effect, was the first experimental evidence of the connection between light and electromagnetism [186]. The Faraday effect is a result of the left and right circularly polarised (LCP and RCP) light propagating at different speeds through the material (phase difference). Later, John Kerr found that light reflected from a magnetic surface could change intensity and polarisation, which was later named the Kerr effect. In reflection, linearly polarised light was seen to rotate (Kerr rotation) and reflected light can become elliptically polarised (Kerr ellipticity). Microscopically, MO effects require both exchange splitting and spin–orbit interactions [187]. Macroscopically, these MO effects depend on the off-diagonal (antisymmetric) elements of the permittivity tensor associated with the material. Magneto-optic technologies have been applied to microscopy (Kerr microscope) [188], magneto-optic memory devices [189], optical isolators [190], wave modulators [191] and magnetic field sensors [192].

The fields of plasmonics and magnetics merged about 100 years later when Chiu and Quinn discovered that external magnetic fields affect the surface plasmon on metal [193]. Later, with the progression of nanofabrication, complex nanoarchitectures could be developed to further exploit this interaction, bringing forth exciting new physics and applications. In this section, we will discuss magnetoplasmonics, with a special emphasis on a vital component of its measurement—polarisation. The polarisation state of light is integral to magneto-optic measurements, as in MO materials the magnetic field causes optical anisotropy. This optical anisotropy can be quantified by the non-diagonal terms of the permittivity tensor of the material, which leads to variations in the intensity and polarisation state of light.

A plasmon can be used to enhance MO effects, as at the LSPR, diagonal and off-diagonal terms of the permittivity tensor are enhanced. A simple coupled oscillator model has recently been proposed by Floess and Giessen to explain the magnetoplasmonic interaction [194]. Typically, noble metals like silver and gold are selected for plasmonic applications thanks to their low optical losses in the visible and near-infrared spectral range, giving rise to a sharp plasmon peak. These efficient plasmonic materials usually have minimal MO activity, and thus are not suited for MO applications alone. Conversely, some magnetic materials have strong MO effects but cannot sustain a strong plasmon due to optical losses. For this reason, most magnetoplasmonic structures combine a noble metal and a magnetic material, typically a ferromagnetic material, into a hybrid structure. Ferromagnetic materials, unlike paramagnetic materials, possess spontaneous magnetisation resulting from the long-range ordering of unpaired electron spins, and when magnetised, the bulk magnetisation is strong and retained by the material. Most ferromagnetic materials have optical losses too large to sustain a plasmon, except nickel nanoparticles, which have exhibited both localised surface plasmon and ferromagnetism [195].

There are two main reasons to design magnetoplasmonic structures, firstly, to modulate the LSPR response by using external magnetic fields and secondly, to increase the MO effects using the LSPR. These two scenarios, i.e., magnetic field modulation of the LSPR and plasmon-enhanced MOs, are both referred to as magnetoplasmonics; however, the term magnetoplasmonic is also often used to describe systems that combine magnetic and plasmonic materials without the direct study of the magnetic–plasmon interaction [196,197]. By combining MO and plasmonic activity into a single nanostructure, electronic hybridisation between the magnetic and plasmonic material is anticipated, and localisation of the magnetic field near to the plasmonic material takes place [198]. In ferromagnetic materials, the conduction electron spins are spin-polarised, which can affect the free electrons of the plasmonic material (electronic hybridisation). Therefore, the magnetic material must be metallic in nature. Secondly, for magnetic field localisation near the plasmon, the magnetic field of the material must be sufficiently strong and does not necessarily need to interact with the free electrons of the plasmonic material (no hybridisation) and therefore, does not need to be

metallic [198]. Without hybridisation, the LSPR and MO response must be spectrally distinct; otherwise, the magnetoplasmonic response at the plasmon frequency would not be distinguishable from other frequencies [198]. The plasmon-enhancement of the MO effects can be improved by introducing the plasmon-associated enhanced local electric field near to the MO material and/or by changing the reflectivity of the material to maximise the reflected/transmitted optical signal.

4.1. Faraday Effect and Inverse Faraday Effect

Measurement of the Faraday effect is straightforward, linearly polarised light is passed through the sample subject to an external magnetic field (parallel with light propagation) which then passes through an analyser and is detected. In 2005, enhanced Faraday (polarisation) rotation was observed in $CoFe_2O_4$-Ag, dumbbell-like nanoparticles. An enhancement of the Faraday effect was observed for nanoparticles with the plasmonic component (dimer) compared to the $CoFe_2O_4$ monomer [199]. For this experiment, six different laser wavelengths (385, 421, 455, 532, 633 and 850 nm) were used with varying magnetic fields from −1000 to 1000 Oe to collect a Faraday rotation (FR) loop as a function of the magnetic field. Both the $CoFe_2O_4$ nanoparticles with and without Ag exhibited a maximum absorption for the 385 nm laser. Both samples gave a large FR of about 0.75°, but the Ag dimer had a marginally larger rotation. The difference between the samples became more pronounced at longer wavelengths. Beyond 633 nm, the FR for monomer $CoFe_2O_4$changed sign, i.e., instead of positive FR at positive magnetic fields, negative FRs were observed at positive magnetic fields. Such sign reversal was not observed for the plasmonic hybrid nanostructures (see Figure 21a). Plasmon-enhanced FR has also been observed in magnetic-plasmonic, γ-Fe_2O_3-Au, core-shell nanoparticles suspended in solution [200]. Using a tunable laser, an improved spectral resolution was obtained compared to the $CoFe_2O_4$ that used select laser wavelengths. Here, a clear peak in the FR spectrum was observed for the gold-coated γ-Fe_2O_3 at the LSPR (~540 nm), which was not observed in uncoated nanoparticles (Figure 21b). Later, the FR was also found to be dependent on the cobalt core radius with silver shells when the total diameter is fixed [201]. As the LSPR blue-shifted due to higher silver content, the FR maximum also blue-shifted with higher magnitude.

The FR is not limited to nanoparticle form. Chin et al. studied yttrium and bismuth iron garnet films with gold nanowires deposited periodically, maintaining high transparency [202]. Polarisation rotation due to the Faraday effect was enhanced by one order of magnitude owing to the plasmonic structures, with spectral dependency on the period of the nanowires (see Figure 21c). Plasmon-enhanced FR was also observed in Bi:YIG films with a gold nanoparticle coating [203]. The measurements were conducted between 500 and 700 nm, with a plasmon-associated absorption observed at ~630 nm. When the angle of rotation of the light polarisation was studied using an external magnetic field of 5 kOe, a clear peak is observed at the SPR maximum which was not observed in the sample without gold coating. Floess et al. observed a tunable and switchable polarisation rotation in gold nanowire coated EuSe thin films [204]. In these structures, the period and the width of the gold nanowires allowed wavelength selectivity; and rotations up to 8.4° were observed. Recently, Kuzmichev et al. studied Bi-substituted iron garnet films with gold nanodisks at different depths [205]. They found that the Faraday effect was most enhanced by the gold nanodisk plasmon when submerged near the upper surface of the magnetic film (see Figure 21d). This finding may aid the future design of plasmon-enhanced FR materials.

Along with noble metal plasmons, single and multilayer graphene deposited on SiC substrate demonstrated large FR, as a result of either the cyclotron effect or inter-Landau-level transitions [206]. Large magnetic fields of 7 T were used to achieve FR of ~6° within 2–4 THz range. Later, Tymchenko et al. calculated large FR in graphene microribbon arrays at higher frequencies (>10 THz) and with smaller magnetic fields than in continuous graphene sheets [207], thus opening up new possibilities in ultrathin tunable MO devices.

Magnetisation can also be induced in purely metallic structures through illumination with circularly polarised light; this is called the inverse Faraday effect. This measurement is typically

conducted using time-resolved pump-probe, with the pump beam circularly polarised and the probe beam linearly polarised. The scheme is similar to standard Faraday effect measurements, but with the absence of an external magnetic field and the filtering out of the pump beam. First observed in $DyFeO_3$ [208], inverse Faraday effect was seen in various films [209,210]. Recently, the inverse Faraday effect was observed in gold nanoparticles in solution [211].

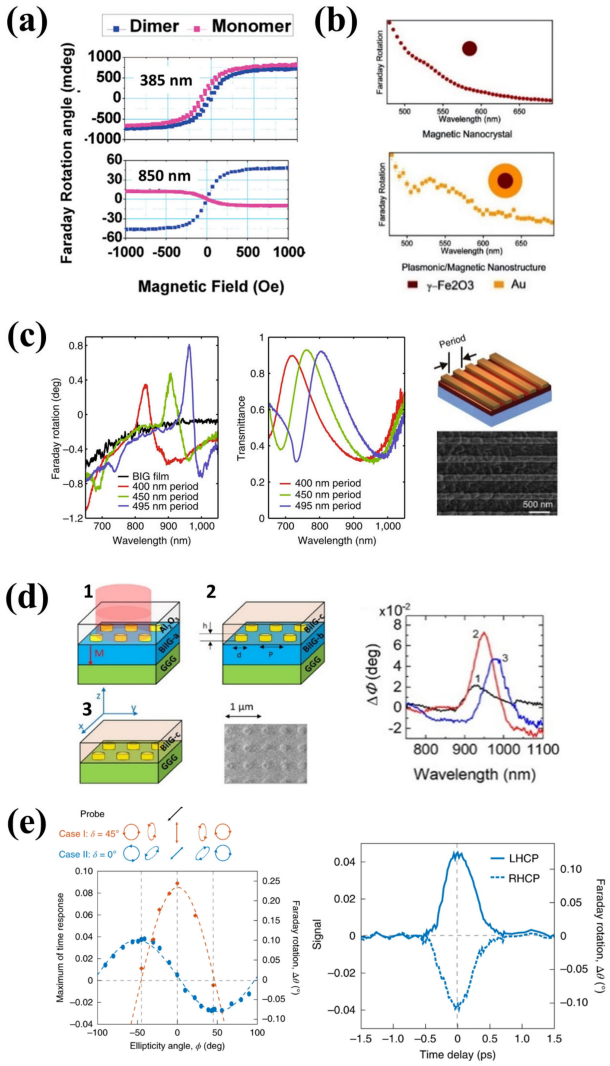

Figure 21. (**a**) FR of $CoFe_2O_4$ nanoparticles (monomer, pink) and $CoFe_2O_4$-Ag nanoparticles (dimer, blue) at 385 (top) and 850 nm (bottom), showing a reversal in the magnetisation loop only for the monomer nanoparticles at long wavelengths. Adapted with permission from [199], Copyright 2005, American Chemical Society. (**b**) FR of iron oxide nanoparticles (top) enhanced by gold coating (bottom), with a peak corresponding to the LSPR of the nanoparticle. Adapted with permission from [200], Copyright 2009, American Chemical Society. (**c**) FR and transmittance dependency on gold nanowire period atop a magnetic film. Adapted with permission from [202], Copyright 2013, Springer Nature. (**d**) Plasmon-enhanced FR of samples (1–3) with different depths of gold nanodisks in films, with sample 2 where nanodisks are submerged inside the magnetic film achieving the highest rotation. Adapted with permission from [205], Copyright 2020, Wiley-VCH. (**e**) Inverse Faraday effect in gold nanoparticles measured using a pump-probe setup. Left, FR for different ellipticity angles (ϕ) of the pump, for two different polarisation angles between the pump beam and probe (δ), with a maximum for $\delta = 45°$ at linear polarisation (Kerr effect) and at $\delta = 0°$ for circular polarisation ($\phi = 45°$) (inverse Faraday effect). Right, time response of Faraday rotation, showing picosecond regime magnetisation and demagnetisation. Adapted with permission from [211], Copyright 2020, Springer Nature.

In this work, a pump-probe setup was used. The linearly polarised probe beam was passed through the sample and detected with an analyser, while the pump beam was circularly polarised to induce the inverse Faraday effect. The ellipticity angle (ϕ), handedness and polarisation angle between the pump beam and probe (δ) were varied to confirm the inverse Faraday effect (see Figure 21e). Where $\delta = 0°$, increased pump ellipticity led to increased FR, with maximums for pure LCP and RCP light; while for $\delta = 45°$, the maximum rotation was observed for linear polarisation (arising from the Kerr effect). Furthermore, the time-response indicated the mechanism was related to the coherent circular motion of the electrons in the gold nanoparticles as opposed to the spin dynamics as seen in ferromagnetic materials, shown in the right panel of Figure 21e.

4.2. Magneto-Optic Kerr Effect

There are three types of magneto-optic Kerr effect (MOKE) measurement techniques, which are classified by the sample's magnetisation vector direction with respect to the sample surface and the incident light [188]. Polar MOKE (PMOKE) denotes the measurement where magnetisation vector is orthogonal to the surface and parallel to the incident light plane, longitudinal MOKE (LMOKE) corresponds to a magnetisation vector in parallel with the surface and incident light plane and lastly, the transverse MOKE (TMOKE) involves the magnetisation vector orthogonal to the light plane and parallel to the surface [188]. All three types of MOKE measurements have been employed in magneto-plasmonic measurement. P/LMOKE are used to study the effects of the plasmon on the reflected light polarisation, while TMOKE involves a plasmon-enhancement of the reflected light intensity.

Plasmonic nickel nanoferromagnet discs have shown plasmon-controlled Kerr rotation, in LMOKE configuration [212]. Three differently sized nanodisks with distinct LSPR responses were studied with two excitation lasers (405 and 670 nm), with MOKE rotation exhibiting contrasting characteristics for the differently sized discs. For the smallest disc diameter, the magnetisation loop shows a maximum MOKE rotation for negative magnetic fields for both wavelengths, while the largest disc shows a maximum MOKE rotation for positive magnetic fields for both wavelengths. Conversely, for the intermediate disc size, the MOKE magnetisation loop shows an excitation wavelength-dependent sign change (see Figure 22a). Considering nickel-based magnetoplasmonics avoid the complex chemistry and fabrication techniques often required for hybrid plasmonic-ferromagnetic structures, this observation opened up a more straightforward method to study and apply plasmon-enhanced MO.

Surface plasmons have been shown to enhance the PMOKE effect in Au/Co/Au multilayer films [213], then later in Au/Co/Au nanodisks [214]. The optical and MO properties of the latter could be tuned by varying the nanoparticle disk size and shape. Recently, asymmetric geometry magnetoplasmonic nanocavities were designed which support multipolar dark plasmons [215]. In this work, gold nanoring arrays had a permalloy nanoparticle disc added inside, either in the centre to create the symmetric nanocavity (CRD) or off centre, forming the asymmetric cavity (NCRD) (see Figure 22b). The authors showed unprecedented MO enhancement in the broken symmetry structure, facilitating effective control of light polarisation using weak magnetic fields. This enhancement was explained by dark multipolar Fano resonance modes (at ~820 nm, see Figure 22b middle and bottom panel) in the ring nanostructure hybridising and enhancing the magnetic-field-induced radiant dipole of the permalloy, measured using PMOKE configuration.

Kreilkamp et al. reported 1.5% modulation of transmitted light intensity, using plasmonic gold nanowire enhanced TMOKE while maintaining transparency of ~45% [216]. The 1.5% modulation occurred when the localised plasmon hybridised with the propagating waveguide mode of the nanowire. By reducing the period of the nanowires, the resonance seen in the transmission and TMOKE spectra could be blue-shifted, with a gradual reduction in the TMOKE signal (see Figure 22c). MO activity was also detected in gold nanoparticles sputtered on glass in TMOKE configuration, which was also applied to SPR refractive index sensing [217]. Rizal et al. recently compared the efficiency of Ti/Au/Co/Au against Ti/Ag/Co/Au by using two plasmonic sensing schemes (TMOKE vs.

SPR) [218] (see Figure 22d). Both of the samples showed TMOKE enhancement over the SPR, while the Ag-based one gave overall higher TMOKE and SPR activity. They found that the TMOKE sensor had a Q-factor more than twice that of the SPR sensor, and suggested this enhanced sensitivity could be used to detect lower analyte concentrations.

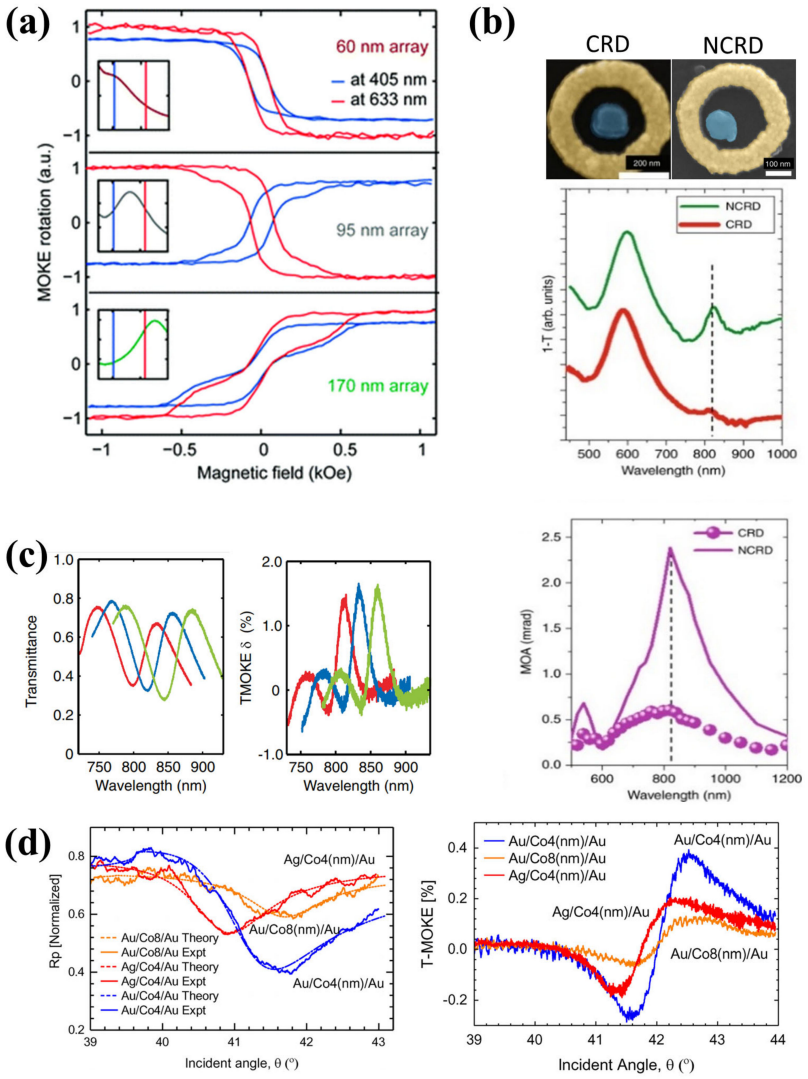

Figure 22. (**a**) LMOKE rotation studies of nickel nanodisks with varying diameters (60, 95 and 170 nm) at 405 and 633 nm, with insets of the extinction spectrum of the nanodisks arrays. A clear wavelength-dependent MOKE magnetisation loop reversal can be seen for the 95 nm array. Adapted with permission from [212], Copyright 2011, American Chemical Society. (**b**) Scanning electron microscopy images of magnetoplasmonic concentric ring disks (CRD) and non-concentric ring disk (NCRD) composed of a gold ring and $Fe_{20}Ni_{80}$ enclosed disk, the transmittance spectra are shown below in the middle panel. The green transmittance spectra correspond to NCRD which has a second peak that can be observed at 820 nm. MO activity (measured by PMOKE) of the nanocavities is shown in the bottom panel, with a large enhancement at 820 nm in the asymmetric cavity. Adapted from [215], CC BY 3.0 2020, Springer Nature. (**c**) Transmittance and TMOKE of iron garnet films with gold nanowires deposited atop with varying period, 450 nm (red), 475 nm (blue), and 500-nm period (green). The TMOKE peak can be seen to redshift with increased period. Adapted from [216], CC BY 2013, American Physical Society. (**d**) P-polarisation reflectivity and TMOKE profiles for Au/Co/Au or Ag/Co/Au samples, used to find the quality factor of the different sensing schemes. Adapted with permission from [218], Copyright 2020, IOP Publishing.

4.3. Magnetic Plasmon Resonances

At optical frequencies, the magnetic permeability of most materials is small and, therefore, the magnetic interaction is typically less than electric interaction, likewise; magnetic plasmon resonances at optical frequencies are more challenging to achieve in natural materials. Pendry et al. [219] demonstrated resonance of the magnetic plasmon incident on double split-ring resonator structures, tuning the effective magnetic permeability of nonmagnetic material to negative values. Furthermore, the permeability could be tuned by changing the geometry of the nanostructure, but the resonance was limited to the microwave region. These split ring structures were modelled as a LC circuit, with a capacitance (C) and inductance (L). In this model, the ring structure can be considered a coil winding, while the branches of the horseshoe are capacitor plates. By scaling down the dimensions of the nanostructure, the inductance and capacitance of the structure also scale down. As the resonant frequency of an LC circuit is inversely proportional to the product of the inductance and capacitance, scaling down the structure was assumed to lead to an increased resonance frequency. Klein et al. [220] demonstrated a breakdown of this rule, achieving a magnetic plasmon resonance in more compact horseshoe split rings at 900 nm. The authors attribute this to the metal deviating from "ideal" metal explained by the Drude model (LC resonance frequency << plasma frequency of the metal), and instead the complex dielectric function of the metal was needed to support the experimental results theoretically. Horizontal light polarisation at normal incidence may be used to excite the magnetic resonance by the electric field component by inducing a circulating circuit in the structure, provided it is perpendicular to the branches of the horseshoe-like, split ring structure. For vertical polarisation at normal incidence, neither the electric nor magnetic field can excite the LC resonance. However, both linear polarisations may excite the electric resonance of the structure, and so the different polarisation schemes can be used to identify the magnetic and electric plasmon resonances.

Bao et al. [221] studied gold split ring hexamer nanostructures using scattering spectroscopy, showing magnetic and electric plasmon modes appearing depending on the illumination polarisation, shown in Figure 23a. Two electrical dipolar modes were observed at 650 and 775 nm. The magnetic dipole mode was observed at 900 nm, which results from the x-component of the electric field and could only be detected using azimuthally polarised light. This magnetic mode was most prominent for 0° (parallel to split) and decreased in magnitude with increased angle of incidence. These experimental findings were supported by finite-difference time-domain (FDTD) simulations, supporting the authors' experimental determination of the magnetic and electric resonances by polarisation resolved scattering spectroscopy. Furthermore, these split-ring hexamer structures were then assembled into 6-piece and 12-piece ring structures that exhibited narrowband single and double Fano resonance, respectively. The narrow FWHM of these Fano resonances is noteworthy for lineshape engineering applications.

Kuznetsov et al. partially cut gold and silver nanoparticles into split-ball resonator structures shown in the top panel of Figure 23b [222]. These split-ball resonators are similar to upright split-ring resonators, but these structures facilitate coupling of the incident light to the magnetic resonance mode yielding higher efficiency owing to a combined electric and magnetic field contribution (LC mode). These split balls were capable of sustaining a magnetic plasmon at 600 nm in gold and 565 nm in silver. To study the electric and magnetic plasmons, s- and p-polarised light was used. P-polarised light was expected to couple with the electric dipole resonance, whereas the s-polarisation excited both the electric and magnetic dipole (LC) (see Figure 23b). Simulations showed that the deeper the depth of the cut in the nanosphere, the more blue-shifted the LC resonance while increasing the width of the cut led to a red-shifting of the LC resonance.

DNA-origami-based strategies have been used by Wang et al. to assemble gold nanoparticles into hexagon rings and then combining these rings into more complex nanoarchitectures, which were subsequently coated with silver [223], as depicted in the left panel of Figure 23c. In the single DNA origami ring composed of six nanoparticles, the peak at ~520 nm is the electric dipole whereas the smaller peak at ~570 nm is attributed to the magnetic dipole, which could be isolated by using a cross-analyser. Combining these rings into more complex structures, yielded scattering spectra with

multiple modes, and magnetic SPPs could be supported in ring chain-like structures. For further details about magnetic plasmons, a comprehensive review on optical magnetism was carried out by Monticone and Alù [224] and by Calandrini et al. on magnetic hot-spots [225].

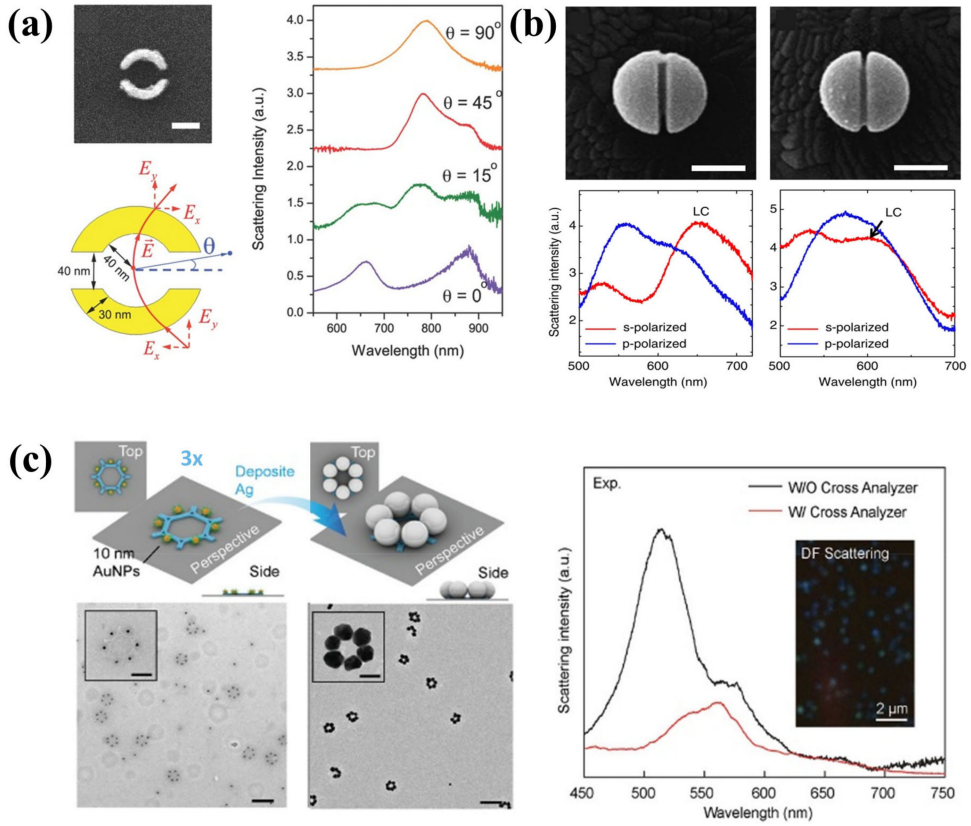

Figure 23. (**a**) Split ring nanostructure image and geometry, right, scattering spectra of nanorings with differing angles of incidence. At 0°, two resonances are observed 650 (electric) and 870 nm (magnetic), then at 15° a third mode at 750 nm (electric) appears and becomes prominent for the larger angles. Adapted with permission from [221], Copyright 2015, Wiley-VCH. (**b**) Electron microscopy image of split ball resonators, gold nanoparticles with a cut width of 15 nm, with different depths (where left is deeper). Below, their respective scattering spectra where s-polarisation light polarisation perpendicular to the cut and p-polarisation is parallel. The marked LC resonance is the combined electric and magnetic resonance, while the p-polarised peak is attributed to electric resonance. Adapted with permission from [222], Copyright 2014, Springer Nature. (**c**) Simplified construction of gold nanoparticles assembled using DNA origami, which are subsequently coated with silver, scattering spectra of the nanostructure, with the electric (520 nm) and magnetic dipolar contributions (570 nm). Adapted with permission from [223], Copyright 2019, Wiley-VCH.

4.4. Second-Harmonic Generation (SHG)

Second-harmonic generation (SHG) is a nonlinear optical phenomenon where two photons of coherent light with the same frequency interact with a material and combine to generate a new photon that has twice the frequency of the incident photons. SHG is sensitive to breaks in the spatial or temporal inversion symmetry of material, and so has been applied to study magnetics (MSHG) by adding the application of an external magnetic field. MSHG has better sensitivity to interfaces than linear MOKE, owing to the increased sensitivity to breaks in symmetry. In the simplest form, SHG setups consist of a fundamental laser focused onto the sample that generates the SHG signal, the fundamental signal is filtered out and the SHG signal is sent to the detector, in either reflection or transmission.

Purely plasmonic nanostructures have demonstrated plasmon-enhanced (non-magnetic) SHG [226] and third harmonic generation, (non-magnetic) THG [227]. Similarly, magnetic-dipole plasmons have been shown to enhance (non-magnetic) SHG activity in metal−dielectric−metal disk nanoparticles [228] and colloidal gold nanocups [229]. Silicon nanodiscs that exhibit both electric and magnetic dipolar resonances were shown to have enhanced third-harmonic generation near the magnetic dipolar resonance [230].

Nickel nanorods have exhibited plasmon-enhanced MOKE, both linear and nonlinear (MSHG) [231]. The geometric anisotropy of the nanorods led to differing contributions to the second-order susceptibility tensor that has magnetisation and crystallographic dependent components. Linear measurements (TMOKE) were performed using p-polarised light at an incident angle of 68° and was varied between 300 and 850 nm. The TMOKE spectrum exhibits a peak at 380 nm, corresponding to the transverse plasmon of the nanorods. A second peak emerged at 600 nm in the TMOKE spectrum, which was also seen as a minimum in the reflectivity spectra, and therefore was attributed to the Fabry–Perot resonance mode of the material. Magnetic and nonmagnetic SHG measurements were conducted using s- and p-polarised light at various angles of incidence. Nonmagnetic SHG showed no resonant features, while its magnetic counterpart showed a maximum at 760 nm (twice the fundamental wavelength) for the s-polarised pump beam, but was not observed in the p-polarised pump beam spectra and thus, is not an effect of interference (see Figure 24a). The 100 nm gold nanoparticle arrays covered with a 90 nm thick layer of iron garnet exhibited MSHG which could be spectrally shifted (by up to 5 nm) by changing the magnetic field direction [232] (see Figure 24b). This spectral shift is not attributed to shifting of the LSPR, but rather due to interference of resonant and nonresonant MSHG signals of both crystallographic and magnetic origin.

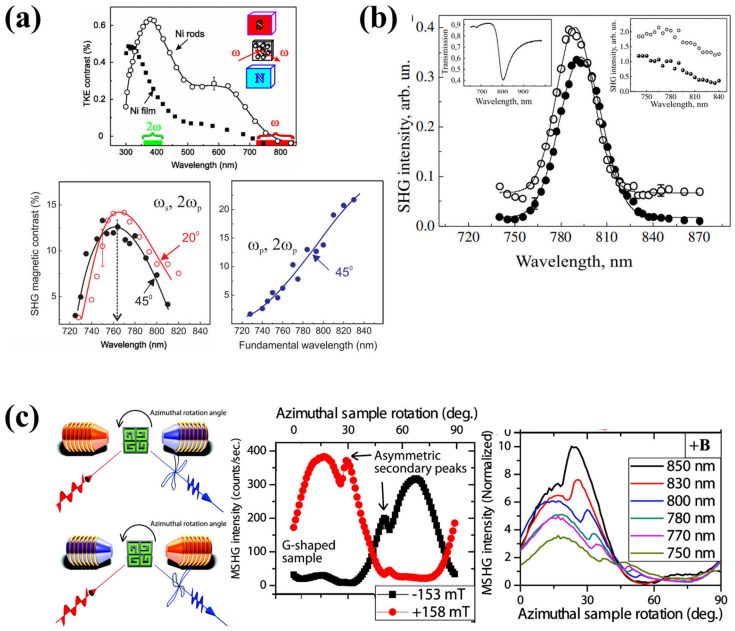

Figure 24. (**a**) MOKE spectrum obtained for nickel nanorod (open circles) vs. film material (filled squares) with fundamental and doubled frequency marked. Below left, MSHG magnetic contrast spectrum of the nickel nanorod is given for two angles of incidence of s-polarised light, a maximum is observed for 760 nm, where the SHG emission matches the LSPR maximum of 380 nm. Below right, the same for p-polarised light with an absence of peak. Adapted with permission from [231], Copyright 2013, American Physical Society. (**b**) MSHG spectra for gold nanoparticle array coated by an iron garnet

layer with an applied magnetic field of varied sign (positive open circle, negative filled circle), showing a spectral shift. Insets show the transmission spectra and MSHG for a non-plasmonic film. Adapted with permission from [232], Copyright 2016, The Optical Society. (**c**) MSHG of G-shaped nickel nanostructures to determine magnetisation direction, where the sample is rotated azimuthally in different magnetic field directions. The four-fold polarisation profile is asymmetric (secondary peaks) and resembles a ratchet wheel. Middle, MSHG intensity as a function of rotation angle for two magnetic fields, a clear asymmetry can be seen. Right, the MSHG for different wavelengths, with longer wavelengths yielding high MSHG intensity. Adapted with permission from [233], Copyright 2011, American Chemical Society.

Valev et al. used the plasmon contributions to the MSHG to find the magnetisation direction in G-shaped Ni nanostructures [233]. Here, the surface plasmons could create asymmetries in the rotational dependant MSHG response, similar to a ratchet wheel, so that directionality could be inferred (see Figure 24c). In this work, the magnetic field is in the plane of optical incidence, with the polariser and analyser along the vertical direction. In this configuration, a single odd element of the effective nonlinear susceptibility tensor contributes to the signal. Asymmetric peaks and magnetic field direction dependence can be seen in the MSHG intensity as a function of azimuthal sample rotation. Furthermore, the position of the secondary peak depends on the wavelength. The asymmetric MSHG response is therefore attributed to the plasmon, where incident light selectively couples to the plasmon modes of the nanostructure at certain sample rotation angles.

4.5. Magnetic Circular Dichroism

Magnetic circular dichroism (MCD), an extension of circular dichroism (CD), is a technique where the difference between a sample's absorption of right and left circularly polarised light is measured in the presence of an external magnetic field. MCD has been used to study circularly propagating magnetoplasmonic modes in symmetric gold nanospheres, where MCD signal is a derivative-like, bisignated curve with the x-axis crossover point aligning spectrally with the LSPR [234] (see Figure 25a).

The MCD bisignated curve is a result of the differing response of the electrons in the nanoparticle to the incoming LCP and RCP light, with the polarisations shifted in energy per the right panel in Figure 25a. Thanks to the sensitivity of the LSPR to the refractive index of the surrounding medium and the strong dependency of the MCD signal on this LSPR, MCD measurements utilising plasmonic nanoparticles have good potential in refractometric sensing. MCD was also used to monitor the linking of silver-coated gold nanorods to supramolecular J-aggregates [235]. When the J-band exciton and plasmons coupled at resonance, enhancements were observed in the MCD signal. This finding opened up the possibility of magnetic-based chemo- and biosensing.

Shiratsu and Yao demonstrated that the bisignated MCD dipolar response of Ag nanocubes depends strongly on the nanocube edge length, with the zero crossover point in the MCD spectra corresponding to the LSPR maximum [236]. Furthermore, the smallest nanocube exhibited the highest MCD as shown in Figure 25b, and this size dependency arises from spectral inhomogeneity in the LSPR extinction. In stark contrast, MCD signal attributed to higher-order multipolar LSPR modes did not correspond to the optical extinction spectra and was size-independent, which the authors hypothesised was as a result of an unequal response to the RCP and LCP light under the magnetic field.

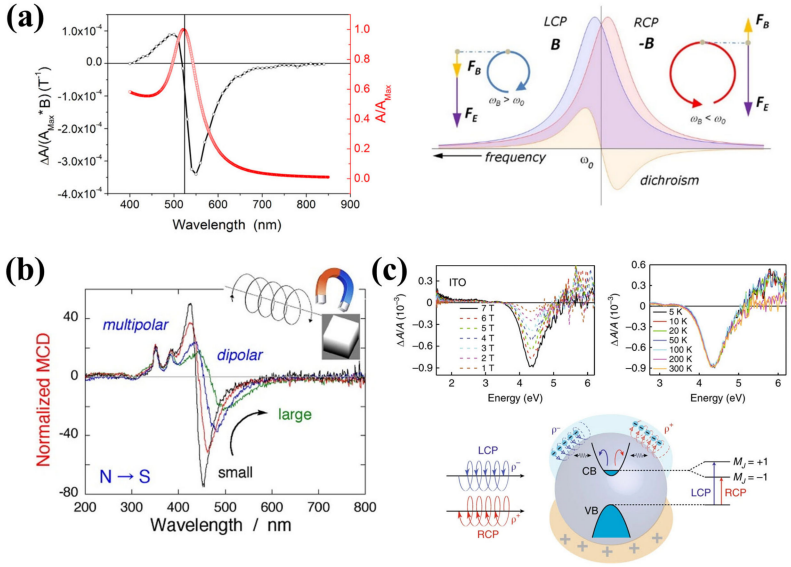

Figure 25. (**a**) Left, MCD/absorbance spectrum of gold nanoparticles, with MCD y-crossover at the LSPR wavelength. Right, schematic showing the differing response for RCP and LCP light, due to different electric (F_E) and magnetic (F_B) contributions of the Lorentz force on the electrons. Adapted with permission from [234], Copyright 2013, American Chemical Society. (**b**) MCD spectra for silver nanocubes of varied size, exhibiting dipolar and higher-order multipolar resonances. MDC dipolar response decreases with increased size, but multipolar effects are less size-dependent. Adapted with permission from [236], Copyright 2018, Elsevier. (**c**) Electron polarisation scheme for Doped-ITO nanoparticles. Top left, MCD spectrum at different field strengths is given in dashed coloured lines. Right, the temperature dependency of the MCD signal. Lastly the schematic of the conduction band splitting due to the angular momentum of the magnetoplasmonic modes due to RCP and LCP excitation. Adapted with permission from [237], Copyright 2018, Springer Nature.

Yin et al. used MCD to study the excitonic properties of degenerately doped (Sn/Mo) In_2O_3 nanocrystals [237]. The measured MCD signal for the ITO nanocrystals was temperature-independent and linearly dependent on the magnetic field (see Figure 25c), and thus specific to the cyclotron motion of the nanocrystals free electrons (magnetoplasmon) leading to splitting of the electronic band state, as opposed to interband sublevels, because the electrons are spin polarised. This result was noteworthy as the spin polarisation coupling is non-resonant; with magnetoplasmons resonant in the near-infrared, whereas the excitons at the bandgap are resonant in the ultraviolet. Furthermore, the charge carrier polarisation could be controlled in the IMO nanocrystals by varying the doping level and magnetic field strength, thus, the magnetoplasmonic mode could be harnessed as a new degree of freedom. This finding opens up a new field, plasmontronics, involving intrinsic plasmon-exciton and plasmon-spin interaction phenomena.

Spin-polarisation transfer from iron oxide to gold has been observed using X-ray magnetic circular dichroism (XMCD) [238]. A magnetic moment arose in the 5d band of gold-iron oxide, core-shell nanoparticles observed at the gold L edge in the XMCD spectrum. The phase of the iron oxide was demonstrated to be crucial for spin polarisation transfer.

4.6. Applications of Magneto-Plasmonics

In this final section, we will explore selected applications of magnetoplasmonic materials, in particular sensing and nanophotonic devices. SPR sensors (e.g., Biacore) are a common biosensing tool used to measure biomolecular interaction. These sensors detect variation in the refractive index at the sensor surface using total internal reflection of plane polarised light incident on a liquid–metal film interface. At the opposite side of the metal face, the photon-induced plasmon propagates

which is sensitive to the refractive index that varies with analyte binding. Combining SPR and MO technology into MOSPR devices, an enhancement of p-polarised light can be achieved due to MO Kerr enhancements. Sepúlveda et al. [239] and Rizal et al. [240] showed an improvement of MOSPR biosensor technology over SPR sensor by a factor of 3–4. Figure 26a demonstrates the superiority of MOSPR sensitivity (compared to conventional SPR) to isopropanol vapours at different concentrations [241].

Magnetoplasmonics have also been applied to measure nanoscale distances [242]. The distance between nickel nanodiscs was measured using Kerr polarisation rotation, with a precision ~2 orders of magnitude higher than state-of-the-art plasmon rulers. Moreover, the system allowed intrinsic spatial orientation adoptability for optimising the nanogap measurement orientation. Figure 26b shows the effect of the spatial orientation of the ruler with respect to the electric and magnetic field direction (90°, 45° and 0°) on the Kerr rotation angle in the 625–635 nm spectral region. When the electric and magnetic fields are 90° to the ruler (p-short) a figure-of-merit (FOM, the ratio between sensitivity and the width of the resonance peak) of 1.5 was achieved. For the electric and magnetic fields at 45° (p-45) a FOM of 1 was attained. When the electric and magnetic fields were aligned parallel with the ruler, the best separation in the Kerr rotation angle for the different ruled distances was achieved with a FOM of 26.7. Considering a standard plasmon ruler could reach a FOM of 0.67, all magnetoplasmonic ruler orientations were superior.

Iron oxide nanorods coated in silica and gold, have been designed by Wang et al. [243] that can be oriented using an external magnetic field, which in turn elicits a varied optical polarisation response. Furthermore, a device was created based on the hybrid nanorods, capable of sensing the magnetic field orientation based on the optical response.

Along with sensing, magnetoplasmonics can also be utilised in photonic applications. Pancaldi et al. fabricated arrays of elliptical Au-Py-Au layered nanoparticles on glass to study the plasmonic photo-heating of nanomagnets using specific light polarisations for selective element heating [244]. Figure 26c shows the extinction spectrum (1-T) using light polarisation along the major/minor axis of the elliptical nanoparticles and the spectral position of the pump and probe. This pump beam was used to measure LMOKE hysteresis loops using polarisation along the long axis of the nanoparticle. A higher power pump led to a decreased coercive field and increased photo-heating, with the magnitude depending on the aspect ratio of the particular nano-ellipse. This finding supports thermally triggered magnetisation reversal in single nanostructures. This technology has interesting applications for selective thermalisation in say, multisystem chips.

Belotelov et al. reported light intensity modulation of 24% by varying the transparency of a magneto-plasmonic crystal [245]. By using in-plane magnetic fields to excite a perpendicularly polarised waveguide mode to vary the transmission spectrum of a magneto-plasmonic crystal [245]. The authors theorise that the effect could exceed 100% using higher quality material. Zubritskaya et al. reported a magneto-chiral trimer nanoantenna surface that consisted of gold and nickel nanodisks. The structure could tune the chiroptical transmission up to 150% using an external magnetic field perpendicular to the nanoantennas plane [246] as depicted in Figure 26d.

Under an applied magnetic field, magnetic nanoparticles can assemble into 1D chains due to magnetic dipolar interaction forces. Song et al. utilise this phenomenon by assembling iron oxide coated silver nanoparticles into long chain-like structures for eventual applications in optical filtering [247]. By varying the polarisation of light, the longitudinal and transverse LSPR can be tuned from visible to near-infrared wavelength regime (see Figure 26e). The redshift of the longitudinal LSPR is caused by near field coupling of neighbouring plasmonic NPs, whereas a blueshift of the transverse LSPR arises from far-field coupling. A summary of the polarisation-based applications of magnetic-plasmonic materials is shown in Table 1.

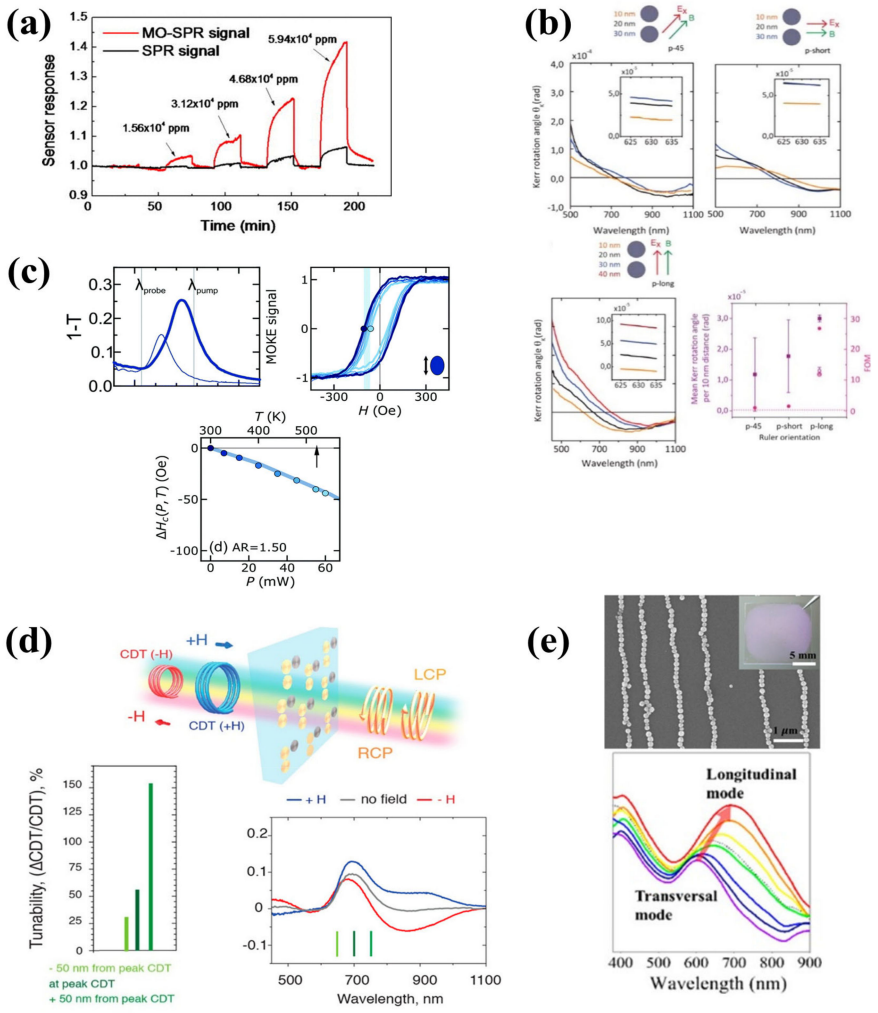

Figure 26. (**a**) Signal response of SPR and MOSPR to isopropanol vapours of different concentrations, with MOSPR showing a clear superiority. Adapted with permission from [241], Copyright 2012, American Institute of Physics. (**b**) Magnetoplasmonic ruler based on nickel nanodiscs, the distance between the nanodiscs can be calculated from the Kerr rotation angle. The Kerr rotations for electric and magnetic field directions (with respect to ruler orientation) are shown, with the parallel fields yielding superior rotations. Bottom right compares figure-of-merit and error bars for the various orientations compared to standard plasmonic rulers (dashed line). Adapted with permission from [242], Copyright 2015, American Chemical Society. (**c**) Left, Extinction spectrum of tri-layer Au–Py–Au elliptical nanostructure along the long axis (thick line) and short-axis (thin line), with pump and probe wavelengths marked. Right, thermoplasmonic heating effects on the magnetic properties obtained by LMOKE, with increased power leading to a decreased coercive field (light blue lines), below, the power-dependent decrease in the coercive field against the calculated temperature increase. Adapted with permission from [244], Copyright 2019, Royal Society of Chemistry. (**d**) Shows the scheme of Au–Au–Ni trimer nanoantennas arrays to study chiral differential transmission (CDT) under magnetic field application. Below left, the tunability of up to 150% for a specific geometry shown in CDT spectrum to the right with a varied external magnetic field. Adapted with permission from [246], Copyright 2018, American Chemical Society. (**e**) Assembled silver-magnetite nanoparticles electron microscopy image and photograph inset, where the LSPR extinction peak varies with the change in the polarisation angle. Adapted with permission from [247], Copyright 2017, American Chemical Society.

Table 1. Overview of the polarisation dependent applications of magnetic, plasmonic materials.

Material	Mechanism	Possible Application	References
Plasmonic nanowire on magnetic film	Faraday effect	Tunable and switchable polarisation rotation for optical isolators	[202,204]
Gold nanoparticles in solution	Inverse Faraday effect	Optical isolation without external magnetic fields	[211]
Plasmonic—magnetic film	Kerr effect	Magneto-optical surface plasmon resonance	[218,239]
Nickel nanodiscs	Kerr effect	Active ruler utilising polarisation, monitoring polarisation-selective photo-heating	[242,244]
Plasmonic resonator structures	Magnetic plasmon resonance	Surface-enhanced Raman scattering, nanoantennas	[221,222]
G-shaped nickel nanostructures	Magnetic second-harmonic generation	Probing the magnetisation direction	[233]
Plasmonic nanoparticles	Magnetic circular dichroism	Sensing by monitoring the intensity of circularly polarised light	[235]
Assembled chains of magnetic-plasmonic nanoparticles	Dipole–dipole magnetic interaction	Optical filtering	[247]

5. Conclusions and Perspectives

In this review, we covered three important aspects of polarisation response from plasmonic nanostructures. In the first section, we discussed the tailoring between LSPR scattering and symmetry of various plasmonic nanostructures with potential applications in optics and optoelectronics. Numerous techniques including SERS scattering, DF extinction and IR transmission/absorption have been employed to investigate the polarisation response, starting from the simplest nanostructure of single nanoparticle to complicated nanoprisms or nanocrescents. In general, all such measurements allow to identify the symmetry of the plasmon modes and distinguish differently shaped particles in a nanoparticle cluster. Moving forward, the strong optical anisotropy and polarisation response obtained from differently shaped plasmonic nanostructures intrigued much interest to exploit such effects SPR sensing. Most of the established SPR sensing relies on the dip or shift in reflected intensity (amplitude) profile at certain wavelength or incident angle. However, we believe that polarisation sensitive selective excitation and detection of particular plasmonic mode and measuring phase shift between them opens up more contrasting sensing opportunities which is yet to be explored. In the second section, we discussed how the artificially fabricated new generation metamaterials can manipulate the polarisation state of light in different ways, e.g., linear polarisation rotation to its cross polarisation, linear-to-circular (or vice versa) polarisation or handedness change for circular polarisation. It is always desirable to achieve all the functionalities within a single metamaterial structure. Although, Liu and co-workers inverse designed chiral metamaterials with multifunctional polarisation manipulation ability, it operates in the GHz regime and remains a real challenge to facilitate such structures to operate in the high frequency THz regime which have more potential applications in ultrafast photonics and optomagnetism. In the last section, we discussed the newly emerged field of magneto-plasmonics with particular emphasis on polarisation in magnetic-plasmonic nanoparticles and thin film structures. These nanostructures either consist of a magnetic material which can sustain a plasmon (e.g., nickel) or, more commonly, consist of hybridisation of a magnetic and plasmonic material (e.g., iron + gold). Various topics including Faraday and inverse Faraday effect, MOKE, magnetic plasmon resonance, magnetic second harmonic generation and magnetic circular dichroism are discussed, along with many potential applications. Magnetoplasmonics is a constantly evolving field, with new sub-fields such as plasmontronics emerging and nanofabrication advancing, it is safe to assume that many more interesting developments are on the horizon and it is likely that polarisation will be pivotal

to the measurement. Subsequently, many applications will emerge, particularly in sensing and nanophotonic devices.

Author Contributions: P.K., G.B. and J.L. wrote the paper. P.K., G.B. and J.L. edited the draft. P.K., G.B., J.L., S.A.M.T., N.L. and C.S. All authors have read and agreed to the published version of the manuscript.

Funding: This work was supported by Irish Research Council (GOIPD/2018/716), Science Foundation Ireland (SFI) centre CÚRAM, the European Regional Development Fund (Grant Number 13/RC/2073), Science Foundation Ireland's Career Development Award program (13CDA2221) and Science Foundation Ireland's National Access Programme (No. 444) and SFI 17/CDA/4733.

Conflicts of Interest: The authors declare no conflict of interest.

References

1. Jiang, N.; Zhuo, X.; Wang, J. Active Plasmonics: Principles, Structures, and Applications. *Chem. Rev.* **2018**, *118*, 3054–3099. [CrossRef] [PubMed]
2. Stockman, M.I.; Kneipp, K.; Bozhevolnyi, S.I.; Saha, S.; Dutta, A.; Ndukaife, J.; Kinsey, N.; Reddy, H.; Guler, U.; Shalaev, V.M.; et al. Roadmap on plasmonics. *J. Opt.* **2018**, *20*. [CrossRef]
3. Harutyunyan, H.; Martinson, A.B.; Rosenmann, D.; Khorashad, L.K.; Besteiro, L.V.; Govorov, A.O.; Wiederrecht, G.P. Anomalous ultrafast dynamics of hot plasmonic electrons in nanostructures with hot spots. *Nat. Nanotechnol.* **2015**, *10*, 770–774. [CrossRef]
4. Baffou, G.; Quidant, R. Nanoplasmonics for chemistry. *Chem. Soc. Rev.* **2014**, *43*, 3898–3907. [CrossRef] [PubMed]
5. Willets, K.A.; Van Duyne, R.P. Localized surface plasmon resonance spectroscopy and sensing. *Annu. Rev. Phys. Chem.* **2007**, *58*, 267–297. [CrossRef]
6. Huang, W.; Wang, J.; Bian, L.; Zhao, C.; Liu, D.; Guo, C.; Yang, B.; Cao, W. Oxygen vacancy induces self-doping effect and metalloid LSPR in non-stoichiometric tungsten suboxide synergistically contributing to the enhanced photoelectrocatalytic performance of WO3-x/TiO2-x heterojunction. *Phys. Chem. Chem. Phys.* **2018**, *20*, 17268–17278. [CrossRef]
7. Leonhardt, U. Optical conformal mapping. *Science* **2006**, *312*, 1777–1780. [CrossRef]
8. Wei, H.; Pan, D.; Xu, H. Routing of surface plasmons in silver nanowire networks controlled by polarization and coating. *Nanoscale* **2015**, *7*, 19053–19059. [CrossRef]
9. Mejia-Salazar, J.R.; Oliveira, O.N., Jr. Plasmonic Biosensing. *Chem. Rev.* **2018**, *118*, 10617–10625. [CrossRef]
10. Yu, C.; Irudayaraj, J. Multiplex Biosensor Using Gold Nanorods. *Anal. Chem.* **2007**, *79*, 572–579. [CrossRef]
11. Tian, F.; Bonnier, F.; Casey, A.; Shanahan, A.E.; Byrne, H.J. Surface enhanced Raman scattering with gold nanoparticles: Effect of particle shape. *Anal. Methods* **2014**, *6*, 9116–9123. [CrossRef]
12. Ringe, E.; Langille, M.R.; Sohn, K.; Zhang, J.; Huang, J.; Mirkin, C.A.; Van Duyne, R.P.; Marks, L.D. Plasmon Length: A Universal Parameter to Describe Size Effects in Gold Nanoparticles. *J. Phys. Chem. Lett.* **2012**, *3*, 1479–1483. [CrossRef] [PubMed]
13. Li, D. Femtosecond polarization switching. *Nat. Photonics* **2017**, *11*, 336–337. [CrossRef]
14. Yang, Y.; Kelley, K.; Sachet, E.; Campione, S.; Luk, T.S.; Maria, J.-P.; Sinclair, M.B.; Brener, I. Femtosecond optical polarization switching using a cadmium oxide-based perfect absorber. *Nat. Photonics* **2017**, *11*, 390–395. [CrossRef]
15. Schubert, O.; Becker, J.; Carbone, L.; Khalavka, Y.; Provalska, T.; Zins, I.; Sonnichsen, C. Mapping the polarization pattern of plasmon modes reveals nanoparticle symmetry. *Nano Lett.* **2008**, *8*, 2345–2350. [CrossRef]
16. Kumbhar, A.S.; Kinnan, M.K.; Chumanov, G. Multipole plasmon resonances of submicron silver particles. *J. Am. Chem. Soc.* **2005**, *127*, 12444–12445. [CrossRef]
17. Tian, X.; Zhou, Y.; Thota, S.; Zou, S.; Zhao, J. Plasmonic Coupling in Single Silver Nanosphere Assemblies by Polarization-Dependent Dark-Field Scattering Spectroscopy. *J. Phys. Chem. C* **2014**, *118*, 13801–13808. [CrossRef]
18. Shegai, T.; Li, Z.; Dadosh, T.; Zhang, Z.; Xu, H.; Haran, G. Managing light polarization via plasmon-molecule interactions within an asymmetric metal nanoparticle trimer. *Proc. Natl. Acad. Sci. USA* **2008**, *105*, 16448–16453. [CrossRef]

19. Luo, M.; Huang, H.; Choi, S.I.; Zhang, C.; da Silva, R.R.; Peng, H.C.; Li, Z.Y.; Liu, J.; He, Z.; Xia, Y. Facile Synthesis of Ag Nanorods with No Plasmon Resonance Peak in the Visible Region by Using Pd Decahedra of 16 nm in Size as Seeds. *ACS Nano* **2015**, *9*, 10523–10532. [CrossRef]
20. Shuford, K.L.; Ratner, M.A.; Schatz, G.C. Multipolar excitation in triangular nanoprisms. *J. Chem. Phys.* **2005**, *123*, 114713. [CrossRef]
21. Felidj, N.; Grand, J.; Laurent, G.; Aubard, J.; Levi, G.; Hohenau, A.; Galler, N.; Aussenegg, F.R.; Krenn, J.R. Multipolar surface plasmon peaks on gold nanotriangles. *J. Chem. Phys.* **2008**, *128*, 094702. [CrossRef] [PubMed]
22. Bukasov, R.; Shumaker-Parry, J.S. Highly tunable infrared extinction properties of gold nanocrescents. *Nano Lett.* **2007**, *7*, 1113–1118. [CrossRef] [PubMed]
23. Li, G.C.; Zhang, Y.L.; Lei, D.Y. Hybrid plasmonic gap modes in metal film-coupled dimers and their physical origins revealed by polarization resolved dark field spectroscopy. *Nanoscale* **2016**, *8*, 7119–7126. [CrossRef] [PubMed]
24. Chen, W.; Shi, H.; Wan, F.; Wang, P.; Gu, Z.; Li, W.; Ke, L.; Huang, Y. Substrate influence on the polarization dependence of SERS in crossed metal nanowires. *J. Mater. Chem. C* **2017**, *5*, 7028–7034. [CrossRef]
25. Wei, H.; Hao, F.; Huang, Y.; Wang, W.; Nordlander, P.; Xu, H. Polarization dependence of surface-enhanced Raman scattering in gold nanoparticle-nanowire systems. *Nano Lett.* **2008**, *8*, 2497–2502. [CrossRef]
26. Deng, G.; Dereshgi, S.A.; Song, X.; Aydin, K. Polarization dependent, plasmon-enhanced infrared transmission through gold nanoslits on monolayer black phosphorus. *J. Opt. Soc. Am. B* **2019**, *36*. [CrossRef]
27. Liu, C.; Bai, Y.; Zhou, J.; Zhao, Q.; Yang, Y.; Chen, H.; Qiao, L. High-performance bifunctional polarization switch chiral metamaterials by inverse design method. *npj Comput. Mater.* **2019**, *5*. [CrossRef]
28. Kaschke, J.; Blume, L.; Wu, L.; Thiel, M.; Bade, K.; Yang, Z.; Wegener, M. A Helical Metamaterial for Broadband Circular Polarization Conversion. *Adv. Opt. Mater.* **2015**, *3*, 1411–1417. [CrossRef]
29. Kruk, S.; Hopkins, B.; Kravchenko, I.I.; Miroshnichenko, A.; Neshev, D.N.; Kivshar, Y.S. Invited Article: Broadband highly efficient dielectric metadevices for polarization control. *APL Photonics* **2016**, *1*. [CrossRef]
30. Chen, S.; Liu, W.; Li, Z.; Cheng, H.; Tian, J. Polarization State Manipulation of Electromagnetic Waves with Metamaterials and Its Applications in Nanophotonics. In *Metamaterials—Devices and Applications*; IntechOpen Limited: London, UK, 2017. [CrossRef]
31. Bi, K.; Yang, D.; Chen, J.; Wang, Q.; Wu, H.; Lan, C.; Yang, Y. Experimental demonstration of ultra-large-scale terahertz all-dielectric metamaterials. *Photonics Res.* **2019**, *7*, 457–463. [CrossRef]
32. Soukoulis, C.M.; Wegener, M. Past achievements and future challenges in the development of three-dimensional photonic metamaterials. *Nat. Photonics* **2011**, *5*, 523–530. [CrossRef]
33. Tong, L.; Miljkovic, V.D.; Kall, M. Alignment, rotation, and spinning of single plasmonic nanoparticles and nanowires using polarization dependent optical forces. *Nano Lett.* **2010**, *10*, 268–273. [CrossRef] [PubMed]
34. Gunnarsson, L.; Rindzevicius, T.; Prikulis, J.; Kasemo, B.; Kall, M.; Zou, S.; Schatz, G.C. Confined plasmons in nanofabricated single silver particle pairs: Experimental observations of strong interparticle interactions. *J. Phys. Chem. B* **2005**, *109*, 1079–1087. [CrossRef] [PubMed]
35. Dort, K.; Kroth, K.; Klar, P.J. A surface-enhanced Raman-spectroscopic study: Verification of the interparticle gap dependence of field enhancement by triangulation of spherical gold nanoparticle trimers. *J. Raman Spectrosc.* **2019**, *50*, 1807–1816. [CrossRef]
36. Steinigeweg, D.; Schutz, M.; Schlucker, S. Single gold trimers and 3D superstructures exhibit a polarization-independent SERS response. *Nanoscale* **2013**, *5*, 110–113. [CrossRef]
37. Wang, H.; Li, Z.; Zhang, H.; Wang, P.; Wen, S. Giant local circular dichroism within an asymmetric plasmonic nanoparticle trimer. *Sci. Rep.* **2015**, *5*, 8207. [CrossRef]
38. Mohamed, M.B.; Volkov, V.; Link, S.; El-Sayed, M.A. The 'lightning' gold nanorods: Fluorescence enhancement of over a million compared to the gold metal. *Chem. Phys. Lett.* **2000**, *317*, 517–523. [CrossRef]
39. Sonnichsen, C.; Franzl, T.; Wilk, T.; von Plessen, G.; Feldmann, J.; Wilson, O.; Mulvaney, P. Drastic reduction of plasmon damping in gold nanorods. *Phys. Rev. Lett.* **2002**, *88*, 077402. [CrossRef]
40. Slaughter, L.S.; Chang, W.-S.; Swanglap, P.; Tcherniak, A.; Khanal, B.P.; Zubarev, E.R.; Link, S. Single-Particle Spectroscopy of Gold Nanorods beyond the Quasi-Static Limit: Varying the Width at Constant Aspect Ratio. *J. Phys. Chem. C* **2010**, *114*, 4934–4938. [CrossRef]

41. He, J.; Zheng, W.; Ligmajer, F.; Chan, C.F.; Bao, Z.; Wong, K.L.; Chen, X.; Hao, J.; Dai, J.; Yu, S.F.; et al. Plasmonic enhancement and polarization dependence of nonlinear upconversion emissions from single gold nanorod@SiO2@CaF2:Yb(3+),Er(3+) hybrid core-shell-satellite nanostructures. *Light Sci. Appl.* **2017**, *6*, e16217. [CrossRef]
42. Khlebtsov, B.N.; Khlebtsov, N.G. Multipole Plasmons in Metal Nanorods: Scaling Properties and Dependence on Particle Size, Shape, Orientation, and Dielectric Environment. *J. Phys. Chem. C* **2007**, *111*, 11516–11527. [CrossRef]
43. Aizpurua, J.; Bryant, G.W.; Richter, L.J.; García de Abajo, F.J.; Kelley, B.K.; Mallouk, T. Optical properties of coupled metallic nanorods for field-enhanced spectroscopy. *Phys. Rev. B* **2005**, *71*, 235420. [CrossRef]
44. Ming, T.; Zhao, L.; Yang, Z.; Chen, H.; Sun, L.; Wang, J.; Yan, C. Strong polarization dependence of plasmon-enhanced fluorescence on single gold nanorods. *Nano Lett.* **2009**, *9*, 3896–3903. [CrossRef] [PubMed]
45. Yguerabide, J.; Yguerabide, E.E. Light-Scattering Submicroscopic Particles as Highly Fluorescent Analogs and Their Use as Tracer Labels in Clinical and Biological Applications: I. Theory. *Anal. Biochem.* **1998**, *262*, 137–156. [CrossRef]
46. Zijlstra, P.; Chon, J.W.; Gu, M. Five-dimensional optical recording mediated by surface plasmons in gold nanorods. *Nature* **2009**, *459*, 410–413. [CrossRef]
47. Diefenbach, S.; Erhard, N.; Schopka, J.; Martin, A.; Karnetzky, C.; Iacopino, D.; Holleitner, A.W. Polarization dependent, surface plasmon induced photoconductance in gold nanorod arrays. *Phys. Status Solidi (RRL)—Rapid Res. Lett.* **2014**, *8*, 264–268. [CrossRef]
48. Ruan, Q.; Fang, C.; Jiang, R.; Jia, H.; Lai, Y.; Wang, J.; Lin, H.Q. Highly enhanced transverse plasmon resonance and tunable double Fano resonances in gold@titania nanorods. *Nanoscale* **2016**, *8*, 6514–6526. [CrossRef]
49. Zhang, M.; Li, C.; Wang, C.; Zhang, C.; Wang, Z.; Han, Q.; Zheng, H. Polarization dependence of plasmon enhanced fluorescence on Au nanorod array. *Appl. Opt.* **2017**, *56*, 375–379. [CrossRef] [PubMed]
50. Sun, M.; Zhang, Z.; Wang, P.; Li, Q.; Ma, F.; Xu, H. Remotely excited Raman optical activity using chiral plasmon propagation in Ag nanowires. *Light Sci. Appl.* **2013**, *2*, e112. [CrossRef]
51. Kim, S.; Bailey, S.; Liu, M.; Yan, R. Decoupling co-existing surface plasmon polariton (SPP) modes in a nanowire plasmonic waveguide for quantitative mode analysis. *Nano Res.* **2017**, *10*, 2395–2404. [CrossRef]
52. Vasista, A.B.; Jog, H.; Heilpern, T.; Sykes, M.E.; Tiwari, S.; Sharma, D.K.; Chaubey, S.K.; Wiederrecht, G.P.; Gray, S.K.; Kumar, G.V.P. Differential Wavevector Distribution of Surface-Enhanced Raman Scattering and Fluorescence in a Film-Coupled Plasmonic Nanowire Cavity. *Nano Lett.* **2018**, *18*, 650–655. [CrossRef] [PubMed]
53. Zhang, Z.; Fang, Y.; Wang, W.; Chen, L.; Sun, M. Propagating Surface Plasmon Polaritons: Towards Applications for Remote-Excitation Surface Catalytic Reactions. *Adv. Sci. (Weinh)* **2016**, *3*, 1500215. [CrossRef] [PubMed]
54. Mohanty, P.; Yoon, I.; Kang, T.; Seo, K.; Varadwaj, K.S.K.; Choi, W.; Park, Q.H.; Ahn, J.P.; Suh, Y.D.; Ihee, H.; et al. Simple Vapor-Phase Synthesis of Single-Crystalline Ag Nanowires and Single-Nanowire Surface-Enhanced Raman Scattering. *J. Am. Chem. Soc.* **2007**, *129*, 9576–9577. [CrossRef] [PubMed]
55. Li, Z.; Gao, Y.; Zhang, L.; Fang, Y.; Wang, P. Polarization-dependent surface plasmon-driven catalytic reaction on a single nanowire monitored by SERS. *Nanoscale* **2018**, *10*, 18720–18727. [CrossRef] [PubMed]
56. Hao, F.; Nordlander, P. Plasmonic coupling between a metallic nanosphere and a thin metallic wire. *Appl. Phys. Lett.* **2006**, *89*, 103101. [CrossRef]
57. Hu, H.; Akimov, Y.A.; Duan, H.; Li, X.; Liao, M.; Tan, R.L.; Wu, L.; Chen, H.; Fan, H.; Bai, P.; et al. Photoluminescence via gap plasmons between single silver nanowires and a thin gold film. *Nanoscale* **2013**, *5*, 12086–12091. [CrossRef]
58. Yang, M.; Cai, W.; Wang, Y.; Sun, M.; Shang, G. Orientation-and polarization-dependent optical properties of the single Ag nanowire/glass substrate system excited by the evanescent wave. *Sci. Rep.* **2016**, *6*, 25633. [CrossRef]
59. Lee, S.J.; Baik, J.M.; Moskovits, M. Polarization-dependent surface-enhanced Raman scattering from a silver-nanoparticle-decorated single silver nanowire. *Nano Lett.* **2008**, *8*, 3244–3247. [CrossRef]
60. Fang, Y.; Li, Z.; Huang, Y.; Zhang, S.; Nordlander, P.; Halas, N.J.; Xu, H. Branched silver nanowires as controllable plasmon routers. *Nano Lett.* **2010**, *10*, 1950–1954. [CrossRef]

61. Liu, N.; Li, Z.; Xu, H. Polarization-dependent study on propagating surface plasmons in silver nanowires launched by a near-field scanning optical fiber tip. *Small* **2012**, *8*, 2641–2646. [CrossRef]
62. Chen, L.; Rong, Y.; Ren, M.; Wu, W.; Qin, M.; Pan, C.; Ma, Q.; Liu, S.; Wu, B.; Wu, E.; et al. Selective Polarization Modification of Upconversion Luminescence of NaYF4:Yb3+,Er3+ Nanoparticles by Plasmonic Nanoantenna Arrays. *J. Phys. Chem. C* **2018**, *122*, 15666–15672. [CrossRef]
63. Mobini, E.; Rahimzadegan, A.; Alaee, R.; Rockstuhl, C. Optical alignment of oval graphene flakes. *Opt. Lett.* **2017**, *42*, 1039–1042. [CrossRef] [PubMed]
64. Chen, J.; Zeng, Y.; Xu, X.; Chen, X.; Zhou, Z.; Shi, P.; Yi, Z.; Ye, X.; Xiao, S.; Yi, Y. Plasmonic Absorption Enhancement in Elliptical Graphene Arrays. *Nanomaterials* **2018**, *8*, 175. [CrossRef]
65. Guler, U.; Turan, R. Effect of particle properties and light polarization on the plasmonic resonances in metallic nanoparticles. *Opt. Express* **2010**, *18*, 17322–17338. [CrossRef] [PubMed]
66. Xia, Y.; Dai, Y.; Wang, B.; Chen, A.; Zhang, Y.; Zhang, Y.; Guan, F.; Liu, X.; Shi, L.; Zi, J. Polarization dependent plasmonic modes in elliptical graphene disk arrays. *Opt. Express* **2019**, *27*, 1080–1089. [CrossRef]
67. Gordon, R.; Brolo, A.G.; McKinnon, A.; Rajora, A.; Leathem, B.; Kavanagh, K.L. Strong Polarization in the Optical Transmission through Elliptical Nanohole Arrays. *Phys. Rev. Lett.* **2004**, *92*, 037401. [CrossRef]
68. Sepulveda, B.; Alaverdyan, Y.; Alegret, J.; Kall, M.; Johansson, P. Shape effects in the localized surface plasmon resonance of single nanoholes in thin metal films. *Opt. Express* **2008**, *16*, 5609–5616. [CrossRef]
69. Petronijevic, E.; Ali, H.; Zaric, N.; Belardini, A.; Leahu, G.; Cesca, T.; Mattei, G.; Andreani, L.C.; Sibilia, C. Chiral effects in low-cost plasmonic arrays of elliptic nanoholes. *Opt. Quantum Electron.* **2020**, *52*, 176. [CrossRef]
70. Hermoso, W.; Alves, T.V.; de Oliveira, C.C.S.; Moriya, E.G.; Ornellas, F.R.; Camargo, P.H.C. Triangular metal nanoprisms of Ag, Au, and Cu: Modeling the influence of size, composition, and excitation wavelength on the optical properties. *Chem. Phys.* **2013**, *423*, 142–150. [CrossRef]
71. Sherry, L.J.; Jin, R.; Mirkin, C.A.; Schatz, G.C.; Van Duyne, R.P. Localized Surface Plasmon Resonance Spectroscopy of Single Silver Triangular Nanoprisms. *Nano Lett.* **2006**, *6*, 2060–2065. [CrossRef]
72. Shahjamali, M.M.; Bosman, M.; Cao, S.; Huang, X.; Saadat, S.; Martinsson, E.; Aili, D.; Tay, Y.Y.; Liedberg, B.; Loo, S.C.J.; et al. Gold Coating of Silver Nanoprisms. *Adv. Funct. Mater.* **2012**, *22*, 849–854. [CrossRef]
73. Sweeney, C.M.; Stender, C.L.; Nehl, C.L.; Hasan, W.; Shuford, K.L.; Odom, T.W. Optical properties of tipless gold nanopyramids. *Small* **2011**, *7*, 2032–2036. [CrossRef] [PubMed]
74. Gao, M.; Zheng, X.; Khan, I.; Cai, H.; Lan, J.; Liu, J.; Wang, J.; Wu, J.; Huang, S.; Li, S.; et al. Resonant light absorption and plasmon tunability of lateral triangular Au nanoprisms array. *Phys. Lett. A* **2019**, *383*. [CrossRef]
75. Banholzer, M.J.; Harris, N.; Millstone, J.E.; Schatz, G.C.; Mirkin, C.A. Abnormally Large Plasmonic Shifts in Silica-Protected Gold Triangular Nanoprisms. *J. Phys. Chem. C* **2010**, *114*, 7521–7526. [CrossRef]
76. Love, J.C.; Gates, B.D.; Wolfe, D.B.; Paul, K.E.; Whitesides, G.M. Fabrication and Wetting Properties of Metallic Half-Shells with Submicron Diameters. *Nano Lett.* **2002**, *2*, 891–894. [CrossRef]
77. Lu, Y.; Liu, G.L.; Kim, J.; Mejia, Y.X.; Lee, L.P. Nanophotonic Crescent Moon Structures with Sharp Edge for Ultrasensitive Biomolecular Detection by Local Electromagnetic Field Enhancement Effect. *Nano Lett.* **2005**, *5*, 119–124. [CrossRef]
78. Shumaker-Parry, J.S.; Rochholz, H.; Kreiter, M. Fabrication of Crescent-Shaped Optical Antennas. *Adv. Mater.* **2005**, *17*, 2131–2134. [CrossRef]
79. Cooper, C.T.; Rodriguez, M.; Blair, S.; Shumaker-Parry, J.S. Polarization Anisotropy of Multiple Localized Plasmon Resonance Modes in Noble Metal Nanocrescents. *J. Phys. Chem. C* **2013**, *118*, 1167–1173. [CrossRef]
80. Won Ha, J.; Sun, W.; Wang, G.; Fang, N. Differential interference contrast polarization anisotropy for tracking rotational dynamics of gold nanorods. *Chem. Commun.* **2011**, *47*, 7743–7745. [CrossRef]
81. Goerlitzer, E.S.A.; Speichermann, L.E.; Mirza, T.A.; Mohammadi, R.; Vogel, N. Addressing the plasmonic hotspot region by site-specific functionalization of nanostructures. *Nanoscale Adv.* **2020**, *2*, 394–400. [CrossRef]
82. Zhang, Y.; Jia, T.Q.; Zhang, S.A.; Feng, D.H.; Xu, Z.Z. Dipole, quadrupole and octupole plasmon resonance modes in non-concentric nanocrescent/nanodisk structure: Local field enhancement in the visible and near infrared regions. *Opt. Express* **2012**, *20*, 2924–2931. [CrossRef] [PubMed]
83. Garoli, D.; Mosconi, D.; Miele, E.; Maccaferri, N.; Ardini, M.; Giovannini, G.; Dipalo, M.; Agnoli, S.; De Angelis, F. Hybrid plasmonic nanostructures based on controlled integration of MoS2 flakes on metallic nanoholes. *Nanoscale* **2018**, *10*, 17105–17111. [CrossRef]

84. Late, D.J.; Liu, B.; Luo, J.; Yan, A.; Matte, H.S.; Grayson, M.; Rao, C.N.; Dravid, V.P. GaS and GaSe ultrathin layer transistors. *Adv. Mater.* **2012**, *24*, 3549–3554. [CrossRef] [PubMed]
85. Hu, P.; Wang, L.; Yoon, M.; Zhang, J.; Feng, W.; Wang, X.; Wen, Z.; Idrobo, J.C.; Miyamoto, Y.; Geohegan, D.B.; et al. Highly Responsive Ultrathin GaS Nanosheet Photodetectors on Rigid and Flexible Substrates. *Nano Lett.* **2013**, *13*, 1649–1654. [CrossRef]
86. Gan, X.-T.; Zhao, C.-Y.; Hu, S.-Q.; Wang, T.; Song, Y.; Li, J.; Zhao, Q.-H.; Jie, W.-Q.; Zhao, J.-L. Microwatts continuous-wave pumped second harmonic generation in few- and mono-layer GaSe. *Light Sci. Appl.* **2018**, *7*, 17126. [CrossRef] [PubMed]
87. Ding, S.-Y.; Yi, J.; Li, J.-F.; Ren, B.; Wu, D.-Y.; Panneerselvam, R.; Tian, Z.-Q. Nanostructure-based plasmon-enhanced Raman spectroscopy for surface analysis of materials. *Nat. Rev. Mater.* **2016**, *1*, 16021. [CrossRef]
88. Seo, S.; Chang, T.-W.; Liu, G.L. 3D Plasmon Coupling Assisted Sers on Nanoparticle-Nanocup Array Hybrids. *Sci. Rep.* **2018**, *8*, 3002. [CrossRef]
89. Najmaei, S.; Mlayah, A.; Arbouet, A.; Girard, C.; Léotin, J.; Lou, J. Plasmonic Pumping of Excitonic Photoluminescence in Hybrid MoS2–Au Nanostructures. *ACS Nano* **2014**, *8*, 12682–12689. [CrossRef]
90. Rodin, A.S.; Carvalho, A.; Castro Neto, A.H. Strain-induced gap modification in black phosphorus. *Phys. Rev. Lett.* **2014**, *112*, 176801. [CrossRef]
91. Qiao, J.; Kong, X.; Hu, Z.X.; Yang, F.; Ji, W. High-mobility transport anisotropy and linear dichroism in few-layer black phosphorus. *Nat. Commun.* **2014**, *5*, 4475. [CrossRef]
92. Jappor, H.R. Electronic structure of novel GaS/GaSe heterostructures based on GaS and GaSe monolayers. *Phys. B Condens. Matter* **2017**, *524*, 109–117. [CrossRef]
93. Wan, W.; Yin, J.; Wu, Y.; Zheng, X.; Yang, W.; Wang, H.; Zhou, J.; Chen, J.; Wu, Z.; Li, X.; et al. Polarization-Controllable Plasmonic Enhancement on the Optical Response of Two-Dimensional GaSe Layers. *ACS Appl. Mater. Interfaces* **2019**, *11*, 19631–19637. [CrossRef] [PubMed]
94. Ozbay, E. Plasmonics: Merging photonics and electronics at nanoscale dimensions. *Science* **2006**, *311*, 189–193. [CrossRef] [PubMed]
95. Liang, Z.; Sun, J.; Jiang, Y.; Jiang, L.; Chen, X. Plasmonic Enhanced Optoelectronic Devices. *Plasmonics* **2014**, *9*, 859–866. [CrossRef]
96. Dionne, J.A.; Sweatlock, L.A.; Sheldon, M.T.; Alivisatos, A.P.; Atwater, H.A. 2010_Silicon-Based Plasmonics for On-Chip Photonics.pdf. *IEEE J. Sel. Top. Quantum Electron.* **2010**, *16*, 295–306. [CrossRef]
97. Špačková, B.; Wrobel, P.; Bocková, M.; Homola, J. Optical Biosensors Based on Plasmonic Nanostructures: A Review. *Proc. IEEE* **2016**, *104*, 2380–2408. [CrossRef]
98. Strobbia, P.; Languirand, E.; Cullum, B.M. Recent advances in plasmonic nanostructures for sensing: A review. *Opt. Eng.* **2015**, *54*, 100902. [CrossRef]
99. Guo, X.; Ma, Y.; Wang, Y.; Tong, L. Nanowire plasmonic waveguides, circuits and devices. *Laser Photonics Rev.* **2013**, *7*, 855–881. [CrossRef]
100. Fang, Y.; Sun, M. Nanoplasmonic waveguides: Towards applications in integrated nanophotonic circuits. *Light Sci. Appl.* **2015**, *4*, 1–11. [CrossRef]
101. Kleinman, S.L.; Ringe, E.; Valley, N.; Wustholz, K.L.; Phillips, E.; Scheidt, K.A.; Schatz, G.C.; Van Duyne, R.P. Single-molecule surface-enhanced raman spectroscopy of crystal violet isotopologues: Theory and experiment. *J. Am. Chem. Soc.* **2011**, *133*, 4115–4122. [CrossRef]
102. Zhang, Y.; Zhen, Y.R.; Neumann, O.; Day, J.K.; Nordlander, P.; Halas, N.J. Coherent anti-Stokes Raman scattering with single-molecule sensitivity using a plasmonic Fano resonance. *Nat. Commun.* **2014**, *5*, 1–7. [CrossRef] [PubMed]
103. Zheng, Y.; Soeriyadi, A.H.; Rosa, L.; Ng, S.H.; Bach, U.; Justin Gooding, J. Reversible gating of smart plasmonic molecular traps using thermoresponsive polymers for single-molecule detection. *Nat. Commun.* **2015**, *6*, 1–8. [CrossRef] [PubMed]
104. Brandl, D.W.; Mirin, N.A.; Nordlander, P. Plasmon modes of nanosphere trimers and quadrumers. *J. Phys. Chem. B* **2006**, *110*, 12302–12310. [CrossRef]
105. Lee, H.; Kim, G.H.; Lee, J.H.; Kim, N.H.; Nam, J.M.; Suh, Y.D. Quantitative Plasmon Mode and Surface-Enhanced Raman Scattering Analyses of Strongly Coupled Plasmonic Nanotrimers with Diverse Geometries. *Nano Lett.* **2015**, *15*, 4628–4636. [CrossRef] [PubMed]

106. Thomas, R.; Swathi, R.S. Linear and Polygonal Assemblies of Plasmonic Nanoparticles: Incident Light Polarization Dictates Hot Spots. *J. Phys. Chem. C* **2016**, *120*, 18733–18740. [CrossRef]
107. Sönnichsen, C.; Alivisatos, A.P. Gold nanorods as novel nonbleaching plasmon-based orientation sensors for polarized single-particle microscopy. *Nano Lett.* **2005**, *5*, 301–304. [CrossRef] [PubMed]
108. Wei, H.; Li, Z.; Tian, X.; Wang, Z.; Cong, F.; Liu, N.; Zhang, S.; Nordlander, P.; Halas, N.J.; Xu, H. Quantum dot-based local field imaging reveals plasmon-based interferometric logic in silver nanowire networks. *Nano Lett.* **2011**, *11*, 471–475. [CrossRef]
109. Wei, H.; Wang, Z.; Tian, X.; Käll, M.; Xu, H. Cascaded logic gates in nanophotonic plasmon networks. *Nat. Commun.* **2011**, *2*, 385–387. [CrossRef]
110. Ditlbacher, H.; Hohenau, A.; Wagner, D.; Kreibig, U.; Rogers, M.; Hofer, F.; Aussenegg, F.R.; Krenn, J.R. Silver nanowires as surface plasmon resonators. *Phys. Rev. Lett.* **2005**, *95*, 1–4. [CrossRef]
111. Ma, Y.; Li, X.; Yu, H.; Tong, L.; Gu, Y.; Gong, Q. Direct measurement of propagation losses in silver nanowires. *Opt. Lett.* **2010**, *35*, 1160–1162. [CrossRef] [PubMed]
112. Sanders, A.W.; Routenberg, D.A.; Wiley, B.J.; Xia, Y.; Dufresne, E.R.; Reed, M.A. Observation of plasmon propagation, redirection, and fan-out in silver nanowires. *Nano Lett.* **2006**, *6*, 1822–1826. [CrossRef] [PubMed]
113. Wei, H.; Xu, H. Controlling surface plasmon interference in branched silver nanowire structures. *Nanoscale* **2012**, *4*, 7149–7154. [CrossRef] [PubMed]
114. Righini, M.; Zelenina, A.S.; Girard, C.; Quidant, R. Parallel and selective trapping in a patterned plasmonic landscape. *Nat. Phys.* **2007**, *3*, 477–480. [CrossRef]
115. Daly, M.; Truong, V.G.; Chormaic, S.N. Evanescent field trapping of nanoparticles using nanostructured ultrathin optical fibers. *Opt. Express* **2016**, *24*, 14470. [CrossRef] [PubMed]
116. Tsai, W.Y.; Huang, J.S.; Huang, B.C. Selective trapping or rotation of isotropic dielectric microparticles by optical near field in a plasmonic archimedes spiral. *Nano Lett.* **2014**, *14*, 547–552. [CrossRef]
117. Wang, K.; Schonbrun, E.; Steinvurzel, P.; Crozier, K.B. Trapping and rotating nanoparticles using a plasmonic nano-tweezer with an integrated heat sink. *Nat. Commun.* **2011**, *2*. [CrossRef]
118. Yang, C.; Pan, D.; Tong, L.; Xu, H. Guided transport of nanoparticles by plasmonic nanowires. *Nanoscale* **2016**, *8*, 19195–19199. [CrossRef]
119. Dasgupta, A.; Singh, D.; Pavan Kumar, V.G. Dual-path remote-excitation surface enhanced Raman microscopy with plasmonic nanowire dimer. *Appl. Phys. Lett.* **2013**, *103*. [CrossRef]
120. Kumar, G.V.P. Plasmonic nano-architectures for surface enhanced Raman scattering: A review. *J. Nanophotonics* **2012**, *6*, 064503. [CrossRef]
121. Ru, L.E.C.; Blackie, E.; Meyer, M.; Etchegoin, P.G. Surface Enhanced Raman Scattering Enhancement Factors: A Comprehensive Study. *J. Phys. Chem. C* **2007**, *111*, 13794. [CrossRef]
122. Wang, A.X.; Kong, X. Review of recent progress of plasmonic materials and nano-structures for surface-enhanced raman scattering. *Materials* **2015**, *8*, 3024–3052. [CrossRef] [PubMed]
123. Huang, Y.; Fang, Y.; Zhang, Z.; Zhu, L.; Sun, M. Nanowire-supported plasmonic waveguide for remote excitation of surface-enhanced Raman scattering. *Light Sci. Appl.* **2014**, *3*. [CrossRef]
124. Cui, Y.; Hegde, R.S.; Phang, I.Y.; Lee, H.K.; Ling, X.Y. Encoding molecular information in plasmonic nanostructures for anti-counterfeiting applications. *Nanoscale* **2014**, *6*, 282–288. [CrossRef] [PubMed]
125. Cui, Y.; Phang, I.Y.; Lee, Y.H.; Lee, M.R.; Zhang, Q.; Ling, X.Y. Multiplex plasmonic anti-counterfeiting security labels based on surface-enhanced Raman scattering. *Chem. Commun.* **2015**, *51*, 5363–5366. [CrossRef]
126. Heeg, S.; Fernandez-Garcia, R.; Oikonomou, A.; Schedin, F.; Narula, R.; Maier, S.A.; Vijayaraghavan, A.; Reich, S. Polarized plasmonic enhancement by Au nanostructures probed through raman scattering of suspended graphene. *Nano Lett.* **2013**, *13*, 301–308. [CrossRef]
127. Venuthurumilli, P.K.; Ye, P.D.; Xu, X. Plasmonic Resonance Enhanced Polarization-Sensitive Photodetection by Black Phosphorus in Near Infrared. *ACS Nano* **2018**, *12*, 4861–4867. [CrossRef]
128. Li, Q.; Lu, J.; Gupta, P.; Qiu, M. Engineering Optical Absorption in Graphene and Other 2D Materials: Advances and Applications. *Adv. Opt. Mater.* **2019**, *7*, 1900595. [CrossRef]
129. Yuan, H.; Liu, X.; Afshinmanesh, F.; Li, W.; Xu, G.; Sun, J.; Lian, B.; Curto, A.G.; Ye, G.; Hikita, Y.; et al. Polarization-sensitive broadband photodetector using a black phosphorus vertical p-n junction. *Nat. Nanotechnol.* **2015**, *10*, 707–713. [CrossRef]
130. Kinzel, E.C.; Xu, X. Extraordinary infrared transmission through a periodic bowtie aperture array. *Opt. Lett.* **2010**, *35*, 992. [CrossRef]

131. Zheludev, N.I. Applied physics. The road ahead for metamaterials. *Science* **2010**, *328*, 582–583. [CrossRef]
132. Zheludev, N.I. Applied physics. Obtaining optical properties on demand. *Science* **2015**, *348*, 973–974. [CrossRef] [PubMed]
133. Li, J.; Yu, P.; Cheng, H.; Liu, W.; Li, Z.; Xie, B.; Chen, S.; Tian, J. Optical Polarization Encoding Using Graphene-Loaded Plasmonic Metasurfaces. *Adv. Opt. Mater.* **2016**, *4*, 91–98. [CrossRef]
134. Shen, N.H.; Massaouti, M.; Gokkavas, M.; Manceau, J.M.; Ozbay, E.; Kafesaki, M.; Koschny, T.; Tzortzakis, S.; Soukoulis, C.M. Optically implemented broadband blueshift switch in the terahertz regime. *Phys. Rev. Lett.* **2011**, *106*, 037403. [CrossRef]
135. Valmorra, F.; Scalari, G.; Maissen, C.; Fu, W.; Schönenberger, C.; Choi, J.W.; Park, H.G.; Beck, M.; Faist, J. Low-Bias Active Control of Terahertz Waves by Coupling Large-Area CVD Graphene to a Terahertz Metamaterial. *Nano Lett.* **2013**, *13*, 3193–3198. [CrossRef] [PubMed]
136. Liu, Y.; Ling, X.; Yi, X.; Zhou, X.; Chen, S.; Ke, Y.; Luo, H.; Wen, S. Photonic spin Hall effect in dielectric metasurfaces with rotational symmetry breaking. *Opt. Lett.* **2015**, *40*, 756–759. [CrossRef]
137. Shu, W.; Ke, Y.; Liu, Y.; Ling, X.; Luo, H.; Yin, X. Radial spin Hall effect of light. *Phys. Rev. A* **2016**, *93*, 013839. [CrossRef]
138. Barry, R.M. Fundamentals of Photonics, Second Edition. *J. Biomed. Opt.* **2008**, *13*, 1–4. [CrossRef]
139. She, J.; Shen, S.; Wang, Q. Optimal design of achromatic quarter-wave plate using twisted nematic liquid crystal cells. *Opt. Quantum Electron.* **2005**, *37*, 625–634. [CrossRef]
140. Shelby, R.A.; Smith, D.R.; Schultz, S. Experimental verification of a negative index of refraction. *Science* **2001**, *292*, 77–79. [CrossRef] [PubMed]
141. Pendry, J.B.; Schurig, D.; Smith, D.R. Controlling electromagnetic fields. *Science* **2006**, *312*, 1780–1782. [CrossRef]
142. Ni, X.; Wong, Z.J.; Mrejen, M.; Wang, Y.; Zhang, X. An ultrathin invisibility skin cloak for visible light. *Science* **2015**, *349*, 1310. [CrossRef] [PubMed]
143. Won, R. The rise of plasmonic metasurfaces. *Nature Photonics* **2017**, *11*, 462–464. [CrossRef]
144. Kildishev, A.V.; Boltasseva, A.; Shalaev, V.M. Planar photonics with metasurfaces. *Science* **2013**, *339*, 1232009. [CrossRef] [PubMed]
145. Liu, Z.; Li, Z.; Liu, Z.; Li, J.; Cheng, H.; Yu, P.; Liu, W.; Tang, C.; Gu, C.; Li, J.; et al. High-Performance Broadband Circularly Polarized Beam Deflector by Mirror Effect of Multinanorod Metasurfaces. *Adv. Funct. Mater.* **2015**, *25*, 5428–5434. [CrossRef]
146. Pors, A.; Nielsen, M.G.; Della Valle, G.; Willatzen, M.; Albrektsen, O.; Bozhevolnyi, S.I. Plasmonic metamaterial wave retarders in reflection by orthogonally oriented detuned electrical dipoles. *Opt. Lett.* **2011**, *36*, 1626–1628. [CrossRef]
147. Zhao, Y.; Alù, A. Tailoring the Dispersion of Plasmonic Nanorods to Realize Broadband Optical Meta-Waveplates. *Nano Lett.* **2013**, *13*, 1086–1091. [CrossRef]
148. Ellenbogen, T.; Seo, K.; Crozier, K.B. Chromatic plasmonic polarizers for active visible color filtering and polarimetry. *Nano Lett.* **2012**, *12*, 1026–1031. [CrossRef]
149. Li, T.; Liu, H.; Wang, S.-M.; Yin, X.-G.; Wang, F.-M.; Zhu, S.-N.; Zhang, X. Manipulating optical rotation in extraordinary transmission by hybrid plasmonic excitations. *Appl. Phys. Lett.* **2008**, *93*, 021110. [CrossRef]
150. Sung, J.; Sukharev, M.; Hicks, E.M.; Van Duyne, R.P.; Seideman, T.; Spears, K.G. Nanoparticle Spectroscopy: Birefringence in Two-Dimensional Arrays of L-Shaped Silver Nanoparticles. *J. Phys. Chem. C* **2008**, *112*, 3252–3260. [CrossRef]
151. Wu, S.; Zhang, Z.; Zhang, Y.; Zhang, K.; Zhou, L.; Zhang, X.; Zhu, Y. Enhanced Rotation of the Polarization of a Light Beam Transmitted through a Silver Film with an Array of Perforated S-Shaped Holes. *Phys. Rev. Lett.* **2013**, *110*, 207401. [CrossRef]
152. Zhang, S.; Zhou, J.; Park, Y.S.; Rho, J.; Singh, R.; Nam, S.; Azad, A.K.; Chen, H.T.; Yin, X.; Taylor, A.J.; et al. Photoinduced handedness switching in terahertz chiral metamolecules. *Nat. Commun.* **2012**, *3*, 942. [CrossRef] [PubMed]
153. Yin, X.; Schaferling, M.; Michel, A.K.; Tittl, A.; Wuttig, M.; Taubner, T.; Giessen, H. Active Chiral Plasmonics. *Nano Lett.* **2015**, *15*, 4255–4260. [CrossRef] [PubMed]
154. Jiang, Z.H.; Lin, L.; Ma, D.; Yun, S.; Werner, D.H.; Liu, Z.; Mayer, T.S. Broadband and wide field-of-view plasmonic metasurface-enabled waveplates. *Sci. Rep.* **2014**, *4*, 7511. [CrossRef] [PubMed]

155. Wu, C.; Arju, N.; Kelp, G.; Fan, J.A.; Dominguez, J.; Gonzales, E.; Tutuc, E.; Brener, I.; Shvets, G. Spectrally selective chiral silicon metasurfaces based on infrared Fano resonances. *Nat. Commun.* **2014**, *5*, 3892. [CrossRef]
156. Stokes, G.G. On the Composition and Resolution of Streams of Polarized Light from different Sources. *Trans. Camb. Philos. Soc.* **1851**, *9*, 399.
157. Ye, Y.; He, S. 90° polarization rotator using a bilayered chiral metamaterial with giant optical activity. *Appl. Phys. Lett.* **2010**, *96*, 203501. [CrossRef]
158. Chin, J.Y.; Lu, M.; Cui, T.J. Metamaterial polarizers by electric-field-coupled resonators. *Appl. Phys. Lett.* **2008**, *93*, 251903. [CrossRef]
159. Cui, J.; Huang, C.; Pan, W.; Pu, M.; Guo, Y.; Luo, X. Dynamical manipulation of electromagnetic polarization using anisotropic meta-mirror. *Sci. Rep.* **2016**, *6*, 30771. [CrossRef] [PubMed]
160. Federici, J.F.; Schulkin, B.; Huang, F.; Gary, D.; Barat, R.; Oliveira, F.; Zimdars, D. THz imaging and sensing for security applications—explosives, weapons and drugs. *Semicond. Sci. Technol.* **2005**, *20*, S266–S280. [CrossRef]
161. Piesiewicz, R.; Kleine-Ostmann, T.; Krumbholz, N.; Mittleman, D.; Koch, M.; Schoebel, J.; Kurner, T. Short-Range Ultra-Broadband Terahertz Communications: Concepts and Perspectives. *IEEE Antennas Propag. Mag.* **2007**, *49*, 24–39. [CrossRef]
162. Ho, I.C.; Guo, X.; Zhang, X.C. Design and performance of reflective terahertz air-biased-coherent-detection for time-domain spectroscopy. *Opt. Express* **2010**, *18*, 2872–2883. [CrossRef] [PubMed]
163. Cong, L.; Cao, W.; Tian, Z.; Gu, J.; Han, J.; Zhang, W. Manipulating polarization states of terahertz radiation using metamaterials. *New J. Phys.* **2012**, *14*, 115013. [CrossRef]
164. Cong, L.; Cao, W.; Zhang, X.; Tian, Z.; Gu, J.; Singh, R.; Han, J.; Zhang, W. A perfect metamaterial polarization rotator. *Appl. Phys. Lett.* **2013**, *103*, 171107. [CrossRef]
165. Zhao, Y.; Alù, A. Manipulating light polarization with ultrathin plasmonic metasurfaces. *Phys. Rev. B* **2011**, *84*, 205428. [CrossRef]
166. Cong, L.; Xu, N.; Gu, J.; Singh, R.; Han, J.; Zhang, W. Highly flexible broadband terahertz metamaterial quarter-wave plate. *Laser Photonics Rev.* **2014**, *8*, 626–632. [CrossRef]
167. Jiang, Y.; Zhao, H.; Wang, L.; Wang, J.; Cao, W.; Wang, Y. Broadband linear-to-circular polarization converter based on phosphorene metamaterial. *Opt. Mater. Express* **2019**, *9*. [CrossRef]
168. Pan, C.; Ren, M.; Li, Q.; Fan, S.; Xu, J. Broadband asymmetric transmission of optical waves from spiral plasmonic metamaterials. *Appl. Phys. Lett.* **2014**, *104*. [CrossRef]
169. Pfeiffer, C.; Zhang, C.; Ray, V.; Guo, L.J.; Grbic, A. High Performance Bianisotropic Metasurfaces: Asymmetric Transmission of Light. *Phys. Rev. Lett.* **2014**, *113*. [CrossRef]
170. Sonsilphong, A.; Wongkasem, N. Mid-infrared circular polarization switching in helical metamaterials. *J. Opt.* **2016**, *18*. [CrossRef]
171. Meinzer, N.; Barnes, W.L.; Hooper, I.R. Plasmonic meta-atoms and metasurfaces. *Nat. Photonics* **2014**, *8*, 889–898. [CrossRef]
172. Estakhri, N.M.; Alù, A. Recent progress in gradient metasurfaces. *J. Opt. Soc. Am. B* **2016**, *33*, A21. [CrossRef]
173. Zhu, A.Y.; Kuznetsov, A.I.; Luk'Yanchuk, B.; Engheta, N.; Genevet, P. Traditional and emerging materials for optical metasurfaces. *Nanophotonics* **2017**, *6*, 452–471. [CrossRef]
174. Yu, N.; Capasso, F. Flat optics with designer metasurfaces. *Nat. Mater.* **2014**, *13*, 139–150. [CrossRef] [PubMed]
175. Chen, S.; Liu, W.; Li, Z.; Cheng, H.; Tian, J. Metasurface-Empowered Optical Multiplexing and Multifunction. *Adv. Mater.* **2020**, *32*, 1805912. [CrossRef]
176. Pfeiffer, C.; Grbic, A. Cascaded metasurfaces for complete phase and polarization control. *Appl. Phys. Lett.* **2013**, *102*. [CrossRef]
177. Li, J.; Chen, S.; Yang, H.; Li, J.; Yu, P.; Cheng, H.; Gu, C.; Chen, H.T.; Tian, J. Simultaneous control of light polarization and phase distributions using plasmonic metasurfaces. *Adv. Funct. Mater.* **2015**, *25*, 704–710. [CrossRef]
178. Wang, W.; Guo, C.; Zhao, Z.; Li, J.; Shi, Y. Polarization multiplexing and bifocal optical vortex metalens. *Results Phys.* **2020**, *17*, 103033. [CrossRef]
179. Cheng, H.; Wei, X.; Yu, P.; Li, Z.; Liu, Z.; Li, J.; Chen, S.; Tian, J. Integrating polarization conversion and nearly perfect absorption with multifunctional metasurfaces. *Appl. Phys. Lett.* **2017**, *110*. [CrossRef]

180. Zheludev, N.I.; Plum, E. Reconfigurable nanomechanical photonic metamaterials. *Nat. Nanotechnol.* **2016**, *11*, 16–22. [CrossRef]
181. Ho, C.P.; Pitchappa, P.; Lin, Y.S.; Huang, C.Y.; Kropelnicki, P.; Lee, C. Electrothermally actuated microelectromechanical systems based omega-ring terahertz metamaterial with polarization dependent characteristics. *Appl. Phys. Lett.* **2014**, *104*. [CrossRef]
182. Zhao, X.; Schalch, J.; Zhang, J.; Seren, H.R.; Duan, G.; Averitt, R.D.; Zhang, X. Electromechanically tunable metasurface transmission waveplate at terahertz frequencies. *Optica* **2018**, *5*, 303. [CrossRef]
183. Wu, P.C.; Zhu, W.; Shen, Z.X.; Chong, P.H.J.; Ser, W.; Tsai, D.P.; Liu, A.Q. Broadband Wide-Angle Multifunctional Polarization Converter via Liquid-Metal-Based Metasurface. *Adv. Opt. Mater.* **2017**, *5*, 1–7. [CrossRef]
184. Ma, F.; Qian, Y.; Lin, Y.S.; Liu, H.; Zhang, X.; Liu, Z.; Ming-Lin Tsai, J.; Lee, C. Polarization-sensitive microelectromechanical systems based tunable terahertz metamaterials using three dimensional electric split-ring resonator arrays. *Appl. Phys. Lett.* **2013**, *102*. [CrossRef]
185. Nouman, M.T.; Hwang, J.H.; Faiyaz, M.; Lee, K.-J.; Noh, D.-Y.; Jang, J.-H. Vanadium dioxide based frequency tunable metasurface filters for realizing reconfigurable terahertz optical phase and polarization control. *Opt. Express* **2018**, *26*, 12922. [CrossRef] [PubMed]
186. Sugano, S.; Kojima, N. *Magneto-Optics*; Springer: Berlin/Heidelberg, Germany, 2000; ISBN 9783662041437.
187. Misemer, D.K. The effect of spin-orbit interaction and exchange splitting on magneto-optic coefficients. *J. Magn. Magn. Mater.* **1988**, *72*, 267–274. [CrossRef]
188. Stupakiewicz, A.; Chizhik, A.; Tekielak, M.; Zhukov, A.; Gonzalez, J.; Maziewski, A. Direct imaging of the magnetization reversal in microwires using all-MOKE microscopy. *Rev. Sci. Instrum.* **2014**, *85*, 103702. [CrossRef]
189. McDaniel, T. Magneto-optical data storage. *Commun. ACM* **2000**, *43*, 56–63. [CrossRef]
190. Shoji, Y.; Mizumoto, T.; Yokoi, H.; Hsieh, I.-W.; Osgood, R.M. Magneto-optical isolator with silicon waveguides fabricated by direct bonding. *Appl. Phys. Lett.* **2008**, *92*, 071117. [CrossRef]
191. Tien, P.K.; Martin, R.J.; Wolfe, R.; Le Craw, R.C.; Blank, S.L. Switching and modulation of light in magneto-optic waveguides of garnet films. *Appl. Phys. Lett.* **1972**, *21*, 394–396. [CrossRef]
192. Kim, S.; Hong, Y.-P.; Kim, Y.-G.; Lee, D.-J. Field-calibrated magneto-optic sensor based on off-axis optical probing of intense magnetic fields. *Appl. Opt.* **2017**, *56*, 1701. [CrossRef]
193. Chiu, K.W.; Quinn, J.J. Magnetoplasma Surface Waves in Metals. *Phys. Rev. B* **1972**, *5*, 4707–4709. [CrossRef]
194. Floess, D.; Giessen, H. Nonreciprocal hybrid magnetoplasmonics. *Rep. Prog. Phys.* **2018**, *81*, 116401. [CrossRef] [PubMed]
195. Chen, J.; Albella, P.; Pirzadeh, Z.; Alonso-González, P.; Huth, F.; Bonetti, S.; Bonanni, V.; Åkerman, J.; Nogués, J.; Vavassori, P.; et al. Plasmonic Nickel Nanoantennas. *Small* **2011**, *7*, 2341–2347. [CrossRef] [PubMed]
196. Tomitaka, A.; Arami, H.; Raymond, A.; Yndart, A.; Kaushik, A.; Jayant, R.D.; Takemura, Y.; Cai, Y.; Toborek, M.; Nair, M. Development of magneto-plasmonic nanoparticles for multimodal image-guided therapy to the brain. *Nanoscale* **2017**, *9*, 764–773. [CrossRef]
197. Urries, I.; Muñoz, C.; Gomez, L.; Marquina, C.; Sebastian, V.; Arruebo, M.; Santamaria, J. Magneto-plasmonic nanoparticles as theranostic platforms for magnetic resonance imaging, drug delivery and NIR hyperthermia applications. *Nanoscale* **2014**, *6*, 9230. [CrossRef]
198. Pineider, F.; Sangregorio, C. Nanomaterials for Magnetoplasmonics. In *Novel Magnetic Nanostructures*; Elsevier: Amsterdam, The Netherlands, 2018; pp. 191–220.
199. Li, Y.; Zhang, Q.; Nurmikko, A.V.; Sun, S. Enhanced Magnetooptical Response in Dumbbell-like Ag−CoFe 2 O 4 Nanoparticle Pairs. *Nano Lett.* **2005**, *5*, 1689–1692. [CrossRef]
200. Jain, P.K.; Xiao, Y.; Walsworth, R.; Cohen, A.E. Surface Plasmon Resonance Enhanced Magneto-Optics (SuPREMO): Faraday Rotation Enhancement in Gold-Coated Iron Oxide Nanocrystals. *Nano Lett.* **2009**, *9*, 1644–1650. [CrossRef]
201. Wang, L.; Clavero, C.; Huba, Z.; Carroll, K.J.; Carpenter, E.E.; Gu, D.; Lukaszew, R.A. Plasmonics and Enhanced Magneto-Optics in Core-Shell Co-Ag Nanoparticles. *Nano Lett.* **2011**, *11*, 37. [CrossRef]
202. Chin, J.Y.; Steinle, T.; Wehlus, T.; Dregely, D.; Weiss, T.; Belotelov, V.I.; Stritzker, B.; Giessen, H. Nonreciprocal plasmonics enables giant enhancement of thin-film Faraday rotation. *Nat. Commun.* **2013**, *4*, 1599. [CrossRef]

203. Fujikawa, R.; Baryshev, A.V.; Kim, J.; Uchida, H.; Inoue, M. Contribution of the surface plasmon resonance to optical and magneto-optical properties of a Bi:YIG-Au nanostructure. *J. Appl. Phys.* **2008**, *103*, 07D301. [CrossRef]
204. Floess, D.; Chin, J.Y.; Kawatani, A.; Dregely, D.; Habermeier, H.-U.; Weiss, T.; Giessen, H. Tunable and switchable polarisation rotation with non-reciprocal plasmonic thin films at designated wavelengths. *Light Sci. Appl.* **2015**, *4*, e284. [CrossRef]
205. Kuzmichev, A.N.; Sylgacheva, D.A.; Kozhaev, M.A.; Krichevsky, D.M.; Shaposhnikov, A.N.; Berzhansky, V.N.; Freire-Fernández, F.; Qin, H.J.; Popova, O.E.; Keller, N.; et al. Influence of the Plasmonic Nanodisk Positions Inside a Magnetic Medium on the Faraday Effect Enhancement. *Phys. Status Solidi Rapid Res. Lett.* **2020**, *14*, 1–4. [CrossRef]
206. Crassee, I.; Levallois, J.; Walter, A.L.; Ostler, M.; Bostwick, A.; Rotenberg, E.; Seyller, T.; van der Marel, D.; Kuzmenko, A.B. Giant Faraday rotation in single- and multilayer graphene. *Nat. Phys.* **2011**, *7*, 48–51. [CrossRef]
207. Tymchenko, M.; Nikitin, A.Y.; Martín-Moreno, L. Faraday Rotation Due to Excitation of Magnetoplasmons in Graphene Microribbons. *ACS Nano* **2013**, *7*, 9780–9787. [CrossRef]
208. Kimel, A.V.; Kirilyuk, A.; Usachev, P.A.; Pisarev, R.V.; Balbashov, A.M.; Rasing, T. Ultrafast non-thermal control of magnetization by instantaneous photomagnetic pulses. *Nature* **2005**, *435*, 655–657. [CrossRef]
209. Kruglyak, V.V.; Hicken, R.J.; Ali, M.; Hickey, B.J.; Pym, A.T.G.; Tanner, B.K. Ultrafast third-order optical nonlinearity of noble and transition metal thin films. *J. Opt. A Pure Appl. Opt.* **2005**, *7*. [CrossRef]
210. Hansteen, F.; Kimel, A.; Kirilyuk, A.; Rasing, T. Nonthermal ultrafast optical control of the magnetization in garnet films. *Phys. Rev. B–Condens. Matter Mater. Phys.* **2006**, *73*, 014421. [CrossRef]
211. Cheng, O.H.-C.; Son, D.H.; Sheldon, M. Light-induced magnetism in plasmonic gold nanoparticles. *Nat. Photonics* **2020**, 1–4. [CrossRef]
212. Bonanni, V.; Bonetti, S.; Pakizeh, T.; Pirzadeh, Z.; Chen, J.; Nogués, J.; Vavassori, P.; Hillenbrand, R.; Åkerman, J.; Dmitriev, A. Designer Magnetoplasmonics with Nickel Nanoferromagnets. *Nano Lett.* **2011**, *11*, 5333–5338. [CrossRef]
213. Safarov, V.I.; Kosobukin, V.A.; Hermann, C.; Lampel, G.; Peretti, J.; Marlière, C. Magneto-optical effects enhanced by surface plasmons in metallic multilayer films. *Phys. Rev. Lett.* **1994**, *73*, 3584–3587. [CrossRef]
214. González-Díaz, J.B.; García-Martín, A.; García-Martín, J.M.; Cebollada, A.; Armelles, G.; Sepúlveda, B.; Alaverdyan, Y.; Käll, M. Plasmonic Au/Co/Au Nanosandwiches with Enhanced Magneto-optical Activity. *Small* **2008**, *4*, 202–205. [CrossRef] [PubMed]
215. López-Ortega, A.; Zapata-Herrera, M.; Maccaferri, N.; Pancaldi, M.; Garcia, M.; Chuvilin, A.; Vavassori, P. Enhanced magnetic modulation of light polarisation exploiting hybridization with multipolar dark plasmons in magnetoplasmonic nanocavities. *Light Sci. Appl.* **2020**, *9*. [CrossRef] [PubMed]
216. Kreilkamp, L.E.; Belotelov, V.I.; Chin, J.Y.; Neutzner, S.; Dregely, D.; Wehlus, T.; Akimov, I.A.; Bayer, M.; Stritzker, B.; Giessen, H. Waveguide-Plasmon Polaritons Enhance Transverse Magneto-Optical Kerr Effect. *Phys. Rev. X* **2013**, *3*, 041019. [CrossRef]
217. Manera, M.G.; Colombelli, A.; Taurino, A.; Martin, A.G.; Rella, R. Magneto-Optical properties of noble-metal nanostructures: Functional nanomaterials for bio sensing. *Sci. Rep.* **2018**, *8*, 12640. [CrossRef] [PubMed]
218. Rizal, C.; Kapralov, P.O.; Ignatyeva, D.; Belotelov, V.; Pisana, S. Comparison of the effects of surface plasmon resonance and the transverse magneto-optic Kerr effect in magneto-optic plasmonic nanostructures. *J. Phys. D Appl. Phys.* **2020**, *53*, 02LT02. [CrossRef]
219. Pendry, J.B.; Holden, A.J.; Robbins, D.J.; Stewart, W.J. Magnetism from conductors and enhanced nonlinear phenomena. *IEEE Trans. Microw. Theory Tech.* **1999**, *47*, 2075–2084. [CrossRef]
220. Klein, M.W.; Enkrich, C.; Wegener, M.; Soukoulis, C.M.; Linden, S. Single-slit split-ring resonators at optical frequencies: Limits of size scaling. *Opt. Lett.* **2006**, *31*, 1259–1261. [CrossRef]
221. Bao, Y.; Hu, Z.; Li, Z.; Zhu, X.; Fang, Z. Magnetic Plasmonic Fano Resonance at Optical Frequency. *Small* **2015**, *11*, 2177–2181. [CrossRef]
222. Kuznetsov, A.I.; Miroshnichenko, A.E.; Hsing Fu, Y.; Viswanathan, V.; Rahmani, M.; Valuckas, V.; Ying Pan, Z.; Kivshar, Y.; Pickard, D.S.; Luk'Yanchuk, B. Split-ball resonator as a three-dimensional analogue of planar split-rings. *Nat. Commun.* **2014**, *5*, 1–8. [CrossRef]
223. Wang, P.; Huh, J.; Lee, J.; Kim, K.; Park, K.J.; Lee, S.; Ke, Y. Magnetic Plasmon Networks Programmed by Molecular Self-Assembly. *Adv. Mater.* **2019**, *31*, 1901364. [CrossRef]

224. Monticone, F.; Alù, A. The quest for optical magnetism: From split-ring resonators to plasmonic nanoparticles and nanoclusters. *J. Mater. Chem. C* **2014**, *2*, 9059–9072. [CrossRef]
225. Calandrini, E.; Cerea, A.; De Angelis, F.; Zaccaria, R.P.; Toma, A. Magnetic hot-spot generation at optical frequencies: From plasmonic metamolecules to all-dielectric nanoclusters. *Nanophotonics* **2018**, *8*, 45–62. [CrossRef]
226. Sandrock, M.L.; Pibel, C.D.; Geiger, F.M.; Foss, C.A. Synthesis and second-harmonic generation studies of noncentrosymmetric gold nanostructures. *J. Phys. Chem. B* **1999**, *103*, 2668–2673. [CrossRef]
227. Lippitz, M.; Van Dijk, M.A.; Orrit, M. Third-harmonic generation from single gold nanoparticles. *Nano Lett.* **2005**, *5*, 799–802. [CrossRef]
228. Kruk, S.; Weismann, M.; Bykov, A.Y.; Mamonov, E.A.; Kolmychek, I.A.; Murzina, T.; Panoiu, N.C.; Neshev, D.N.; Kivshar, Y.S. Enhanced Magnetic Second-Harmonic Generation from Resonant Metasurfaces. *ACS Photonics* **2015**, *2*, 1007–1012. [CrossRef]
229. Ding, S.J.; Zhang, H.; Yang, D.J.; Qiu, Y.H.; Nan, F.; Yang, Z.J.; Wang, J.; Wang, Q.Q.; Lin, H.Q. Magnetic Plasmon-Enhanced Second-Harmonic Generation on Colloidal Gold Nanocups. *Nano Lett.* **2019**, *19*, 2005–2011. [CrossRef]
230. Shcherbakov, M.R.; Neshev, D.N.; Hopkins, B.; Shorokhov, A.S.; Staude, I.; Melik-Gaykazyan, E.V.; Decker, M.; Ezhov, A.A.; Miroshnichenko, A.E.; Brener, I.; et al. Enhanced third-harmonic generation in silicon nanoparticles driven by magnetic response. *Nano Lett.* **2014**, *14*, 6488–6492. [CrossRef]
231. Krutyanskiy, V.L.; Kolmychek, I.A.; Gan'shina, E.A.; Murzina, T.V.; Evans, P.; Pollard, R.; Stashkevich, A.A.; Wurtz, G.A.; Zayats, A.V. Plasmonic enhancement of nonlinear magneto-optical response in nickel nanorod metamaterials. *Phys. Rev. B* **2013**, *87*, 035116. [CrossRef]
232. Kolmychek, I.A.; Shaimanov, A.N.; Baryshev, A.V.; Murzina, T. V Magnetization-induced effects in second harmonic generation under the lattice plasmon resonance excitation. *Opt. Lett.* **2016**, *41*, 5446. [CrossRef]
233. Valev, V.K.; Silhanek, A.V.; Gillijns, W.; Jeyaram, Y.; Paddubrouskaya, H.; Volodin, A.; Biris, C.G.; Panoiu, N.C.; De Clercq, B.; Ameloot, M.; et al. Plasmons reveal the direction of magnetization in nickel nanostructures. *ACS Nano* **2011**, *5*, 91–96. [CrossRef]
234. Pineider, F.; Campo, G.; Bonanni, V.; Fernández, C.D.J.; Mattei, G.; Caneschi, A.; Gatteschi, D.; Sangregorio, C. Circular magnetoplasmonic modes in gold nanoparticles. *Nano Lett.* **2013**, *13*, 4785–4789. [CrossRef] [PubMed]
235. Melnikau, D.; Govyadinov, A.A.; Sánchez-Iglesias, A.; Grzelczak, M.; Liz-Marzán, L.M.; Rakovich, Y.P. Strong Magneto-Optical Response of Nonmagnetic Organic Materials Coupled to Plasmonic Nanostructures. *Nano Lett.* **2017**, *17*, 1808–1813. [CrossRef]
236. Shiratsu, T.; Yao, H. Magnetic circular dichroism (MCD) in silver nanocubes with different sizes. *Chem. Phys. Lett.* **2018**, *706*, 607–612. [CrossRef]
237. Yin, P.; Tan, Y.; Fang, H.; Hegde, M.; Radovanovic, P.V. Plasmon-induced carrier polarisation in semiconductor nanocrystals. *Nat. Nanotechnol.* **2018**, *13*, 463–467. [CrossRef] [PubMed]
238. Pineider, F.; de Julián Fernández, C.; Videtta, V.; Carlino, E.; al Hourani, A.; Wilhelm, F.; Rogalev, A.; Cozzoli, P.D.; Ghigna, P.; Sangregorio, C. Spin-Polarisation Transfer in Colloidal Magnetic-Plasmonic Au/Iron Oxide Hetero-nanocrystals. *ACS Nano* **2013**, *7*, 857–866. [CrossRef]
239. Sepúlveda, B.; Calle, A.; Lechuga, L.M.; Armelles, G. Highly sensitive detection of biomolecules with the magneto-optic surface-plasmon-resonance sensor. *Opt. Lett.* **2006**, *31*, 1085. [CrossRef] [PubMed]
240. Rizal, C.; Pisana, S.; Hrvoic, I.; Fullerton, E.E. Microstructure and magneto-optical surface plasmon resonance of Co/Au multilayers. *J. Phys. Commun.* **2018**, *2*, 055010. [CrossRef]
241. Manera, M.G.; Colombelli, A.; Rella, R.; Caricato, A.; Cozzoli, P.D.; Martino, M.; Vasanelli, L. TiO 2 brookite nanostructured thin layer on magneto-optical surface plasmon resonance transductor for gas sensing applications. *J. Appl. Phys.* **2012**, *112*, 053524. [CrossRef]
242. Zubritskaya, I.; Lodewijks, K.; Maccaferri, N.; Mekonnen, A.; Dumas, R.K.; Åkerman, J.; Vavassori, P.; Dmitriev, A. Active Magnetoplasmonic Ruler. *Nano Lett.* **2015**, *15*, 3204–3211. [CrossRef] [PubMed]
243. Wang, X.; Feng, J.; Yu, H.; Jin, Y.; Davidson, A.; Li, Z.; Yin, Y. Anisotropically Shaped Magnetic/Plasmonic Nanocomposites for Information Encryption and Magnetic-Field-Direction Sensing. *Research* **2018**, *2018*, 1–13. [CrossRef]
244. Pancaldi, M.; Leo, N.; Vavassori, P. Selective and fast plasmon-assisted photo-heating of nanomagnets. *Nanoscale* **2019**, *11*, 7656–7666. [CrossRef] [PubMed]

245. Belotelov, V.I.; Kreilkamp, L.E.; Akimov, I.A.; Kalish, A.N.; Bykov, D.A.; Kasture, S.; Yallapragada, V.J.; Gopal, A.V.; Grishin, A.M.; Khartsev, S.I.; et al. Plasmon-mediated magneto-optical transparency. *Nat. Commun.* **2013**, *4*, 1–7. [CrossRef] [PubMed]
246. Zubritskaya, I.; Maccaferri, N.; Inchausti Ezeiza, X.; Vavassori, P.; Dmitriev, A. Magnetic Control of the Chiroptical Plasmonic Surfaces. *Nano Lett.* **2018**, *18*, 302–307. [CrossRef] [PubMed]
247. Song, Y.; Tran, V.T.; Lee, J. Tuning Plasmon Resonance in Magnetoplasmonic Nanochains by Controlling Polarisation and Interparticle Distance for Simple Preparation of Optical Filters. *ACS Appl. Mater. Interfaces* **2017**, *9*, 24433–24439. [CrossRef]